Study of physical phenomena of selective laser melting towards increased productivity

THÈSE N^{O} 6817 (2015)

PRÉSENTÉE LE 18 NOVEMBRE 2015
À LA FACULTÉ DES SCIENCES ET TECHNIQUES DE L'INGÉNIEUR
LABORATOIRE DE GESTION ET PROCÉDÉS DE PRODUCTION
PROGRAMME DOCTORAL EN SYSTÈMES DE PRODUCTION ET ROBOTIQUE

ÉCOLE POLYTECHNIQUE FÉDÉRALE DE LAUSANNE

POUR L'OBTENTION DU GRADE DE DOCTEUR ÈS SCIENCES

PAR

Christoph VAN GESTEL

acceptée sur proposition du jury:

Prof. M.-O. Hongler, président du jury
Prof. R. Glardon, Dr E. Boillat, directeurs de thèse
Prof. L. Froyen, rapporteur
Dr A. Burn, rapporteur
Prof. R. Logé, rapporteur

ÉCOLE POLYTECHNIQUE
FÉDÉRALE DE LAUSANNE

Suisse
2015

Acknowledgements

In these paragraphs I would like to thank all the people I have had the pleasure to meet on this journey called life.

Rémy Glardon, my thesis director, for the rare opportunity of pursuing a doctoral degree and the general management of the thesis.
Eric Boillat, my thesis advisor, for his day to day advice and much appreciated help in the lab. As well as for the many stories on Swiss life.

Tatiana and Jamasp, my supporting colleagues and office mates during the thesis.
Marc Matthey for all the technical assistance and pleasant talks.
Ioanna Paniara for taking on the administrative burden and her superb organizational skills.
My other colleagues in the LGPP lab during the years of the thesis preparation, for the friendliness and shared activities.

The mechanical workshop, foremost Marc Jeanneret and Marc Salle, for their help in the production of the many mechanical parts.
The people of the LMM lab for sharing some of their equipment and some of their drinks.

The jury members: Prof. Roland Logé, Prof. Ludo Froyen, Dr. Andreas Burn and Prof. Max-Olivier Hongler for their diligence in scrutinizing this document.

And finally..
My parents and family for all their support over the many years of my life.
My grandparents for keeping me well stocked on cookies throughout the thesis.
My friends in Belgium or abroad for, well, being friends.
My dearest girlfriend, Suzanne, for the shared moments these past five years.

Abstract

This thesis presents an experimentally focused study of three of the key physical phenomena of the Selective Laser Melting (SLM) process. The SLM process increasingly gains momentum in industrial applications. As awareness of the process and its capabilities for the manufacturing of high performance objects increases, some of the current limitations of the process become more apparent. The SLM process is not a fully mature manufacturing process and there are still significant gains to be made in terms of material understanding, process optimization, final part prediction and quality control.

The experimental study of the physical aspects contributes to the material understanding on a fundamental level but also provides the tools for facilitating future research. A link to practical applications is presented in a case study on evaluating the influence of beam movement patterns and on the identification of process instabilities for quality control. A broad literature survey covers the state of the art on improving the SLM process.

The three physical phenomena which are the subject of this study are: the interaction of laser beam light with the material to be processed, the transport of heat within the material and the behavior of the molten material. These three phenomena take place under conditions which are unlike conventional production processes, in terms of energy intensity, thermal gradients and liquid (metal) dynamics.

The laser-material interaction is characterized by the absorptance. An integrating sphere setup is integrated in an SLM machine to measure the absorptance of the material in the pristine and final state. Also the absorptance evolution is characterized. Results are available for Maraging 300 steel powder, silver powder and AlSi10Mg powder. The influence of surface oxidation and surface roughness is discussed.

The heat transport within the powder bed is characterized by diffusion. The thermal diffusivity and thermal conductivity are measured using the flash method with a laser as the energy source. The implementation uses a special laser beam intensity profile and data processing by correlation with numerical simulations. Thermal diffusivity and conductivity values are included for Maraging 300 steel, silver and titanium. The results confirm the large difference between bulk and powder conductivity and the limited influence of the material type.

The melt pool behavior is studied using an integrated coaxial vision system. This system uses a combination of sensors to monitor the radiation which is emitted by the melt pool and its surroundings. The implementation presents optimized timing and data processing protocols. The relation between the melt pool properties and the process stability is explained. A procedure is also developed for obtaining temperature field profiles of the melt pool.

Key words: selective laser melting, absorptance, thermal conductivity, process monitoring, temperature field, defects, scan patterns

Résumé

Cette thèse consiste en une étude expérimentale de trois des phénomènes physiques clés impliqués en fusion sélective par laser (SLM). Le procédé SLM est de plus en plus employé dans les applications industrielles. Mais, en même temps qu'augmente l'intérêt de ce procédé pour la fabrication d'objets complexes à haute valeur ajoutée, certaines de ses limites deviennent de plus en plus apparentes. A l'heure actuelle, le procédé SLM n'a certainement pas encore atteint sa pleine maturité et des progrès importants sont encore à réaliser en termes de compréhension des matériaux, d'optimisation des paramètres opérationnels et de contrôle de la qualité des pièces.

Les études expérimentales présentées dans ce travail doivent contribuer à une meilleure compréhension du comportement du matériau traité et fournir des outils à même de favoriser de nombreuses recherches futures. D'un point de vue plus appliqué, on présente aussi une étude de cas sur l'influence des stratégies de balayage laser. On discute aussi la possibilité d'identifier les instabilités du procédé pour proposer un contrôle direct de qualité. Une large revue de littérature donne, en outre, une vision précise des recherches effectuées à ce jour pour améliorer le procédé SLM.

L'interaction du faisceau laser avec la matière, le transport de chaleur dans le matériau et le comportement du bain liquide sont les trois phénomènes physiques principaux concernés par cette étude. On fait observer qu'ils impliquent des conditions très différentes de celles observées dans les procédés de production traditionnels, que ce soit en terme de gradients thermiques, de concentration d'énergie où de dynamique d'écoulement de fluides.

L'interaction laser-matière est essentiellement caractérisée par l'absorbtivité du matériau. A cette fin, on propose un montage de sphère intégratrice adaptée aux machines SLM. Il est capable de mesurer, in situ, l'absorbtivité des matériaux en fonction de leur évolution entre l'état de poudre libre à celui de solide consolidé. Les résultats sont disponibles pour des matériaux comme l'acier maraging 300, l'argent ou un alliage d'aluminium AlSi10Mg. L'influence de l'oxydation et de la rugosité de surface est aussi discutée.

La diffusivité et la conductivité thermique conditionnent le transport de chaleur dans le lit de poudre. On propose de mesurer ces quantités grâce à une méthode flash qui utilise le laser équipant la machine SLM comme source d'énergie. La mise en oeuvre de cette méthode fait intervenir un traitement des données particulier. On utilise, en outre, une corrélation avec des simulations numériques. On illustre cette technique en l'appliquant aux mêmes matériaux (acier maraging 300, argent et alliage d'aluminium AlSi10Mg). Les résultats obtenus confirment la grande différence qui existe entre la conductivité de la poudre et celle du matériau massif.

Le comportement du bain de fusion est enfin étudié à l'aide d'un système intégré de vision coaxial. Ce système utilise une combinaison de capteurs pour analyser le rayonnement infrarouge émis par la poudre en fusion et ses environs. On propose des protocoles d'échantillonage et de traitement de données optimisés pour des conditions de puissances laser et de vitesses de balayage très élevées telles qu'elles sont couramment utilisées, aujourd'hui, en SLM. La relation entre l'évolution du bain de poudre et la stabilité du processus est clairement illustrée. Pour finir, on met au point une procédure de calibration permettant d'utiliser le système de vision coaxial comme un pyromètre bidimensionnel permettant de filmer l'évolution des profils de température en surface.

Mots clefs : fusion sélective par laser, absorptivité, conductivité thermique, contrôle du bain liquide, champ thermique, défauts, stratégies de balayage

Contents

Acknowledgements **i**

Abstract (English/Français) **iii**

List of figures **xi**

List of tables **xv**

Introduction **1**

1 SLM productivity - State of the art **5**
- 1.1 Introduction 5
- 1.2 Raw productivity 6
  - 1.2.1 High power lasers 6
  - 1.2.2 Multiple lasers 6
  - 1.2.3 Alternative energy sources 7
  - 1.2.4 Energy optimization 7
  - 1.2.5 Structural optimization 8
  - 1.2.6 System identification 9
  - 1.2.7 Process understanding 9
- 1.3 Effective productivity 11
  - 1.3.1 Pre-production 11
  - 1.3.2 Defect reduction 12
  - 1.3.3 Defect detection 15
  - 1.3.4 Defect repair 18
  - 1.3.5 Post-processing 18
- 1.4 Versatility 18
  - 1.4.1 Physical properties 19
  - 1.4.2 Novel materials 20
  - 1.4.3 Novel applications 20
- 1.5 Conclusion 20

2 General materials and methods **23**
- 2.1 Introduction 23
- 2.2 Selective Laser Melting machine 23

2.3 Reference materials 24
2.4 Additional methods 26
  2.4.1 Microscopy 26
  2.4.2 Powder apparent density 26

3 Radiation-material interaction 27

3.1 Introduction 27
  3.1.1 Aim 27
  3.1.2 Methodology 27
  3.1.3 State of the art 28
  3.1.4 Novelty 28
3.2 Design and implementation 28
  3.2.1 Method selection 28
  3.2.2 Implementation 29
  3.2.3 Integration 29
3.3 Materials 31
  3.3.1 Calibration materials 31
  3.3.2 Sample materials 31
3.4 Methods 31
  3.4.1 Calibration and validation 31
  3.4.2 Measurement procedure 32
  3.4.3 Data-acquisition 32
  3.4.4 Data analysis 33
  3.4.5 Absorptance calculation 33
3.5 Results and discussion 34
  3.5.1 Calibration and validation 34
  3.5.2 Absorptance 35
  3.5.3 Absorptance evolution 36
3.6 Additional considerations 38
3.7 Conclusion 39

4 Heat diffusion in powder beds 41

4.1 Introduction 41
  4.1.1 Aim 41
  4.1.2 Methodology 41
  4.1.3 State of the art 42
  4.1.4 Novelty 43
4.2 Design and implementation 43
  4.2.1 Method selection 43
  4.2.2 Implementation 43
4.3 Materials and methods 44
  4.3.1 Sample preparation 44
  4.3.2 Calibration 45

4.3.3 Measurement procedure 46
4.3.4 Simulation procedure 46
4.3.5 Diffusivity and conductivity calculation 47
4.4 Results and discussion 47
4.4.1 Measurements 47
4.4.2 Simulations 48
4.4.3 Diffusivity and conductivity 49
4.5 Conclusion 50

5 Melt pool behavior **51**
5.1 Introduction 51
5.1.1 Aim 51
5.1.2 Methodology 51
5.1.3 State of the art 52
5.1.4 Novelty 52
5.2 Background 52
5.2.1 Process monitoring 52
5.2.2 Coaxial vision systems 53
5.2.3 Sensors 53
5.2.4 Data mapping 53
5.3 Design and implementation 53
5.3.1 General assembly 53
5.3.2 Wavelength band selection 55
5.3.3 Spatially integrating sensors 55
5.3.4 Spatially resolving sensors 56
5.4 General acquisition procedure 56
5.4.1 Camera calibration procedure 56
5.4.2 Camera measurement procedure 58
5.4.3 Photodiode measurement procedure 61
5.5 General temperature field procedure 61
5.5.1 Image acquisition 62
5.5.2 Spatial correlation 62
5.5.3 Intensity linearization 64
5.5.4 Radiation spectra 65
5.5.5 Ratio method 66
5.6 Temperature calibration A - Calibrated light source 68
5.6.1 Setup description 68
5.6.2 Ratio calculation 68
5.6.3 Temperature field 68
5.7 Temperature calibration B - Melt pool size 69
5.7.1 Setup description 69
5.7.2 Data-acquisition 70

5.7.3 Melt pool measurement . . . 71
5.8 Additional considerations . . . 72
5.9 Conclusion . . . 72

6 Applications of melt pool characterization 75
6.1 Introduction . . . 75
6.2 Defect development . . . 75
6.2.1 Case description . . . 75
6.2.2 Results and discussion . . . 77
6.3 Melt pool stability maps . . . 77
6.3.1 Case description . . . 77
6.3.2 Results and discussion . . . 78
6.4 Scan pattern comparison . . . 80
6.4.1 Case description . . . 80
6.4.2 Results and discussion . . . 80
6.5 Conclusion . . . 84

Conclusion 85

Bibliography 87

Curriculum Vitae 99

List of Figures

1.1 Overview of the process steps for Selective Laser Melting, with the main tasks for each step on the right. 5

1.2 Absorptance as a function of wavelength for various metals [27]. Typical laser types are highlighted. 8

1.3 Proces map for single tracks with various types of anomalies [86]. 13

1.4 Sample cubes produced without (top) and with (bottom) real-time process control. The scan speeds were 300, 500 and 700 mm/s from left to right, all other parameters were constant [117]. 15

1.5 Melt pool data mapping - detection of overheating at overhangs for varying support structures [125]. 17

1.6 The use of process monitoring for process characterization. Pyrometer output for the scanning of two simple squares, one using a simple one-zone parallel scanning strategy (left) and one using a two-zone scanning strategy (right) [112]. 17

2.1 Photograph of the experimental SLM machine setup. 24

2.2 Micrographs showing the reference powder morphology. 26

3.1 Schematic of the laser beam path for integrating sphere measurements. 30

3.2 Picture of the integrating sphere setup in high flux mode, inside the SLM process chamber. 30

3.3 Demonstration of the sample placement for the measurement of the specular reflection component. 30

3.4 Demonstration of a series of calibration and validation measurements using Aluminum 7075 and a high flux density beam (in-focus). 34

3.5 Average absorptance measurements for several materials and material states. . 35

3.6 Evolution of the instantaneous absorptance during the transition from powder to liquid metal for Maraging steel. Compilation of 8 measurements (grey) and a least-squares exponential fit (black, $-0.044\ln(x)+0.84$). 36

3.7 Evolution of the instantaneous absorptance during the transition from powder to liquid metal for commerically pure silver. Compilation of 8 measurements (grey) and a least-squares exponential fit (black, $-0.09\ln(x)+0.54$). 37

3.8 The melting of Maraging steel powder with a static beam. State after 500 μs and 2000 μs of exposure at 30 W beam power, in high flux density mode. 37

3.9 The melting of commercially pure silver powder with a static beam. State after 500 µs and 2000 µs of exposure at 30 W beam power, in high flux density mode. 38

4.1 Drawing of the powder vessel with tunable thermocouple depth, used for the thermal conductivity experiments. 44
4.2 Intensity distribution of mono-mode laser beams [152]. The laser has a TEM01* type of beam, which results in a ring-like intensity distribution for randomly polarised beams. 45
4.3 Left: Surface of the powder vessel, filled with Maraging steel powder and the mark of the laser beam. Right: Sintered powder cake after repeated exposures. 45
4.4 Representation of the simulation area. The software simulates the heat diffusion in a 2D cutout using the axio-symmetric property. 46
4.5 Examples of temperature-time curves for Maraging steel powder, a pulse time of 20 ms and various sensor depths. The grey curves are the raw measurement data, the black curves are fitted models. 48
4.6 Examples of simulated temperature-time curves for Maraging steel powder. . . 48
4.7 Diffusivity calculation table for the conversion from time to maximum registered temperature to diffusivity. Each curve represents a specific temperature sensor depth. 49
4.8 Diffusivity results for the three tested powder types. The first group gives the average over all measurements. The second group gives a breakdown in terms of sensor depth and the third group in terms of beam exposure time. The error bars represent the standard deviation. 49

5.1 Schema of the components of the general monitoring setup for two sensors. The filters and focusing optics are optional. The sensors can be CMOS cameras, photodiodes or a mixture. 54
5.2 Relevant radiation wavelength bands, with the position of the vision sensor ranges and the laser beam wavelength. 55
5.3 Example calibration image for the MV1-D1312-240-CL8 camera with 300 mm objective. Demonstration of a typical 96x96 pixel region of interest. 56
5.4 Simplified optical chain for the calculation of the effective resolution. 57
5.5 Intensity compression capabilities of the PhotonFocus MV1 CMOS camera system. 58
5.6 Schematic representation of the image timing options for short (top curve) and long (bottom curve) scan vectors for optimal data collection. 59
5.7 Visualization of the concepts of Feret diameter, equivalent ellipse and the ellipse minor axis for the calculation of the aspect ratio of a melt pool. 61
5.8 Example of 2 images for calibration procedure A and comparison between two spatial correlation techniques: cross-correlation through the frequency domain (c) and melt-pool center of gravity (d). The comparison image is the result of the subtraction of the two images after correlation. 63
5.9 Resulting camera sensor return value (gray value) as a function of intensity for two camera exposure modes: no compression and low compression. 64

5.10 Emission spectrum for a black body at various temperatures. The two sensor wavelength bands are indicated. 65
5.11 Normalized intensity ratio for wavelength bands of 810-1000 nm (A) and 700-810 nm (B). Illustration of the method to identify T when the intensity ratio R and the calibration constant C are known. 67
5.12 Temperature field of a calibration image at 3000 K. This type of image is used to check the calibration homogeneity for a given temperature/intensity ratio combination. 69
5.13 Calibration constant as a function of temperature for a typical calibration. The error bars represent the standard deviation over 6 images. The average value of the calibration constant is 2.10. 69
5.14 Temperature field of a melt pool. Calibration according to the calibrated lamp method. The resolution is 25 µm per pixel. 70
5.15 Measurement of the real melt pool width. 71
5.16 Correlation of the real melt pool width to the image intensity line profile. 71

6.1 Illustration of the development and escalation of a defect while scanning thin walls (one image in two, interval ±1.5 – 2 ms, total time 9-12 ms). 76
6.2 Benchmark consisting of 10 different scan patterns. 78
6.3 Mapping of the melt pool size (in mm^2) on a benchmark of 10 scan patterns as detailed in Figure 6.2. 79
6.4 Mapping of the number of the average image intensity on a benchmark of 10 scan patterns as detailed in Figure 6.2. 79
6.5 Mapping of image peak intensity on a benchmark of 10 scan patterns as detailed in Figure 6.2. 80
6.6 Photodiode output for a parallel alternating pattern (Figure 6.2a). 81
6.7 Photodiode output for a parallel uni-directional pattern (Figure 6.2b). 81
6.8 Photodiode output for a zig-zag pattern (Figure 6.2c). 82
6.9 Photodiode output for a non-sequential pattern with two passages (Figure 6.2e). 82
6.10 Photodiode output for a non-sequential pattern with a repetition unit of 2 vector spacings (Figure 6.2f). 83
6.11 Photodiode output for an inwards spiraling pattern (Figure 6.2g). 83
6.12 Photodiode output for an outwards spiraling pattern (Figure 6.2h). 84

List of Tables

1.1 List of process parameters applicable to Selective Laser Melting. 12
1.2 SLM process productivity aspects and the related benefits and drawbacks. . . . 21

2.1 Chemical and physical properties of the reference powders. 25
2.2 Thermal and mechanical properties for the reference materials in bulk form. . 25

3.1 Absorptance values for the calibration materials. 31
3.2 Overview of the various calibration conditions. 32

4.1 Thermal and physical properties of the studied powders, and their measured diffusivities and conductivities. Material data is from Table 2.1 and Table 2.2. The given uncertainty interval for the diffusivity and conductivity is ±1 standard deviation. 50

5.1 Suitable materials for melt pool calibrations. Sourced from MatWeb. 70

Introduction

Project structure

This work is a collection of efforts to increase the general productivity and industrial acceptance of the Selective Laser Melting (SLM) process. The introduction will explain some of the base terminology of the topic, provide a reference frame for the work and summarize the structure of this document.

The state of the art is a compilation of the published works related to the productivity of SLM. A broad range of topics is covered in three categories, based on how these topics influence the process productivity. The first category combines aspects related to the raw productivity. The raw productivity is anything which improves the pre-process optimizations and the raw build rate of parts. This includes fundamental material research and technological developments. The second category is the effective productivity. This category bundles efforts to decrease the amount of post-process work and to decrease the failure rate of parts by studying, monitoring and repairing defects. The third and last category is the versatility of the process. This category tries to list some of the prime aspects of the SLM process and demonstrates how these can be applied to the development of new materials and applications.

The core part focuses on helping the SLM process by improving the knowledge on the SLM sub-processes. Three key physical phenomena are studied in three separate chapters: the interaction of the laser radiation with the build material, the diffusion of heat within the material and the behavior of the material in its molten state. For each phenomenon a dedicated measurement setup is designed and integrated in the in-house SLM machine. Both quantitative and qualitative results are provided. The last chapter contains three short case studies on applications related to the behavior of the molten material.

A general conclusion will summarize the most important results from each topic and discuss the general impact on the future of the Selective Laser Melting process.

Selective Laser Melting

For those unfamiliar with the term, Selective Laser Melting (SLM) is an additive manufacturing process [1]. An additive manufacturing process builds up a 3D object from a smaller scale base material. In the case of SLM, the base material is a powder or granulated material. The base material is delivered in a series of thin layers. Each layer is selectively irradiated by a laser beam, which completely melts the material in the selected regions. A new layer is applied on top of the previous one and the process repeats until the 3D object is fully constructed. A computerized 3D model determines for each layer which regions are to be processed. Additional algorithms calculate the path the laser beam needs to follow to melt the base material in these regions. Some creative implementations of the SLM process do not necessarily adhere to all points of this description, but it holds in general.

Several advancements have been made in the SLM process. Recent successes attest to a growing maturity and acceptance. Large industrial manufacturers like Boeing, Siemens and General Electric are increasingly using SLM for aeronautical and aerospace applications. They cite cost reductions, lead time reductions and a reduction in the number of required parts as the main reasons to shift to additive manufacturing and SLM [2–4]. This is an important step up from the production of prototype parts and tooling equipment, the original applications of the SLM process, and the medical implants and specialized, small functional parts that were later added to the process portfolio. SLM also benefits from the succes of other additive manufacturing processes as fused deposition modeling. The wider commercialization has led to the incorporation of additive manufacturing tools in model design software packages as AutoDesk Inventor [5] and Adobe Photoshop CC [6]. This helps in public awareness and familiarity with the process capabilities.

Problem statement

Despite SLM technology being a fast expanding business, there are signs that some aspects of the technological development of the process are lagging behind. Additive manufacturing is known for producing complex components at low extra cost compared to more simple components [7]. For higher SLM production speeds, this is no longer the case. Increased process instability makes extensive calibration and optimization necessary, increasing cost and lead time [8]. Even though many materials are theoretically suitable to be processed by SLM, again extensive individual optimization is often required. It is also difficult to predict the resulting micro-structure and mechanical properties, preventing directed research strategies and requiring adjustments and iterations to reach the desired properties.

These are manifestations of a lack of fundamental process and material understanding, especially within the physical environment of SLM. The process behaves often unstable and the mechanisms, while well researched, are not yet mastered [9–11]. Qualification and certification, despite significant progress over the last few years for a select number of materials, is still difficult. Advancements in process monitoring, control and repair strategies are progressing and could aid in qualification and ultimately increase process confidence. This is supported by industry, which indicates the need for improvements in material development, process control and inspection tools [12].

Goal and methodology

The ultimate goal is to make the SLM process a viable and preferred choice for as many industrial applications as possible. Reductions in total process time, increased process mastery and improved mechanical characteristics are the paths. The knowledge gained during this work, the techniques that were developed or refined and the new applications that are proposed all help to pave the road.

The work does not present any concrete, quantifiable improvements of productivity. It does aim to present tools and knowledge to facilitate productivity improvements, both in future research and in production environments. The methods presented in this work are developed with maximum machine compatibility in mind and the information is delivered in a format which should be useful both for theoretical engineers developing models as for process engineers looking for practical information.

This thesis is part of a parallel effort in Selective Laser Melting at the Laboratory for Production Management and Processes of the EPFL. It provides experimental data as input and validation for theoretical models developed by Tatiana Polivnikova as part of her thesis [13].

1 SLM productivity - State of the art

1.1 Introduction

While the SLM process is considered fast in the way it doesn't require custom tooling, a typical small part with dimensions of a few centimeters takes hours to days to build, depending on the desired accuracy and properties [14, 15]. This is because, in the SLM process, at any given time, only a very small volume of material is in the molten state. Often this is in the range of 10^{-4} to 10^{-3} mm^3. The laser beam which provokes the melting moves typically at a few hundred to a few thousand millimeters per second. This leads to typical raw melting rates of a few cubic millimeters per second [16, 17]. Added to this are the powder layering times, machine setup time, pre-process 3D model optimizations and process data generation, post-process cool-downs, part extraction and any further post-processing steps. An overview of the process

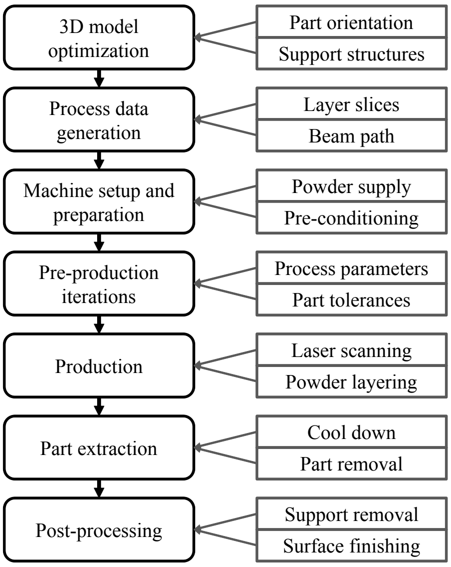
3D model optimization
Part orientation
Support structures
Process data generation
Layer slices
Beam path
Machine setup and preparation
Powder supply
Pre-conditioning
Pre-production iterations
Process parameters
Part tolerances
Production
Laser scanning
Powder layering
Part extraction
Cool down
Part removal
Post-processing
Support removal
Surface finishing

Figure 1.1 – Overview of the process steps for Selective Laser Melting, with the main tasks for each step on the right.

steps and the main tasks for each step is presented in Figure 1.1.

This chapter gives a broad overview of the topics which affect the productivity of the SLM process. The topics are divided in three categories: the raw productivity, the effective productivity and the versatility of the process.

1.2 Raw productivity

This section contains aspects which influence the raw productivity of the SLM process; the consolidation by laser and the powder layering. For large parts, the raw processing can take 80% of the total processing time [16, 17].

1.2.1 High power lasers

While more of a natural technological evolution, the availability of increasingly powerful laser sources enables an increase in the melt rate. Even though multi-kilowatt (CO_2) laser sources were available [18–20], the resulting laser beams did not have favorable cost/quality ratios and a low efficiency [11]. Newer generations of laser technology (Yb:YAG, Yb-fiber, diode disk) combine high quality laser beams with higher output powers.

Due to an increase in process instabilities at higher energy throughputs (evaporation, spattering), the increase in melt rate is usually not linear with the beam power. The same effects make process optimization increasingly time-consuming. For AlSi10Mg, a 4 fold increase in melt rate was achieved with a 6 fold increase of beam power [16]. Sometimes the increase in energy density, provided by high quality, high power beams allows or facilitates the processing of materials. An example is aluminum, which has a high reflectivity and high thermal conductivity, two properties which lower the efficiency of the process [16].

1.2.2 Multiple lasers

A rather straightforward approach in concept, is the integration of multiple lasers in the same processing unit. This decreases the melting time, while all other process steps remain unchanged. The multiple lasers can work in series or simultaneously, depending on whether they share some of the hardware.

When only one laser can be active at any time (serial), the lasers are usually distinct in functionality. For example one laser is used for high precision at small features or edges, while a higher power laser melts areas with a lower required precision (due to a larger or more instable melt pool) [17].

Simultaneously operating laser beams are possible in different configurations. Similar, independent lasers can be used to double, triple, or further multiply the melt rate by melting different regions independently. Dissimilar lasers can be used in the same way as explained before, with each laser having its own functionality, but operating simultaneously. A third configuration is the use of dissimilar lasers with movement constraints. A second laser can be positioned in front, superimposed, next to or behind another laser. This technique changes the energy distribution of the combined lasers and can lead to increases in productivity, process stability [21] or part quality.

1.2.3 Alternative energy sources

A number of alternative ways of delivering a portion of the required energy for melting have been reported. These energy sources are often less spatially and temporally concentrated as the laser beam but can increase the melting rate by decreasing the required laser energy.

One approach is to use an external energy source. The energy can be delivered by a radiative source to the surface of the construction bed. The radiative source can be a lamp or another laser. Conductive heating is possible, and in the case of electrically conductive materials also inductive heating. These generally heat the whole build volume, usually from the bottom up. Although the difference in thermal (and electrical) conductivity between the unexposed powder and the solidified material can preferentially heat the constructed part. Practically, the required energy can only be reduced by $10-25\%$ when micro-structural changes should be avoided.

A quite different approach is to use the energy of an exothermal chemical reaction [22]. The reagents are pre-mixed with the base powder or present in the processing units atmosphere. The reaction is usually thermally activated by the scanning laser beam and can release the additional energy in a very localized way, in space and in time. An example is the reaction of iron oxide (Fe_2O_3) in aluminum powder [22].

1.2.4 Energy optimization

Optimizing the energy needed to melt a unit of volume of material leads to similar improvements as using higher power lasers or external energy sources, but is more economical [23]. Usually the idea is to reduce the energy density as much as possible while still achieving the required physical [23] and mechanical properties. The energy optimization is often performed by establishing a process map for a large range of process parameters [24, 25] and by optimizing the energy density parameter.

Energy optimization can also be carried out by optimizing the energy uptake. The energy uptake efficiency of the powder bed can play an important role, as the material absorption strongly depends on laser wavelength [26, 27] (Figure 1.2). Modifying the beam shape and the powder layer thickness can change the influx of energy [28]. The powder morphology also has an effect. For instance, in a bimodal size distribution, a lower fraction of large particles will result in a higher energy flux in the powder bed [29].

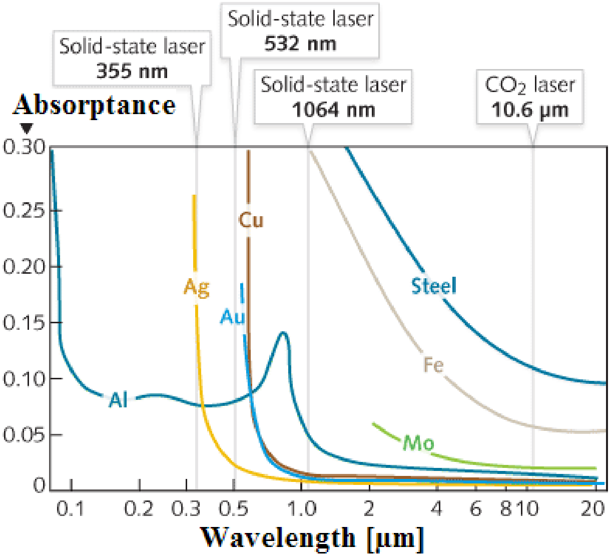

Figure 1.2 – Absorptance as a function of wavelength for various metals [27]. Typical laser types are highlighted.

Locally adapting the part quality can save on energy for the mechanically less important regions of a part [30]. For example a higher quality but less productive input strategy can be utilized at the exposed surfaces of a part or at sharp features. While a reduced energy input - through higher melt rates at constant beam power - is used for the internal part regions. This is sometimes called a skin-core approach [17].

1.2.5 Structural optimization

Another way to improve the part build time is to reduce the volume to melt. This uses one of the key advantages of additive manufacturing, which offers additional part complexity for free. There are two main ways to reduce the part volume in exchange for an increase in complexity: topological optimization of the general part shape and lattice structures. Weight reductions up to 50% can be achieved, by example for automotive parts [16].

Topological optimization heavily relies on mechanical models and simulations. The shape and volume of each feature of a part is optimized towards a number of geometrical and mechanical constraints. One of the possible optimizations is to reduce the mass as much as possible while maintaining the minimum mechanical properties. Several software solutions are already available [31]. A less generic form of topological optimization is layout optimization, which optimizes the size and orientation of discrete elements to yield solutions which are generally more practical to implement [32].

Lattice structures are a structured way of introducing internal porosity in a part. Different types of unit cell geometries, formed by consolidated struts, have been researched and assessed in terms of production quality and resulting morphological and mechanical properties [33–

35]. Different types of geometry and orientation are optimal depending on the eventual mechanical load [36]. The struts should be preferentially loaded along their longitudinal axis [33]. The layered processing does affect the lattice quality for some orientations, especially horizontal struts and bridges tend to be lower in quality [34]. Ultimately, optimizing the type, orientation and density of the internal lattice structure of parts can significantly decrease the volume to melt, while maintaining the part functionality [33]. Some design rules for optimal incorporation of lattice structures have been derived [35]. The lattice structure can also be exposed to the surface of the part. This is especially useful for some medical applications, for example to facilitate bone ingrowth in implants [33].

1.2.6 System identification

The laser beam is in most cases positioned by a system of galvanic mirrors. For higher displacement speeds ($>1\,\mathrm{m\,s^{-1}}$), signal lag and inertial lag drive the need for proper timing or synchronization. For lattice structures or very porous parts, the beam displacement time during which the laser is 'off' due to acceleration/deceleration phases can be substantial. Identification of the beam displacement and laser 'on/off' systems can help in optimizing the beam displacements to reduce the laser 'off' time. Reductions of 10% [37, 38] in raw consolidation time have been obtained.

1.2.7 Process understanding

The SLM process takes some basic physical mechanisms to extreme grounds, introducing effects that are not observed or are of lesser importance for classical production processes. These include effects caused by the high energy density of the laser beam and the difference in properties of the powder versus the solidified material.

Radiation absorption

The first interaction of the laser beam with the material is the absorption of part of the incoming radiation. Typically radiation is either absorbed by the material or reflected back (specularly or diffusely). For most solid materials transmission of radiation is limited. However, for the SLM process, the powder bed acts as a diffuse and partially transparent medium. It has been demonstrated both theoretically [26, 28, 29, 39, 40] and experimentally [26, 41] that there can be significant penetration of the radiation in the powder bed. The general mechanism is through multiple reflections on the curved powder particle surfaces and through the pores of the powder bed.

The volumetric absorption mechanism of the powder bed results in very different amounts of energy absorbed by the material. The increased absorption of unconsolidated material is one of the reasons for 'burn in' or overheating at the start of a new scan vector [42]. A stable interface below the laser beam is in general important for process stability. Even variations in rugosity of the surface (solid or molten) can significantly affect the absorption [43].

The absorptance ratio of a material is also temperature dependent [44, 45]. The large temperature interval of the SLM process can require to take this dependence into account. Metals generally show an increase in absorption for increasing temperature and also phase transformations can affect the absorptance. However, around the wavelength range of 1 µm, many metals have a relatively low temperature dependence of the absorptance [46].

The high energy density of the modern SLM process can introduce secondary effects at the surface, as oxidation [45], vaporization [28], plasma formation [47, 48] and the creation of shock waves through rapid heating of air and material vaporization [45]. These are generally unwanted effects as they result in material loss, inefficient use of energy and obstruction of the laser beam. Sometimes the presence of oxides at the surface can increase the absorption efficiency, without adversely affecting the melt pool [49].

Heat transfer

The transport of thermal energy is the key physical aspect of the SLM process. Ideally the temperature is homogeneous and just above the liquidus in the volume being melted. The melt pool should extend just into the previously consolidated layer to achieve good bonding, while it should not expand too much outwards near the top surface.

The heat transfer within the powder bed has been researched extensively [50–56]. The transfer mechanism inside the powder bed is characterized by thermal conductivity [44]. Generally the thermal conductivity of the powder bed is very low compared to the fully dense state of the same material. For metals the difference can span several orders of magnitude [57]. The main reason is the thermal resistance of the contact points between the powder particles. The powder morphology has been found to have an influence: smaller and irregularly shaped particles have higher contact resistance and lower thermal conductivity. The thermal conductivity can be as much as three times lower for 10 µm particles as for 100 µm particles [52, 58]. Mechanical compression or thermal sintering improves the particle contacts and can increase the thermal conductivity (approximately 10% for a 7% increase of density at 40% powder bed relative density for 316L steel) [52, 58].

In between the loose powder state and the consolidated state the thermal conductivity changes depending on the resulting pore morphology. This transition has been studied both theoretically [44, 56, 57, 59] and experimentally [52, 57, 60].

The large difference in thermal conductivity of the powder bed versus the consolidated material has several implications. A scan next to consolidated material will leak energy from the melt pool to the consolidated material [61, 62]. The downwards expansion of the melt pool is slower because it has to penetrate powder. Thinner powder layers (20 to 50 µm) can use the radiation penetration effect to reduce the necessary heat transfer [28]. Once the melt pool reaches the previously consolidated layer, the heat loss to the consolidated layer can decrease the temperature of the melt pool and prevent the melt pool from creating a continuous interface with the previous layer. The absence of some of these sources of energy loss at part edges or at overhanging geometry can drastically change the temperature field and negatively affect process quality [63].

Simulation

While a better comprehension of the previously mentioned physical phenomena can aid directly in process optimization, the principal use is the application in models and (computer) simulations of the process [64].

Various models have been adapted or developed for the SLM process, ranging from analytical descriptions [65] over mixed analytical/finite element models [62, 66] to comprehensive multiphysics finite element models [67–71]. Some models simulate the powder volumes and melt pool hydrodynamics [53, 70] which can predict porosity, surface shape, and sintering in heat affected zones. The models are used to estimate starting values for the process parameter optimization [72], analyze the process stability [73–75] or to predict the mechanical performance [68, 71, 76]. These techniques can lead to significant time savings in the initial optimization for a new material or a particularly complex part. Accurate models are also a requirement for other aspects, such as topological optimization.

1.3 Effective productivity

This section discusses the topics related to the effective productivity; the pre-processing, the failure rate and the post-processing.

1.3.1 Pre-production

For unique parts or small series, the pre-production can be more time-consuming than the actual production. The general pre-production is the preparation of the process code from the 3D model data and the process parameter iterations until the part meets the specifications. Once a parameter set has been established for a certain material or a certain geometry, the pre-production time is greatly reduced and limited to the software part pre-processing.

Part pre-processing

For the SLM process the orientation of the parts relative to the build orientation (z-axis) is an important parameter which impacts the mechanical properties and other aspects as the surface quality [1, 34, 77–80]. The height of the part also determines the number of required powder layering steps. More layers increase the production time.

Even though the powder bed can support overhanging features, additional supporting struc-

Table 1.1 – List of process parameters applicable to Selective Laser Melting.

- Beam wavelength
- Beam size
- Beam shape
- Beam intensity distribution
- Beam power
- Beam scan speed
- Powder class
- Powder shape
- Powder size (distribution)
- Powder bed density
- Layer thickness
- Processing temperature
- Process atmosphere
- Process pressure
- Scan pattern type
- Scan spacing
- Various pattern modifications

tures are sometimes required to aid in the thermal balance or prevent warping of the part [76, 81]. Software solutions become increasingly capable of highlighting regions that may require additional support and adding these supports to the 3D model [82].

In order to avoid geometrical inconsistencies, it is important to limit rounding or approximation errors during the conversion of the 3D model to the beam path. Improved geometrical algorithms [83, 84] and compensation strategies have been proposed [79].

Parameter optimization strategies

The actual production process itself encompasses many more process parameters, the optimal values of which are sensitive to changes in the equipment (laser, atmosphere) and material properties (powder morphology and physical properties). These are represented in Table 1.1. The current level of understanding of the interactions between these parameters requires experimental optimization of at least some of them [77]. Often process maps are experimentally defined for new materials and specific sets of equipment [20, 24, 25, 85] (Figure 1.3).

Experimental design strategies have been proposed to decrease the experimental workload, ranging from factorial designs to genetic algorithms [87–93]. Computer simulations can also provide a starting point or help define process limits.

1.3.2 Defect reduction

Various types of defects can occur during the production and cause the part to fail quality control. The main types of defects are: geometrical inaccuracies [30, 94–96], warping [75, 76, 97–101], delamination [20, 98], internal and edge porosity [102–104], balling and spattering [20, 42, 85, 86, 97, 105, 106]. The reduction of the prevalence of these defects can be achieved by optimizing the process parameters. Other means to reduce defects exist but often negatively affect the raw productivity, so a trade-off has to be made between fewer failed parts and shorter production run times.

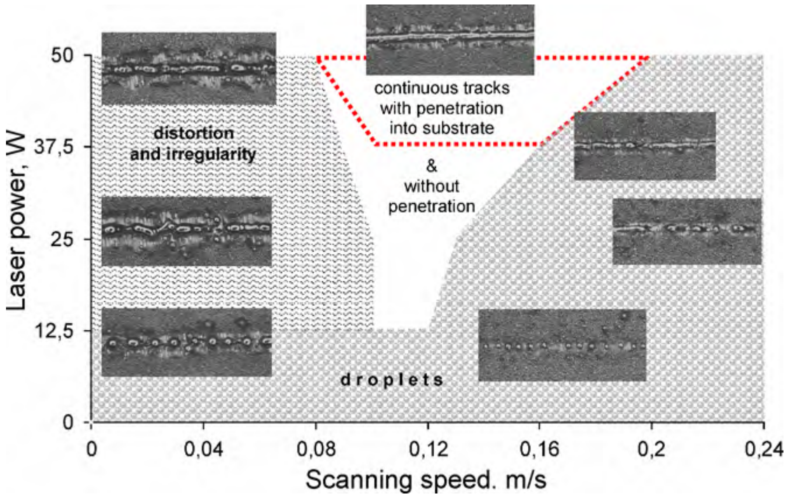

Figure 1.3 – Proces map for single tracks with various types of anomalies [86].

Scan pattern

The scan pattern is the geometrical pattern the laser beam follows to melt a cross-section of the part. The basis is usually a series of parallel lines (also tracks or vectors). Many additions and small variations have been studied. Usually they try to address a specific type of defect.

One variation is to scan the contour of the cross-section as a separate step, before and/or after the filling of the cross-section. Scanning the contour before filling can reduce the edge porosity [63, 107].

For large cross-sections, the area can be divided into a series of smaller, connected areas. Scanning in shorter vectors can decrease deformation (warping) of the part and avoid delamination (the parting of layers) [91, 98, 108]. Shorter vectors also effect the thermal field; some of the heat of the previous vector is used to decrease the required energy to melt the next vector. The influence of the smaller areas' size has been studied both experimentally [98] and mathematically [107]. Incorporating these patterns in more complex parts poses some challenges, solutions to these have been proposed and tested [108].

Sometimes the pattern can be adapted to the part shape. Using a concentric circle pattern can improve the micro-structural homogeneity of cylindrical parts [109].

Scan strategy

The scan strategy encompasses the changes in the scan pattern and process conditions for different layers or different geometrical features.

A gradual change in process parameters can improve the quality of horizontal overhangs. Reducing the power and vector spacing at the onset of the overhang, and gradually increasing the power towards nominal conditions further away improves the geometrical accuracy [94].

Adapted parameters for the first scan vector(s) in a pattern can reduce inhomogeneities in the part surface [30]. Lowering the laser power at the scan vector extremities can also improve the surface quality at the edges of a layer [30]. The varying of the laser power can be taken to the extreme, in the case of pulse shaping. Pulse shaping is a deliberate, pre-configured variation of the laser beam output as a function of time. Pulse shaping can increase layer bonding, reduce spatter or reduce warping [97].

Changing the orientation of the scan vectors in between layers can reduce internal porosity [103, 110] and reduce part distortions [68, 74]. The strategy can also be applied in combination with multiple scan passes over the same surface for a reduction in thermal stresses and the related part distortions [111].

Scanning the same cross-section in multiple passes can improve the porosity, the surface finish of part exteriors [110] and the overall process stability. A first pass at reduced energy followed by a second pass at full power was shown to significantly lower porosity [112] and improve processability [103]. Other research found that this strategy can in fact reduce the surface quality at the edges of a part [30]. Scanning each layer a second time, with parallel vectors, but in between the previous vectors can also reduce internal porosity [110]. A further reduction of porosity can be achieved by scanning a first time at double vector spacing, re-depositing powder at the same layer height and scanning a second time in-between the previous vectors [110, 113]. These last two examples are applications of non-sequential patterns (the vectors are not scanned in order).

To reduce the (often negative) effect on the layer quality of the the first scan vectors, the start point of the pattern can be shifted from layer to layer. This approach has been found to reduce surface inhomogeneities [30].

The powder layer thickness has been related to the amount of residual stress in produced parts. Thicker layers have been found to result in higher residual stresses [99]. Starting with more compact (higher apparent density) layers can result in improved part porosity [102].

Pre-heating

The most common use of powder bed pre-heating is to decrease the cyclical and residual thermal stresses in the part [76, 99, 100, 114]. This can either be achieved by lowering the thermal gradients during the laser scanning or, if the temperature is high enough, by stress-relief. Lowering the thermal stresses prevents warping of the part [76, 99, 114] as well as delamination. The pre-heating can result in demonstrable improvements in the part properties, e.g. the fatigue life [115]. Pre-heating also helps in the homogenization of the mechanical properties [115].

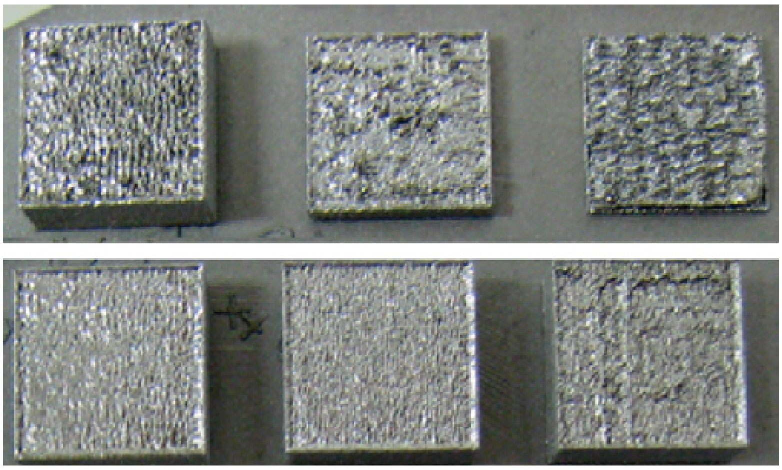

Figure 1.4 – Sample cubes produced without (top) and with (bottom) real-time process control. The scan speeds were 300, 500 and 700 mm/s from left to right, all other parameters were constant [117].

Active process control

A more recent development for SLM is active process control. Based on sensor feedback and a target value, one of the SLM process parameters is adapted in real-time to stabilize the process. For some processes, like laser cladding [116] and laser welding, this is already an established technique.

For SLM, the sensors currently measure part of the radiation emitted below and around the laser beam. The sensor is placed either within the process chamber or outside, using the same optical path as the laser beam to guide the radiation (also called coaxial setup). The control variable is so far always the laser beam power [96, 117].

Active process control requires a good understanding of the process to provide the target value and a good characterization of the process response to changes in the control variable. Currently, the technique has been demonstrated to be useful in decreasing edge overheating [42], improving surface smoothness [117] (Figure 1.4), and improving the quality of horizontal overhangs [95, 96].

1.3.3 Defect detection

The detection of the various defects is an important step towards increased process confidence. Understanding the defects and the conditions in which they occur can lead to better processing strategies. Critical defect detection can save time by aborting the process before completion or by removing the defective part from the process queue if multiple parts are produced simultaneously. The focus here is on defect detection during the process, called on-line process monitoring.

Process monitoring

Already in place for other manufacturing processes as laser welding, cladding and classical manufacturing processes [19, 47, 116, 118–121], online monitoring is an effective method to control part quality. Different methods and sensor types exist for process monitoring of laser material processing. Most frequently used are the observation of back reflected laser radiation (for the most popular laser sources at a wavelength of λ = 1060-1070 nm), plasma induced radiation (λ = 400 nm to 650 nm) and thermal radiation (λ = 900 nm to 2300 nm). The used detectors can be separated into two types: spatially integrating, e.g. photodiodes and spatially resolving, e.g. CCD and CMOS-cameras [122].

The Katholieke Universiteit Leuven has a long tradition in melt pool on-line monitoring [63, 95, 96, 117, 123–125]. An in-process system based on a high speed CMOS camera (10 kHz, 20x16 pixels) and photodiode has been developed. The camera and photodiode look at the process through the beam deflection unit and thus the system is capable of observing the melt pool at all times during the process, regardless of the movement of the laser spot. The CMOS camera and photodiode can extract information from the melt pool radiation. The photodiode integrates all melt pool radiation whereas the CMOS camera provides a two-dimensional image from which the melt pool geometry can be extracted. Some post-processing steps such as thresholding and filtering of tiny particles around the melt pool are required before the extraction of melt pool geometry giving the melt width, area or length. An important application of the monitoring data is mapping [125]. This visualization technique correlates each data point to the physical location where it was taken. The resulting image gives more information about structural defects as overheating and de-lamination (Figure 1.5).

On the basis of this type of image processing, it is shown that the size of the bath increases almost linearly with respect to the laser power and decreases exponentially with the scanning speed. In addition, there is a correlation between the size of the bath and the signal of the photodiode. With this system, many problems related to excessive oxygen, powder layering failures, dirt on optics and sub-optimal process parameters, can be detected during or after the process [124]. For instance, the build can be stopped if it will not succeed due to some problems such as excessive powder feed and insufficient melting of the thick layers. Stopping the build may prevent any possible material waste and extra effort to recycle the deposited and unused powder.

In the Ecole Nationale d’Ingénieurs de Saint-Etienne (ENISE) a monitoring system was developed to visualize the melting of metallic powders [14, 61, 126–128]. Visualization is carried out using LED illumination and a CCD-camera. A photodiode-based, two-wavelength pyrometer is used to measure the maximum surface temperature in the irradiation spot. It is found that the maximum temperature value is rather sensitive to deviations of SLM parameters from their optimum values. For example, a sharp temperature increase and its instability indicate that the energy input per unit length of beam scanning should be decreased. The monitoring equipment can also help in assessing process parameters like the scan vector spacing, the layer

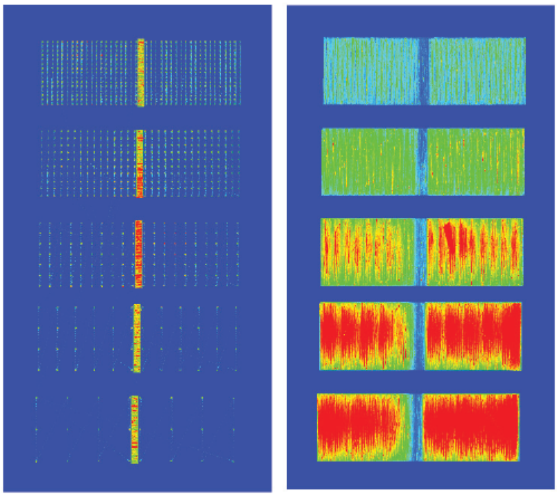

Figure 1.5 – Melt pool data mapping - detection of overheating at overhangs for varying support structures [125].

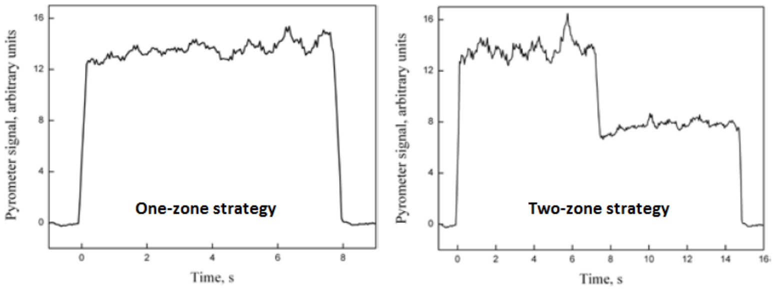

Figure 1.6 – The use of process monitoring for process characterization. Pyrometer output for the scanning of two simple squares, one using a simple one-zone parallel scanning strategy (left) and one using a two-zone scanning strategy (right) [112].

thickness and the scan pattern type [112] (Figure 1.6). For example, the measured temperature decreases with increasing vector spacing, and increases with increasing layer thickness. The camera output was detailed enough to detect overheating at the start of scan lines and the ejection of molten droplets from the melt pool. Extensive quantification of the characteristics of these droplets was carried out [14].

The Fraunhofer-Institute in Aachen uses a mix of the previous techniques [122]. The image information from the processing area is transmitted back through the laser beam optical system. Imaging at high scanning velocities with a high resolution requires an additional external illumination source.

While the previous systems use the laser optical path for the monitoring system (coaxial setup), there are also systems which directly view the processing surface. The sensors can be normal cameras or pyrometers. This technique allows for a larger field of view and the characterization of the thermal field around the melt-pool over multiple scan vectors. The technique has been applied to the investigation of the influence of a wide array of process parameters as: beam power, scan speed, vector spacing, vector length and layer thickness [129].

1.3.4 Defect repair

A combination of process monitoring and repair scan strategies can be implemented to detect defects and attempt a repair. For example a region with insufficient melting (laser beam occluded, more thermal losses through the part) can be repaired by re-scanning the specific region. Excessive surface rugosity could be remedied in the same way, preventing a process shutdown [103, 112]. Up to now, no concrete implementations of real-time repair strategies have been reported. However, the use of laser remelting for crack repair or stress relief has been explored [130].

1.3.5 Post-processing

Post-processing can add a significant workload to the SLM process [15]. Part removal from the build surface often requires wire cutting or electro-erosion [124]. Faces which form part of an assembly often require surface finishes [78] or precision milling [78]. Even normal faces may need to be treated due to the sintering of powder in the heat affected zone surrounding the solidified material [131]. Powder removal can be tricky for parts with complex internal structures which have to conform to strict hygienic conditions (e.g. implants). Some techniques have been reported which can decrease the post-processing time [81].

Adaptive surface quality

Scan strategies which result in a smoother surface layer can be selectively applied to external faces of the parts. Solutions exist for upwards facing surfaces [112, 124], downward facing surfaces [94] and vertical surfaces [107]. These techniques can decrease the need for post-process surface finishing operations [132].

Support-free construction

Optimized process strategies [35, 107] and low expansion coefficient alloys or eutectic alloys [81] reduce the need for additional supports at overhangs. This can significantly reduce the post-processing effort. Analysis of the build process by optical sensors can help in optimizing the use of these support structures [125] (Figure 1.5).

1.4 Versatility

The following section groups SLM innovations which increase the versatility of SLM. This can be related to material properties, new materials or new applications for the SLM process.

Expanding the applications often leads to equipment cost reductions, incites more research efforts and increases machine utilization.

1.4.1 Physical properties

The physical properties of dense, defect-free parts are largely defined by the material micro-structure. The SLM process often results in performant micro-structures as built, though post-process heat-treatments can be used to tune the properties as desired.

Micro-structure formation

The rapid heating and cooling -up to several $10^6\ \mathrm{K\,s^{-1}}$ [16]- which is characteristic for the SLM process is particularly suited for creating very fine micro-structures. Significant research has ben performed on the implications for the mechanical properties. An ultra-fine lamellar $\alpha + \beta$ micro-structure (200-300 nm) in Ti-6Al-4V resulted in both a yield strength and ductility improvement over electron beam melting and mill-annealing [133].

The fast cooling allows the preservation of meta-stable micro-structures. The combination of hard martensitic phases and the fine grains can significantly improve the part wear rate (40% lower wear rate compared to cast samples) [134].

The micro-structure, in particular the preferred crystallographic orientation and the size distribution of the grains, can be tailored by varying the process parameters [109, 135]. This flexibility can be used to optimize the (anisotropic) mechanical properties for specific load cases [80].

The SLM process is also interesting for the field of high entropy alloys. High entropy alloys are multi-component alloys (typically >5 components) with either very complex micro-structures or a single-phase solid solution. This class of metals is very promising for the development of new specialized alloys. FeCoCrNi samples with a single-phase micro-structure have been produced [72]. The mechanical properties are superior compared to arc-melting and casting of the same alloy and comparable to SLM produced stainless steels. The increased performance is attributed to the finer micro-structure.

Heat-treatment

Post-process heat-treatments are applied for various reasons. The fast cooling and the repeated thermal cycles due to the layered process can result in high internal stresses. Stress-relief heat treatments can result in improved ductility, especially when performed under increased pressure (HIP) [34].

Peak hardening of SLM produced AlSi10Mg samples can increase the (high-cycle) fatigue resistance and decrease the build orientation induced anisotropy of the properties [115].

Annealing heat treatments can incite precipitation, increasing the yield strength, ultimate tensile strength [34] or hardness [91, 136].

1.4.2 Novel materials

The SLM process is increasingly applied to the production of metal matrix composites, where the reinforcement is usually a particulate ceramic. These materials lead to, for example, light weight materials with increased strength, hardness, wear resistance and/or thermal stability. The SLM process has some key advantages compared to the processes currently used (arc melting, stir casting, sintering). These advantages include better homogeneity and higher interface strength [137, 138]. In-situ formation of the reinforcing particles can result in even better homogeneity and smaller reinforcement sizes [137–139].

Functionally graded materials are materials with locally varying compositions. The technique has been researched for tool steel (H13) - copper mixtures with the goal of creating regions with higher thermal conductivity in hard cutting tools [113].

The production of shape memory alloys has been researched [109]. The SLM process allows (limited) control of the transformation temperature by varying the laser scan speed.

1.4.3 Novel applications

Originally the SLM was mainly applied to (functional) prototypes and tools for use in other production processes (molds [140], cutting tools, dies [4, 21, 113]). Better part quality and increased process understanding have expanded the application field to the medical sector (implants, surgical aids) and the aeronautics sector [10].

There are still areas where the SLM process can get a foothold. An example is the electronics and sensors sector, which require a downscaling of the process. Research into even thinner layering devices [141] is one example which can further develop this field.

1.5 Conclusion

It is clear that there are many aspects of the SLM process where improvements are both possible and actively researched. Each of these aspects is quite complex and oftentimes an actual improvement in productivity depends on the interaction and trade-offs between multiple aspects. Table 1.2 gives an overview of the treated aspects and how they interact.

The effort is concentrated around improved understanding of material properties and physical mechanisms, integration of diagnostic sensors, hardware improvements and increasingly intelligent software solutions. The following thesis topics concentrate mainly on the understanding of the physical mechanisms and related diagnostic techniques.

Table 1.2 – SLM process productivity aspects and the related benefits and drawbacks.

Aspect	Positive influences	Negative influences
Raw productivity		
High power lasers	Laser scanning time	Process optimization time
Multiple lasers	Laser scanning time	Scan path complexity
Alternative energy sources	Laser scanning time	Material properties, process stability, part extraction cool-down
Energy optimization	Laser scanning time, energy usage	Process optimization time, strategy complexity
Structural optimization	Laser scanning time, material usage	Process data generation, 3D model optimization, requires good mechanical property prediction
System identification	Laser scanning time, geometric tolerance optimization	Scan path complexity
Process understanding	Laser scanning time, process stability, parameter optimization	requires large research effort
Effective productivity		
Defect reduction	Failure rate, mechanical properties	Process optimization time
Defect detection	Lasing time, qualification	Detection calibration time, process control complexity
Defect repair	Failure rate, mechanical properties	Laser scanning time, process control complexity

2 General materials and methods

2.1 Introduction

This chapter introduces the main equipment, materials and methods which are used by most of the experimental procedures of the next chapters.

2.2 Selective Laser Melting machine

Almost all of the experiments in this work are performed on an in-house built SLM machine [50, 142] (Figure 2.1). The base machine is composed of a vacuum chamber with gas inlets for atmosphere composition control. Vacuums up to 10^{-4} bar are possible and the available fill gases are Nitrogen and Argon.

The chamber has a circular build platform with a 100 mm diameter and approximately 60 mm of vertical travel (z-axis).

The main laser source is an IPG Ytterbium fiber laser with a 500 W maximum output, a Gaussian beam profile, a minimum beam waist of 57 µm and a wavelength of 1070 nm. The laser beam is displaced by a 2-mirror scan head with an $f-\theta$ focusing lens with a focal distance of 714 mm. The scan head mirrors are controlled by a XY-200 controller, while the general beam path and laser beam control is assured by a Cambridge Technology SM1000 controller.

For the powder layering, the system can be configured in several ways to allow deposition by a sieve and roller system or by a hopper and rake system. The execution of the layering and lasing steps is performed by a PC with custom software, programmed in National Instruments LabVIEW as part of this thesis.

The base machine can be equipped with a diverse series of measurement devices, such as thermocouples, cameras or photodiode systems. These will be further detailed in the relevant chapters.

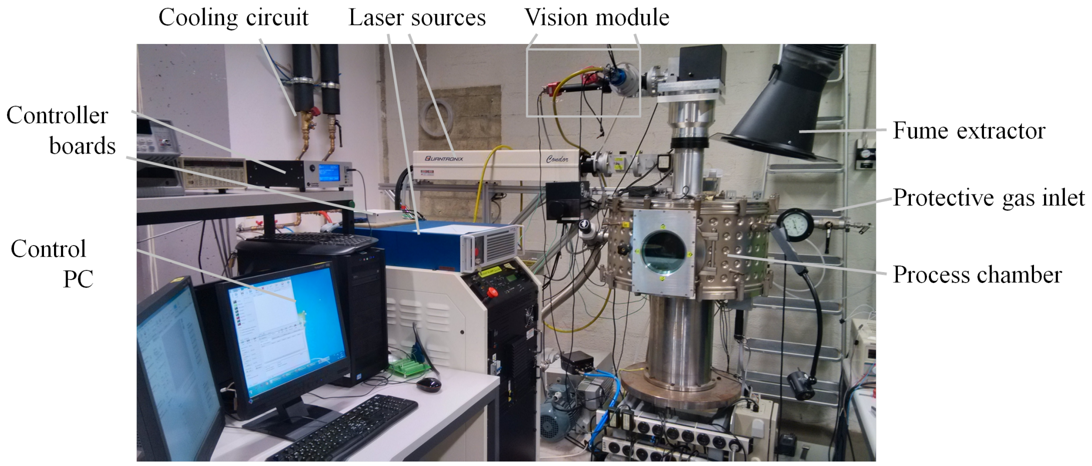

Figure 2.1 – Photograph of the experimental SLM machine setup.

2.3 Reference materials

Four materials are selected as the base reference materials for the experiments. The first is a Maraging 300 type steel (SandvikOsprey), the second is an AlSi10Mg alloy (AvioProp), the third is commercially pure silver (Nippon Atomized Metal Powders Corporation) and the fourth is a commercially pure titanium (PyroGenesis). The first two are commonly used both in SLM processes and in traditional processes. The Maraging steel is suitable for dies, tools and in general applications which require high tensile strength at elevated temperatures. The AlSi10Mg alloy is used in lightweight aerospace structures. After precipitation hardening a high specific tensile strength is achieved. The silver has potential applications for the (Swiss) jewelery sector. Titanium is used in lightweight structures and medical tools and implants.

The materials have also been selected because of their varying physical properties. The silver and aluminum alloy have a much higher thermal conductivity and reflectance compared to the steel and titanium. This difference will be exploited in the chapters on thermal conductivity and radiation absorption. The silver powder is also interesting because of the small granule size and spherical particles. The AlSi10Mg alloy consists predominantly of large, irregular particles. The Maraging steel powder consists mostly of spherical particles, but the larger particles often have small particles (satellites) attached. This limits the flowability of the powder. The Titanium particles are spherical and smooth and the powder flows very well. Custom powder deposition strategies have been developed for each powder.

The powder properties are detailed in Table 2.1. Figure 2.2 shows the powder morphology. The powder composition and particle size are as stated in the material data sheet or accompanying manufacturer information. The relative densities were obtained using the procedure in Section 2.4.2. A summary of thermal and physical properties for the equivalent bulk materials is provided in Table 2.2.

Table 2.1 – Chemical and physical properties of the reference powders.

	Maraging 300 steel	AlSi10Mg	Silver	Titanium
Composition	Fe 60 – 70; Ni 10 – 20; Co 0 – 10; Mo 0 – 10; Al 0 – 10	Al 80 – 90; Si 9 – 11; Mg 0.2 – 0.5	Ag > 99.9	Ti > 99.6
Particle size [µm]; 10%,50%,90%	3.5, 8.2, 9.4	20-63	3.1, 5.5, 8.9	8.0, 14.3, 24.1
Particle shape	Spherical, satellites	Irregular	Spherical, non-smooth	Spherical, smooth
Bulk density $[\mathrm{kg\,m^{-3}}]$	8.26×10^3	2.68×10^3	10.49×10^3	4.50×10^3
Apparent density - deposited [%]	44	49	31	57
Apparent density - tapped [%]	60	58	51	65

Table 2.2 – Thermal and mechanical properties for the reference materials in bulk form.

	Maraging 300 steel (SLM, as-built) [143]	AlSi10Mg [144]	Silver (c.p., annealed) [145]	Titanium (c.p.) [146]
Heat capacity $[\mathrm{J\,kg^{-1}\,K^{-1}}]$	540	960	230	530
Thermal conductivity $[\mathrm{W\,m^{-1}\,K^{-1}}]$	19-21	113	419	17
Melting point [°C]	1427-1454	557-596	962	1650-1670
Heat of fusion $[\mathrm{J\,kg^{-1}}]$	247×10^3	389×10^3	105×10^3	435×10^3
Elastic modulus [GPa]	160-200	71	76	116
Yield strength [MPa]	900-1100	170	/	140
UTS [MPa]	1000-1200	300	140	220

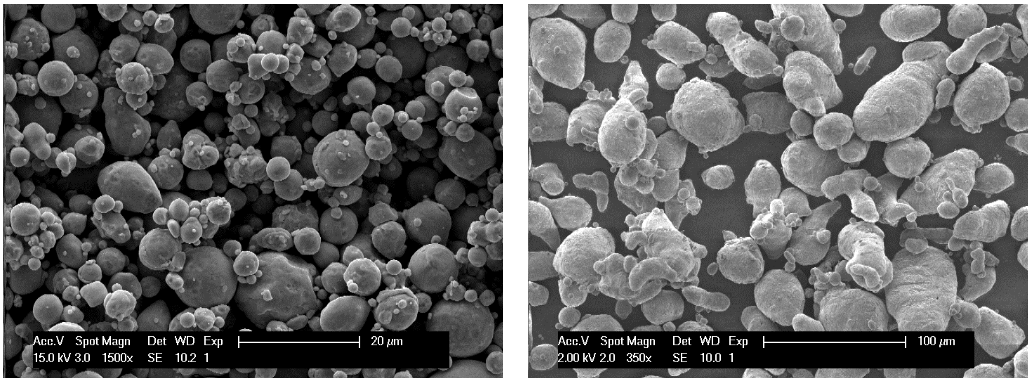
Acc.V Spot Magn Det WD Exp 20 µm
15.0 kV 3.0 1500x SE 10.2 1
Acc.V Spot Magn Det WD Exp 100 µm
2.00 kV 2.0 350x SE 10.0 1

(a) Maraging 300 steel

(b) AlSi10Mg

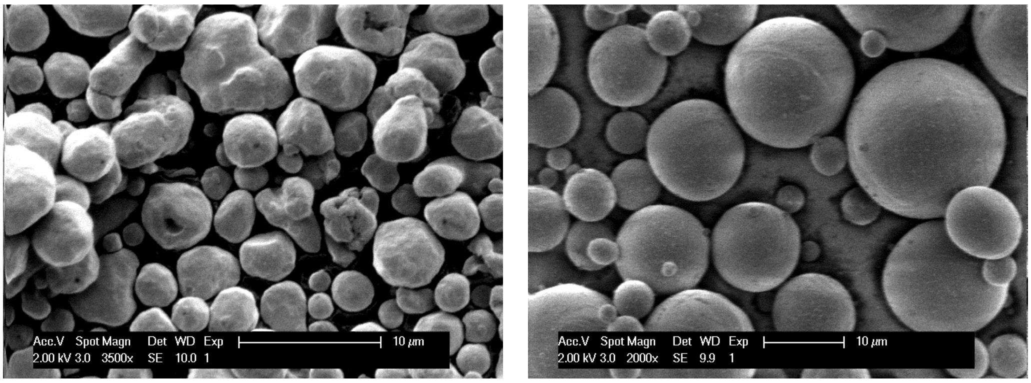
Acc.V Spot Magn Det WD Exp 10 µm
2.00 kV 3.0 3500x SE 10.0 1
Acc.V Spot Magn Det WD Exp 10 µm
2.00 kV 3.0 2000x SE 9.9 1

(c) Silver

(d) Titanium

Figure 2.2 – Micrographs showing the reference powder morphology.

2.4 Additional methods

2.4.1 Microscopy

The various optical micrographs are obtained by an Olympus SZX10 stereo-microscope. The electron microscope micrographs are obtained using a FEI XLF-30 FEG scanning electron microscope. Both backscattered electron (BSE) and secondary electron (SE) images are available.

2.4.2 Powder apparent density

The apparent densities in Table 2.1 are obtained using a volumetric cup (24.80 cm^3). The density is measured after gentle deposition (deposited) and after manual tapping (>50 times, tapped) using an extension cylinder. The extension cylinder is lifted and excess powder is removed by a scraper blade. Weighing of the powder contents and division by the cup volume yields the apparent density. Each measurements is repeated at least five times. The densities are presented as a fraction of the bulk density.

3 Radiation-material interaction

3.1 Introduction

3.1.1 Aim

The aim of this chapter is to improve the understanding of the radiation-material interaction and the influence of the melting process. The principal characteristic for this interaction is the absorptance, or the ratio of the energy absorbed by the material to the total incoming energy.

The absorptance defines a part of the efficiency of the process, but has also implications for the stability of the process. The material undergoes large physical changes during the melting phase. This changes the momentary uptake of energy (absorptance) and modifies the energy balance.

The experimental measurement of the absorptance during the radiation-material interaction is used to study the qualitative material changes and the dynamics thereof. The aim is to obtain a description of the energy uptake which is representative for the SLM process. The results can be used in material selection and for numerical simulation models.

3.1.2 Methodology

A methodology has been defined to carry out absorptance measurements as close as possible to SLM conditions. The followed steps are:

- Design and implementation of an absorptance measurement system, capable of working in conditions close to SLM;
- Validation of the system by correlation with existing data;
- Validation of the system for conditions with no comparable, existing results;
- Measurement of the absorptance change in conditions closely mimicking the process.

The definition of ‘close to SLM conditions’ for this work means a comparable:

- Powder bed state;
- Beam type, size and power;
- Timescale of the absorption event.

The measurements close to SLM conditions gradually increase in complexity. The steps are:

- Measurement of the absorptance in the initial and final material states, specifically the powder bed and the fully dense solid, at room temperature;
- Measurement of the absorptance during a controlled transition between these states, emulated by short beam pulses using a static beam.

3.1.3 State of the art

A more extensive description of radiation absorption in SLM can be found in Section 1.2.7. The general state is that it has been demonstrated that both the surface roughness and surface oxidation level can significantly alter the radiation absorption for solid surfaces [46]. Xie et al. (1999) [49] carried out absorptance measurements on molten metals, using different types of lasers. The absorptance of powders for application in SLS and SLM has been studied by Tolochko et al. [45] and Furumoto et al. [58]. Both used an integrating sphere type setup.

3.1.4 Novelty

The previous research measures the absorption properties mainly for a stable material state (exceptions [45, 49, 55]). The conditions were also selected in a way to avoid effects which can decrease the measurement accuracy, resulting in a low energy flux and longer measurement times.

The current work includes a study of what actually happens during the melting and solidification of the original powdered material and the effect of non-idealized conditions. These include higher energy fluxes and shorter exposure events, as well as possible oxidation effects.

3.2 Design and implementation

3.2.1 Method selection

There are several methods for measuring the absorptance of a material. Most can be categorized as reflection based or based on caloric measurements. Direct reflection methods were not suitable because of the strong diffuse reflection component and the in-homogeneity of the diffuse reflection. Caloric measurements are not compatible with the time scale and spatial resolution of the measurements.

The selected method is an indirect reflection based method, often referred to as the integrating sphere method or Ulbright sphere method. The method homogenizes the total diffuse reflection, and optionally also the specular reflection. Drawbacks of the method are the need of a reference standard and the sensitivity of the sphere inner surface to powder blowout.

3.2.2 Implementation

The integrating sphere has an internal diameter of 95 mm and contains three port holes. One is a rectangular laser beam entry hole of 15 by 5 mm; one a circular sample hole of 8 mm diameter and one a circular detector hole of 2.7 mm diameter. The total surface area of the port holes amounts to 2.3% of the integrating sphere surface. The detector port hole contains an SM1 threaded fixture suitable for the attachment of a photodiode, possibly in combination with 1″ diameter optical filters. The port holes are constructed so that no direct reflections can reach the sensor chip of the detector. The integrating sphere coating consists of a 1.8 mm thick layer of Gesso paint, applied in > 10 layers and polished.

The integrating sphere is equipped with a Thorlabs PDA36A, Si-based, photodiode with a measurement range of 350-1100 nm and a sensor area of 13 mm^2. The photodiode has a built-in amplifier with an amplification factor between 0 and 70 dB (Figure 3.1).

3.2.3 Integration

The designed setup is compatible with the in-house developed SLM machine, as described in Section 2.2 and shown in Figure 3.2. The integrating sphere replaces the powder container of the sieve and roller powder layering device. Sample holders can be placed on a specially prepared substrate plate. The laser beam follows the same optical path as during normal SLM operation, as depicted in Figure 3.1. In this case, the beam passes the collimator, the beam splitter mirror of the Vision sensor system (optional), the CTI scan head with the $f\theta$-lens and a protective glass, to finally enter the process chamber. The target sample can be introduced in the focal plane of the laser beam, or at a specific de-focus distance. De-focus is possible by using a raised platform for the integrating sphere and the z-axis of the table for raising the target sample.

Custom samples were machined from the reference materials (Section 2.3). The sample surface is circular with a diameter of 6 mm. Some samples have a top surface which is at an angle with the measurement plane in order to study the effect of specular reflections and to validate the sphere homogeneity (Figure 3.3). Small cups for powder samples are prepared in the same shape, with inner dimensions of 4 mm diameter and 3 mm depth. Non-standard solid samples are simply positioned on top of a standard sample holder.

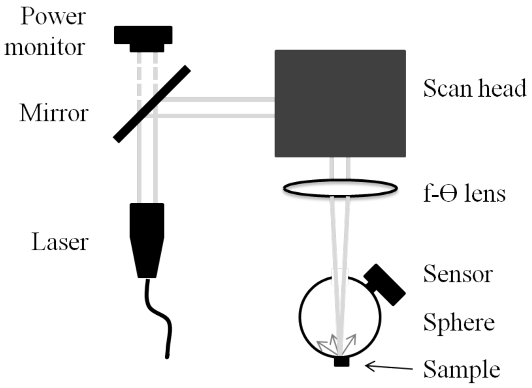
Power monitor
Mirror
Laser
Scan head
f-Θ lens
Sensor
Sphere
Sample

Figure 3.1 – Schematic of the laser beam path for integrating sphere measurements.

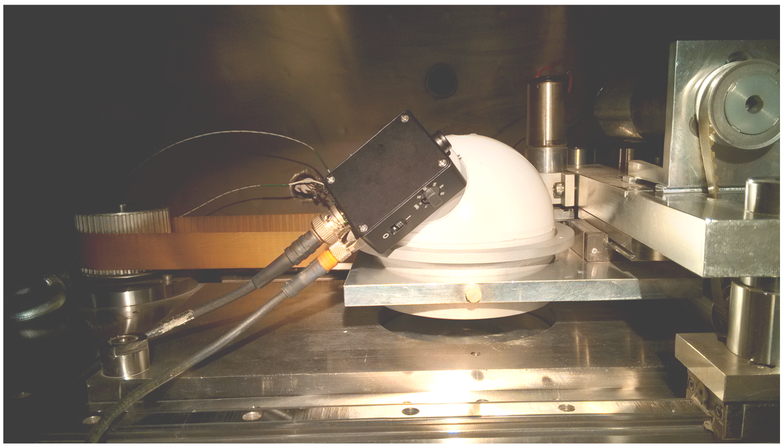

Figure 3.2 – Picture of the integrating sphere setup in high flux mode, inside the SLM process chamber.

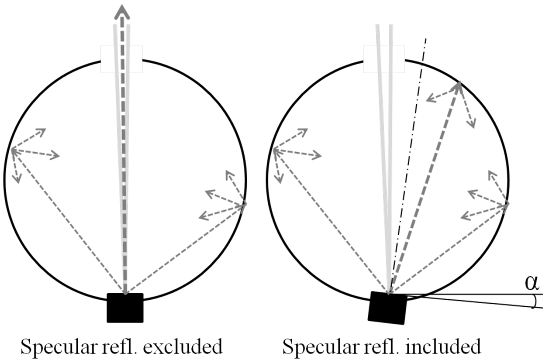
α
Specular refl. excluded
Specular refl. included

Figure 3.3 – Demonstration of the sample placement for the measurement of the specular reflection component.

Table 3.1 – Absorptance values for the calibration materials.

Material	Absorptance	Source
Fine polished aluminium	5%	Wijers et al. 1996 [27]
	6%	Xie et al. 1999 [49]
Rough polished aluminium	30%	Nicolle et al. 1969 [147]
	10-21%	Xie et al. 1999 [49]

3.3 Materials

3.3.1 Calibration materials

The calibration material is an Aluminum 7075-T6 (AlZn5.5MgCu). Two surface preparation methods are considered, one polished at 320 grit (Ra ~ 0.25 µm), the second polished down to 4000 grit (Ra <0.1 µm) using SiC coated paper.

Values for the reflectivity of the reference materials are obtained from literature (Table 3.1). These are values for similarly rough material surfaces for radiation at the same approximate wavelength (1060-1070 nm).

3.3.2 Sample materials

The three base materials as described in Section 2.3 are used for the powder samples. The samples are prepared by gentle deposition of an excess of powder in the sample holder, followed by removal of the excess powder by a scraper blade.

The dense Maraging steel samples are produced in-house by SLM. The oxidized sample is produced in normal atmosphere. For the base sample the production chamber's atmosphere was evacuated (to $\pm 5 \times 10^{-5}$ atm) and subsequently filled with Argon gas. All other processing steps and conditions are equal. After processing, the samples are cleaned using pressured air.

3.4 Methods

3.4.1 Calibration and validation

The integrating sphere method requires reference standards with a known absorptance for the calibration of the sphere/sensor combination. Furthermore, validation measurements are performed for sensor linearity and sphere homogeneity with regard to angle of incidence of the beam and the in-plane sample orientation.

The calibration is performed for two beam flux densities (energy per unit of surface and unit of time). The flux density is varied by off-setting the sample from the laser beam focal point, which increases the beam area. The first series of measurements has the sample surface at 80

Table 3.2 – Overview of the various calibration conditions.

Beam power	Sample de-focus	Angle of incidence	Surface polish
30 W, 30-100 W	0 mm, 80 mm	90°, 85°, 80°	320 grit, 4000 grit

mm offset from the beam focal point (de-focus) in order to create a larger sampling surface and have a lower beam intensity. These are referred to as the low flux (density) measurements. The second series of measurements has the sample surface at the beam focal plane, where it has a waist of about 57 μm. These are referred to as the high flux (density) measurements.

The standard input beam power is 30 W. For the linearity validation the beam power is increased from 30 to 100 W, in steps of 10 W. The effect of the angle of incidence is measured for angles of 90°, 85° and 80°, relative to the sample surface. The 90° measurement excludes specular reflections (Figure 3.3). The sphere homogeneity is verified by rotating the (inclined) samples by approximately 90° around the beam axis between measurements. The test conditions are summarized in Table 3.2.

Each measurement series consists of samples taken at 8 different locations. Between each series the sample surface is re-polished and cleaned. The tests are all performed under normal atmospheric conditions.

3.4.2 Measurement procedure

The measurements with a stationary beam are performed with modulated pulses of the laser beam. The beam output during a pulse is constant, except for the on/off transients which take approximately 20 μs for the on-transient and 20-50 μs for the off-transient, as measured by a high-speed photodiode coupled to an oscilloscope. The beam output is 30 W, measured at the sample surface.

Again 8 positions are sampled per measurement, with sufficient time between pulses and after displacements to stabilize the powder surface and the beam position.

3.4.3 Data-acquisition

For the low beam flux samples, a single measurement pulse has a duration of 100 ms with a sampling rate of 500 samples per second. The measurements at high beam flux -with the sample at the laser beam focal point- are performed for either 2 ms with a sampling rate of 50 000 samples per second or for 0.5 ms with a sampling rate of 100 000 samples per second. These settings result in 50-200 data points per sample.

A second sensor measures the beam output level, synchronized with the integrating sphere sensor.

3.4.4 Data analysis

For the average absorption calculations the data is analyzed by an automated pulse detection algorithm which uses the second beam output sensor and a thresholding algorithm. The integrating sphere data points are averaged and additional statistical information (median, standard deviation) is stored.

For the dynamic analysis the curves of multiple measurement series are averaged. Approximate models are derived using the least squares method.

3.4.5 Absorptance calculation

The sensors provide readouts of the signal intensity in Volts. The signal intensity is proportional to the average intensity of the reflection. For each measurement, samples are acquired at zero beam intensity to define the zero offset of the sensor signal. This offset is calculated as the average over 50-100 data points and is subtracted from the raw signal:

$$\text{signal} = \text{raw signal} - \text{zero offset}. \tag{3.1}$$

The reflectance of the sample can be calculated by comparing the sample signal to the signal of a reference material with known reflectance, according to:

$$\text{sample reflectance} = \frac{\text{sample signal}}{\text{reference signal}} \times \text{reference reflectance}. \tag{3.2}$$

In some cases an adjustment may be required if the sampling beam power is different from the reference power:

$$\text{sample reflectance} = \frac{\text{sample signal}}{\text{reference signal}} \times \text{reference reflectance} \times \frac{\text{reference power}}{\text{input power}}. \tag{3.3}$$

Or after grouping the calibration parameters:

$$\text{sample reflectance} = \frac{\text{sample signal}}{\text{input power}} \times \frac{\text{reference reflectance} \times \text{reference power}}{\text{reference signal}}. \tag{3.4}$$

For the calculation of the absorptance, the assumption is made that there is no transmittance of radiation through the sample and that the contribution of emitted radiation is negligible. Under these conditions, the equation simply becomes:

$$\text{sample absorptance} = 100\% - \text{sample reflectance}. \tag{3.5}$$

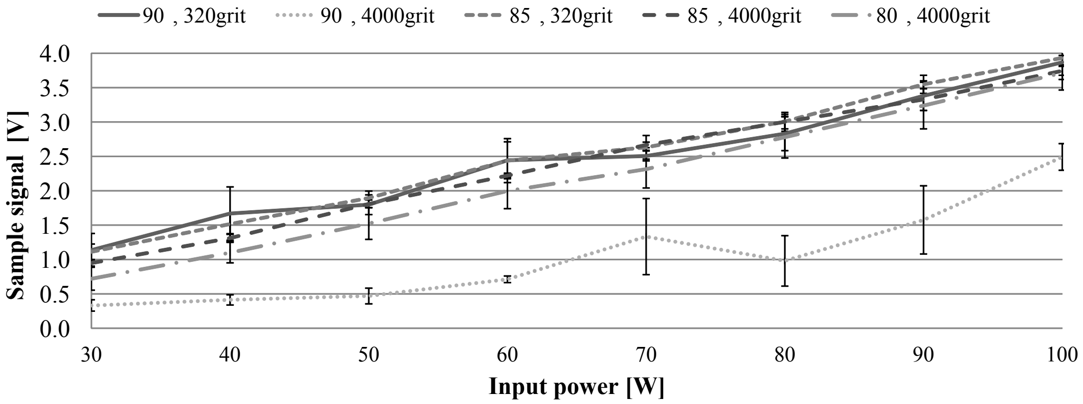

Figure 3.4 – Demonstration of a series of calibration and validation measurements using Aluminum 7075 and a high flux density beam (in-focus).

3.5 Results and discussion

3.5.1 Calibration and validation

Figure 3.4 demonstrates a calibration and validation series for a high flux density beam. It shows the sample signal for varied conditions. Several results can be derived from this data.

The signal value is used for calibrating the integrating sphere. The reference measurement series is the one with a rough polished surface (320grit) and a non-perpendicular angle (85°) to include the specular reflection in the measurement. The reference reflectivity is from Table 3.2. The conversion value for this particular calibration was 0.052 $\mathrm{V W^{-1}}$. The other measurements are used to investigate the sub-properties of the reflection.

The trend in the data for linearly increasing beam powers can validate the linearity of the detector. This is under the conditions that the beam output is stable and the material state does not change significantly. For the reference measurement conditions and the selected power range the trend is confirmed to be linear. The standard deviation of the conversion value over the calibration range was ±2%.

The error bars on the graph represent the standard deviation of the sample signal for 4 samples with a different in-plane orientation. The orientation shift is approximately 90° between each sample. The standard deviation for the reference series is 3 – 10%, for the other conditions it is generally higher and on the order of 10 – 20% or even more for the finer polished surface with perpendicular beam. The standard deviation over the 50-100 data points of a single beam pulse is 3 – 6% for the reference conditions. This means the orientation does not influence the results.

The difference between the 320grit and 4000grit polished surfaces with a perpendicular beam is a measure of the specular and diffuse components of the reflection. It is clear that a 4000grit polish is not yet mirror-like, but the diffuse component of the reflection is only one third compared to the rougher surface. Since the total reflectance is similar, as demonstrated by the measurements at non-perpendicular angles, the specular reflection has to be higher. A higher specular reflection is more sensitive to local variations in the sphere coating, explaining the higher standard deviation between samples. This is compounded by small variations in the surface orientation for the perpendicular samples, causing some portion of the specular reflection to be included in the measurement.

While at non-perpendicular beam angles the sample signal seems lower for the smooth polished samples compared to the rough polished samples, the variation is within measurement error.

3.5.2 Absorptance

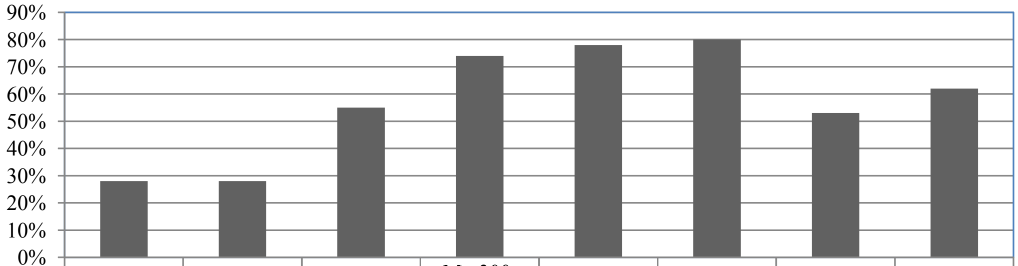

	Al7075, 320grit, low flux	Al7075, 320grit, high flux	Mar300, bulk, low flux	Mar300, bulk, oxidized, low flux	Mar300, powder, low flux	Mar300, powder, high flux	Ag, powder, high flux	AlSi10Mg, powder, high flux
Absorptance	28%	28%	55%	74%	78%	80%	53%	62%

Figure 3.5 – Average absorptance measurements for several materials and material states.

Figure 3.5 groups a series of averaged absorptance values. The obtained results for the bulk Maraging steel (55%) are in line with reported values for non-polished stainless steels (40 – 60% [43]). As previous research pointed out, the absorptance for powders can be significantly higher compared to the dense material state. The effect is increasingly large for highly reflective materials. The absorptance for powdered aluminum (AlSi10Mg) and silver are approximately six and ten times higher, respectively(62% to 5 – 10% for aluminum and 53% to 1 – 5% for silver), compared to reported values for dense, flat samples. For Maraging steel, which has a higher absorptance for the base material, the increase is less than two times (78% vs 55%). No direct comparison with literature is available, however the measured values are in line with those reported for metal powders (65 – 80% [45]).

One observation is the good agreement of the results for the Maraging steel powder for low and high flux density beams. For sufficiently short exposure times a higher flux density can be tolerated. The high flux density measurements also have a small sampling surface, the diameter of which is in the same order of magnitude as the individual powder particles. The current measurements, however, do not show a bias or change in the results.

The direct comparison of the absorptance of powdered materials is not possible with the current results as the powder morphology is different for the three tested materials.

Another observation is the effect an oxidation layer can have on absorptance. The dense Maraging steel samples produced in normal atmosphere presented an oxidized top surface, which seems to greatly increase the absorptance. The hypothesis is that the increase in absorptance is due to the increased surface rugosity by the oxidation layer, rather than through a higher absorption by the oxides. This hypothesis is supported by Bergstrom (2008) [43] who found a 50% increase in absorptance with increasing surface rugosity for stainless steel, and the low absorptance of the oxide particles themselves [45, 46].

Overall, the state of the material under the laser beam and the environmental conditions can greatly affect the absorbed energy during processing.

3.5.3 Absorptance evolution

Figures 3.6 and 3.7 show the evolution of the absorptance for the transition from powder to liquid. The instantaneous absorptance is integrated and multiplied by the beam power to obtain the total energy absorption. Each graph contains a measurement series of 8 samples (graphs in grey). The samples are fitted with a simple logarithmic equation using a least-squares-error fit to demonstrate the trend.

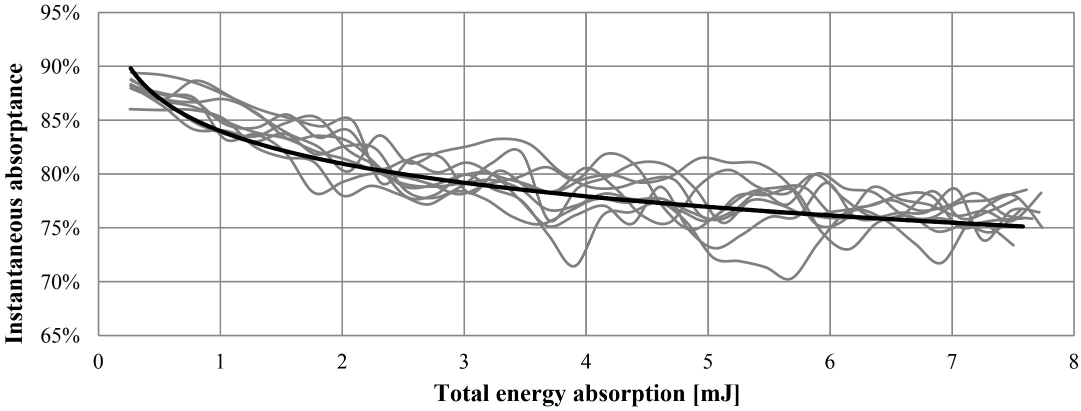

Figure 3.6 – Evolution of the instantaneous absorptance during the transition from powder to liquid metal for Maraging steel. Compilation of 8 measurements (grey) and a least-squares exponential fit (black, $-0.044\ln(x)+0.84$).

A notable observation is that the instantaneous absorptance stays higher than the absorptance of the equivalent dense, flat material. This could be due to the surface of the molten liquid,

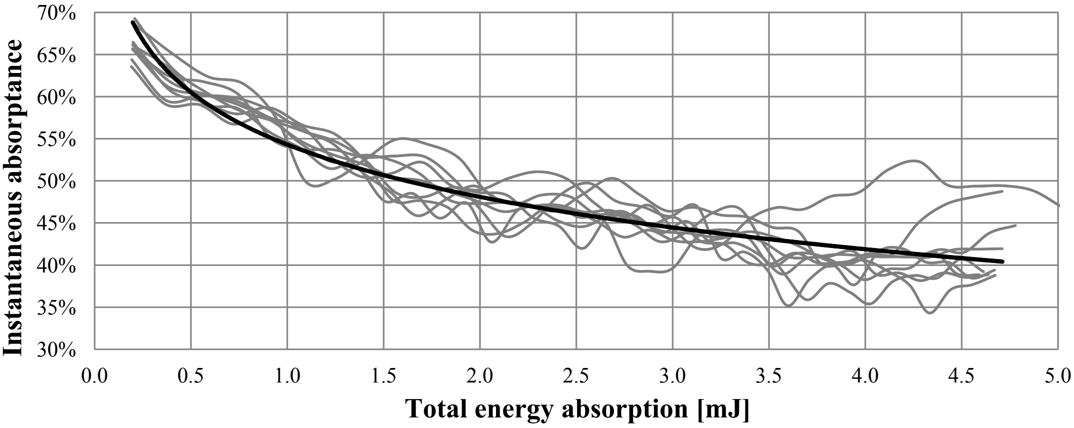

Figure 3.7 – Evolution of the instantaneous absorptance during the transition from powder to liquid metal for commerically pure silver. Compilation of 8 measurements (grey) and a least-squares exponential fit (black, $-0.09\ln(x)+0.54$).

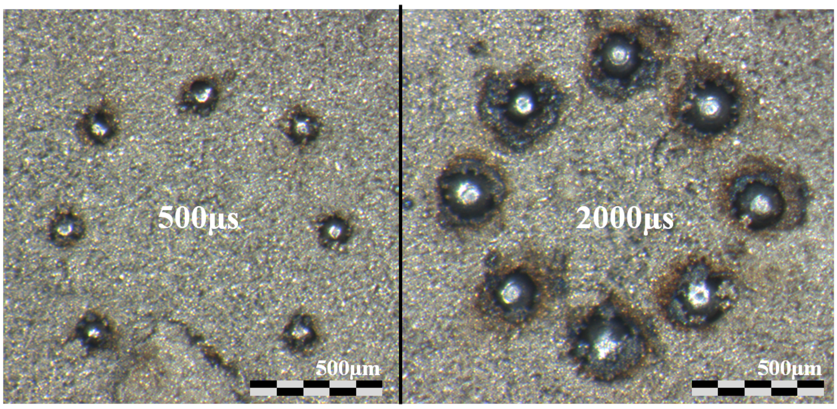

Figure 3.8 – The melting of Maraging steel powder with a static beam. State after 500 µs and 2000 µs of exposure at 30 W beam power, in high flux density mode.

oxides, temperature dependence of the absorption or absorption of a part of the radiation by the surrounding powder. This observation is of importance when absorption properties are used in numerical simulations of the SLM process; standard literature values for the dense material may not represent the reality.

The graphs demonstrate the variation of the absorptance during the transition and variance over multiple samples. If the powder bed quality is good (uniform density and flatness) the absorptance varies only by 5-10 percent points. However, defects in the powder bed can greatly influence the total energy absorption. Increases of the total energy absorption of 50% have been measured. These can significantly change the energy balance. The effect depends on the size and shape of the defect, and the depth of the powder bed. A small crack results

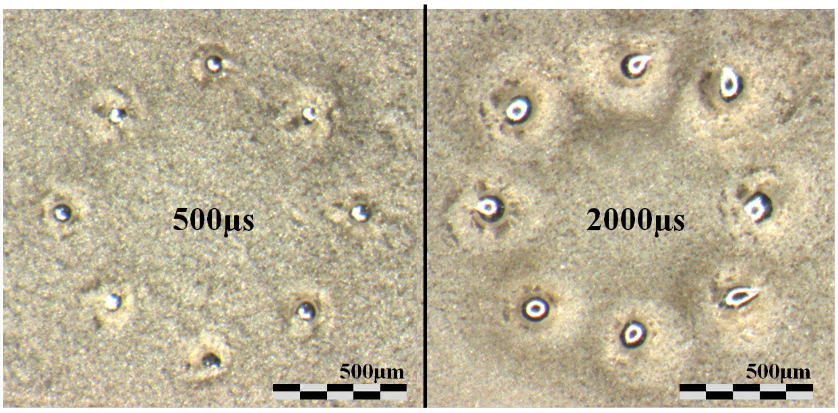

Figure 3.9 – The melting of commercially pure silver powder with a static beam. State after 500 μs and 2000 μs of exposure at 30 W beam power, in high flux density mode.

in higher absorption and less material availability, which can disrupt the melt pool, provoke overheating and/or create pores.

Figures 3.8 and 3.9 show the effect on the material for pulses of different durations. The figures show how the molten material usually takes on a spherical shape due to surface tension forces. The shape change, together with the material shrinkage during the transition from porous powder to dense liquid causes a gap between the liquid and powder. The lower intensity radiation at the edge of the beam and any heat transported through the material also cause (partial) sintering of the powder and create a heat-affected-zone.

3.6 Additional considerations

The current method's implementation relies on the absence of emission of radiation during the absorption event. For some conditions, especially in normal atmosphere, the oxidation of powder particles may cause significant emissions. The sensor also detects radiation in a wide band so thermal emission could disturb the measurement. For the parameters used in this study the thermal radiation is expected to be less than 1% of the reflected beam power. An improved implementation could use optical filters in front of the sensor in order to remove all radiation except for the radiation with a wavelength close to the laser beam's wavelength.

At high beam intensities, the rapid heating and corresponding expansion of the gas/air in between powder particles can cause particles to be ejected from the powder bed. This phenomenon is called powder blowout. When these particles are suspended in the atmosphere they may obstruct the laser beam, altering the measured reflection. The powder particles will eventually be deposited on the sphere's coating and cause contamination, skewing the measurements.

The SLM process often takes place within an enclosure with a protected or non-oxidizing atmosphere. While the experimental setup supports protected atmospheres, the combination with the integrating sphere module was not possible due to powder blowout during the flushing.

The beam power applied during the experiments is lower than the powers which are used nowadays in SLM. The reason is to prevent damages to the sphere coating. However, recent experiences suggest that samples with a low specular reflection component could permit higher powers.

3.7 Conclusion

It is demonstrated that the integrating sphere method can be an effective method for the study of the radiation-material interaction in SLM. The designed implementation is a technologically straightforward way of performing absorptance measurements in SLM conditions. The validity of the setup and the absorptance results have been proven by comparison with available data.

The possible influence of the base material properties, the presence of oxides and the material surface have been studied, though not extensively. The absorptance does not vary much for surface rugosities typical of SLM processed samples. However, the presence of oxides can have a large influence.

The absorptance of the material in the powdered state can be several times higher compared to the dense and flat material state, especially for materials with a low natural absorptance.

Furthermore, the approach can also be applied to the transient behavior of the absorptance during the melting of powder. The results are of particular relevance for numerical simulations. They also demonstrate the importance of a uniform powder bed for maintaining a consistent energy balance.

Overall, the approach presented in this chapter can be of use for SLM machine manufacturers to study material and environmental influences and aid in process optimizations by optimizing the energy absorption for quantity and stability.

4 Heat diffusion in powder beds

4.1 Introduction

This chapter expands on existing methods for characterizing the heat diffusion in packed powder beds. In packed powder beds the heat transport mechanism is characterized by heat diffusion. The diffusion can be quantified by the thermal diffusivity or thermal conductivity of the powder bed. These properties are dependent on the material, the material state and environmental properties (fill gas, temperature, pressure).

4.1.1 Aim

The focus is on the measurement of the effective thermal conductivity for various powder materials in the initial packed bed state or in a partially sintered state. The effective thermal conductivity in the powder state has no direct relation to the melt pool created by the laser beam, but it defines how heat will spread in the surrounding powder. This in turn influences part surface quality and precision. It can also alter material properties as the absorptance, which influences the melting of subsequent tracks.

The general aim of this chapter is to contribute to the available data on the thermal conductivity of powder beds. The implementation is also chosen in such a way as to enable future studies of the thermal conductivity change during powder sintering.

4.1.2 Methodology

The thermal diffusivity is measured using the flash method, with a laser beam to excitate the surface of the powder bed. The thermal conductivity can be derived using the material volumetric density and specific heat capacity.

The flash method is a transient method, which uses information on the change of temperature over time. A laser beam pulse initiates a heat wave which propagates through the powder bed, increasing the local temperature before cooling back down (Figure 4.5). A thermocouple which is embedded in the powder bed below the laser beam center measures the temperature response. The time between the laser pulse and the measurement of the maximum temperature at the position of the sensor is characteristic for the thermal diffusivity.

4.1.3 State of the art

Section 1.2.7 gives an overview of works related to heat transfer in SLM. The flash method has been in use since the 1960's [148], though initially for dense, solid materials. Many different implementations exist, using various geometries for the heat source and different types of sensors for the temperature response registration. The conductivity of powders and other granulated materials has been experimentally studied using transient methods since the 1930's [51].

The experimental study of the thermal conductivity of powders in relation to the SLS/SLM process is more recent [58, 149–151]. All use some form of the flash method. Taylor et al. (2001) [151] use both a stationary and moving laser as the excitation source, a thermocouple as the sensor and the time to maximum temperature as the characteristic. Furumoto et al. (2007) [58] use a similar setup to study the influence of the powder particle size and powder bed (relative) density on the thermal conductivity. Sih et al. (1992) [149] use the rate of temperature increase as the characteristic to measure the thermal conductivity of powders for temperatures up to $100°C$ using a water bath. Rombouts et al. (2005) [150] use a pyroelectric sensor to study the influence of the material composition and the powder bed density.

The basic flash method puts some conflicting requirements on the test conditions:

- Enough energy needs to be delivered to provoke a well-defined temperature rise at the position of the sensor, however, the energy shouldn't alter the material state;
- The sensor should not be too far from the surface to prevent dissipation of the energy, but it should be far enough to consider the beam a point source;
- The duration of the beam exposure should be small compared to the time the thermal front takes to reach the sensor; however, this decreases the delivered energy.

Typical test conditions use a low intensity beam with a relative large cross-section and pulse duration, and place the temperature sensor at 5-10 mm deep in the powder bed. With the assumptions of far enough boundaries and heat transport only by conduction, a simplified heat diffusion model can be used. The model is based on semi-hemispherical diffusion from a point source. Furumoto et al. (2007) [58] pose that for a sufficiently small beam radius to measurement depth ratio (<1.22) and for a sufficiently large time to maximum temperature to pulse duration ratio (>10) the diffusivity is characterized by:

$$\text{diffusivity} = \frac{\text{depth}^2}{6 \times \text{time to max. temperature}}. \tag{4.1}$$

4.1.4 Novelty

Due to the measurement conditions, the usual simplified equations for the calculation of the diffusivity can not be used. A series of finite element simulations of the experiments are used to correlate the time to maximum temperature to the effective diffusivity.

The implementation in this work uses a special type of laser beam as the excitation source. The beam has a ring-like intensity distribution, which lowers the energy density while a higher total energy can be delivered. The higher total energy increases the temperature rise at the point of the sensor. The setup also uses shorter pulse times and a sensor placement which is closer to the surface compared to existing implementations. In the future, this setup can be used to study the change in thermal conductivity for increasingly higher degrees of sintering of the powder bed.

4.2 Design and implementation

4.2.1 Method selection

The flash method was chosen over alternatives for several reasons. The flash method is a transient method, which does not require heating to high temperatures for prolonged periods of time. It also does not require extensive isolation of the measurement volume, which makes integration more practical. The presence of a laser in SLM machines is another plus for integration of the test in the normal processing environment.

There are some drawbacks to integrating the flash method. The equipped SLM laser is not always suitable for the measurements, usually due to a too high energy density. The flash method also has a larger measurement uncertainty compared to alternatives. This is generally due to the sensor positioning error, beam instability, powder bed preparation variations, temperature registration noise and uncertainty on the material density and specific heat capacity.

4.2.2 Implementation

The implemented version of the flash method uses an open powder vessel (Figure 4.1). The vessel is 25 mm in diameter and 10 mm deep. Inside the powder vessel is an adjustable platform (height-axis) composed of PETP polymer. The platform is spring loaded and can be locked using a screw. In the center of the platform is a hole through which the head of a thermocouple protrudes. The sensor is a K-type thermocouple with a 0.25 mm diameter head. The thermocouple wires are guided through the platform and the vessels bottom to the registration equipment.

The powder vessel can be mounted on the SLM machine processing platform. The z-axis of the machine can be used to move the powder bed surface out of the laser beam focal plane

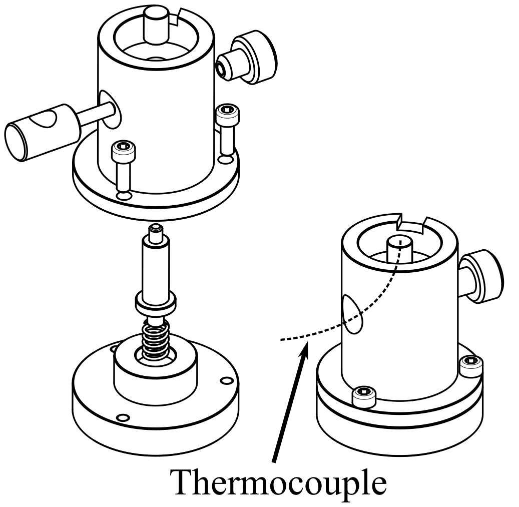

Figure 4.1 – Drawing of the powder vessel with tunable thermocouple depth, used for the thermal conductivity experiments.

(de-focus) in order to reduce the energy density.

The heat diffusion is initiated by one of the laser beams which with the SLM machine can be equipped. The pulse timing is measured either by monitoring the laser modulation signal or by using a photodiode (Thorlabs DET10A) which uses stray laser light. The laser pulse registration is coupled with the temperature registration equipment.

The laser beam is a Quantronix Nd:YAG laser. The laser has a special mode, designated as TEM01*, which results in a ring-shaped intensity profile. The profile expands when the laser is de-focused (Figure 4.2). This mode is used to decrease the energy density and avoid the temperature build-up in the center of the beam. Figure 4.3 shows the powder bed, the laser imprint and the sintered powder cake after repeated exposures.

The manufacturer provided software is used to control the laser beam. The temperature and pulse timing data is registered by an Agilent 34420A. A custom Matlab routine transfers, processes, displays and stores the data.

4.3 Materials and methods

4.3.1 Sample preparation

The main measurements were performed on three powder materials as described in Section 2.3: commercially pure silver, commercially pure titanium and Maraging steel. The samples are prepared by gentle deposition of an excess of powder in the powder vessel, followed by removal of the excess powder by a scraper blade.

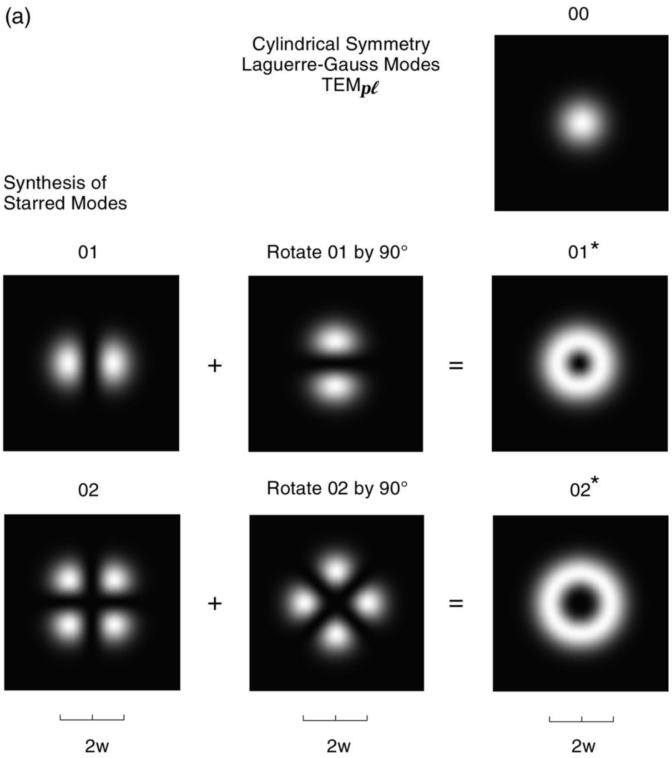
(a)
Cylindrical Symmetry
Laguerre-Gauss Modes
TEM$_{p\ell}$
00
Synthesis of
Starred Modes
01
Rotate 01 by 90°
01*
+
=
02
Rotate 02 by 90°
02*
+
=
2w
2w
2w

Figure 4.2 – Intensity distribution of mono-mode laser beams [152]. The laser has a TEM01* type of beam, which results in a ring-like intensity distribution for randomly polarised beams.

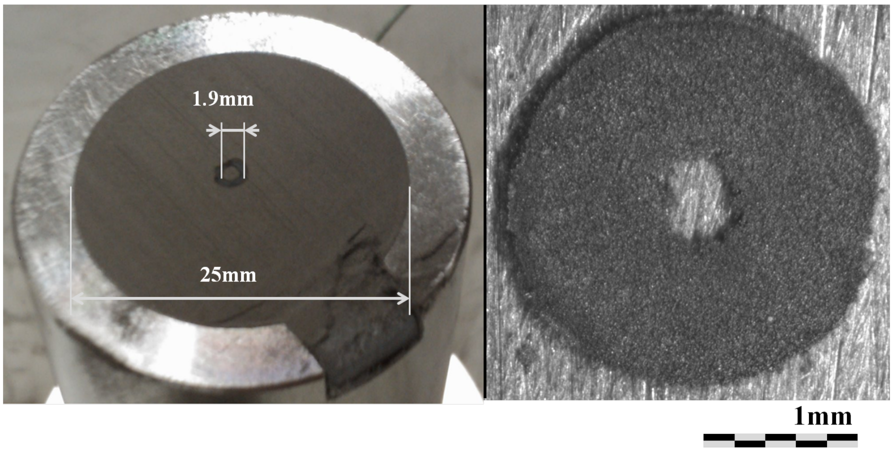
1.9mm
25mm
1mm

Figure 4.3 – Left: Surface of the powder vessel, filled with Maraging steel powder and the mark of the laser beam. Right: Sintered powder cake after repeated exposures.

4.3.2 Calibration

The thermocouple sensor is calibrated using a water-ice bath. However, the exact temperature value is not important for the results. The voltage to temperature conversion is handled by the registration software.

The depth of the sensor is set by a micrometer placed on the top of the powder vessel. The platform containing the sensor is subsequently locked using a screw. The sensor depth is checked by the same procedure after a measurement series. The estimated accuracy for the sensor depth is 0.1 mm.

The laser beam power output is calibrated with a Gentec power meter before each measurement. The power was always accurate to within ±1 W.

4.3.3 Measurement procedure

All measurements are performed under normal atmosphere. The laser beam output is fixed at 13 W, as measured at the sample surface. The sample surface is elevated by 50 mm above the focal plane. This results in a ring-shaped beam with an outer diameter of roughly 2.0 mm and and inner diameter of 1.8 mm. Data samples are acquired at approximately 7 Hz.

Measurements are performed for a range of sensor depths (0.5-2.0 mm) and beam exposure times (4/20/50 ms). 9 measurements are taken for each condition.

4.3.4 Simulation procedure

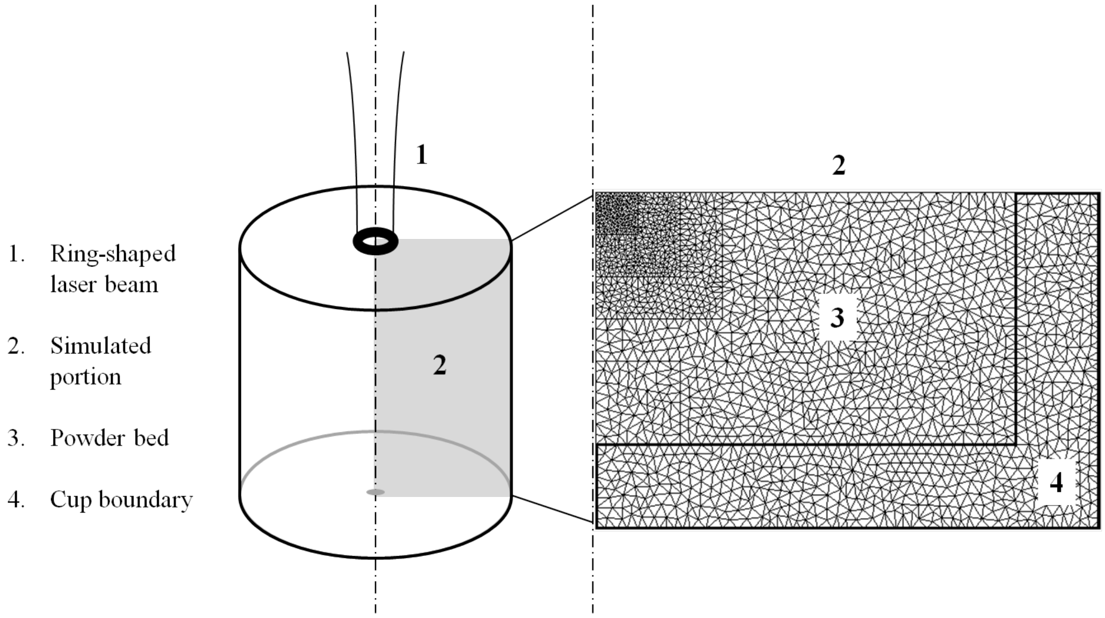

Figure 4.4 – Representation of the simulation area. The software simulates the heat diffusion in a 2D cutout using the axio-symmetric property.

A series of finite element simulations allows to relate the time to maximum temperature to the effective diffusivity of the material. The simulation software is provided by the LGPP laboratory of the Ecole Polytechnique Fédérale de Lausanne. The algorithm uses a simple axio-symmetric geometry, based on a cut-out of the actual powder vessel (Figure 4.4). Heat transport is only possible by conduction (standard heat diffusion equation). The boundaries of the domain are insulated. The laser energy is applied through a ring shape, based on the actual beam size and shape (1.8 mm i.d. - 2 mm o.d.), but with a uniform intensity distribution of 21.8 $\mathrm{W\,mm^{-2}}$. The powder bed is modeled as a homogeneous material with a fixed diffusivity.

Virtual thermocouples are placed at various depths along the symmetry axis. The profile of the temperature over time is recorded and the time to maximum temperature is retrieved (Figure 4.6). Since the time to maximum temperature depends only on the thermal diffusivity parameter and not on any other material parameters, the same series of simulations can be used for a range of materials.

The maximum temperature reached is also dependent on other material parameters as the the density, thermal conductivity and absorptance. The actual temperature values can not be compared between materials.

The simulation is repeated over a range of diffusivities in order to obtain a correlation table. Bundling all the data for a given sensor depth results in correlation curves (Figure 4.7).

4.3.5 Diffusivity and conductivity calculation

The diffusivity is calculated by interpolation of the simulated curve for the specific sensor depth. The thermal conductivity can be further calculated using the powder bed density and material specific heat capacity:

$$\text{conductivity} = \text{diffusivity} \times \text{density} \times \text{heat capacity}. \tag{4.2}$$

4.4 Results and discussion

4.4.1 Measurements

Figure 4.5 contains some example measurement curves. The noise is low, but at test conditions with a small temperature increase there can be significant uncertainty on the time of the maximum temperature. The subsequent calculations use the numerical maximum.

A possible alternative approach is to fit a continuous function to the raw data, and calculate the time to maximum temperature using the fit. According to Furumoto et al. (2007) [58], the time-temperature curve takes the following form:

$$\Delta T = \frac{c_1}{\sqrt{t}}\left(1 - \mathrm{e}^{\frac{-c_2}{t}}\right)\mathrm{e}^{\frac{-c_3}{t}}, \tag{4.3}$$

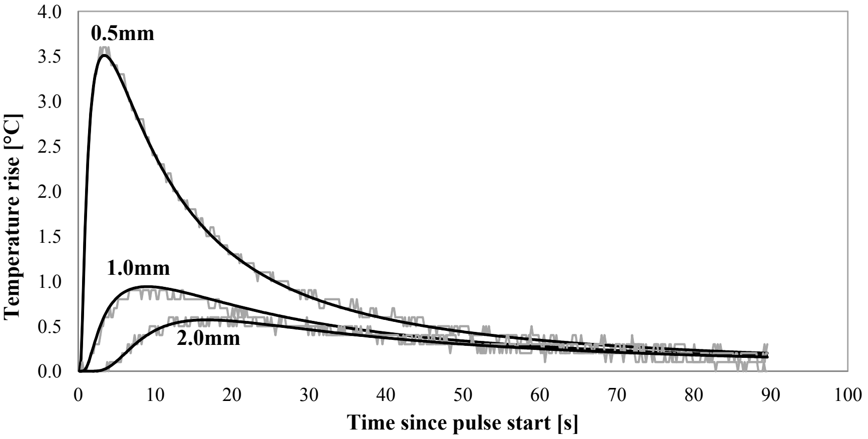

Figure 4.5 – Examples of temperature-time curves for Maraging steel powder, a pulse time of 20 ms and various sensor depths. The grey curves are the raw measurement data, the black curves are fitted models.

with ΔT the temperature rise, t the time since the pulse start and c_1,c_2,c_3 the fit parameters. The fits are included in Figure 4.5 and agree well over the full range of measurement conditions.

4.4.2 Simulations

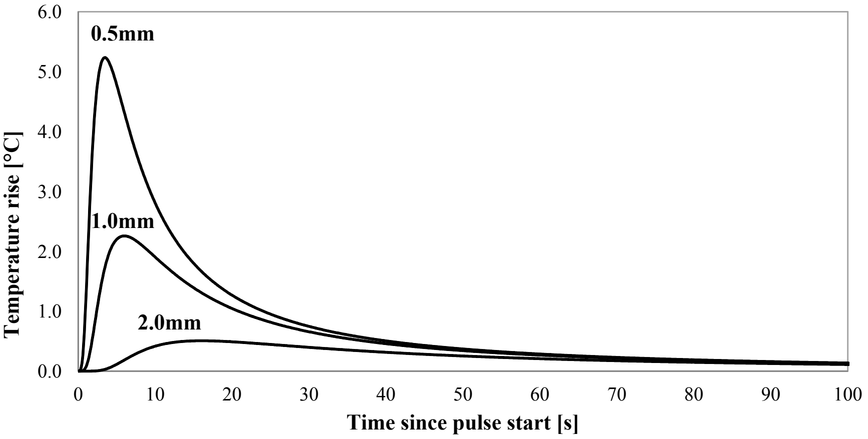

Figure 4.6 – Examples of simulated temperature-time curves for Maraging steel powder.

Figure 4.6 contains some simulated curves for equivalent conditions as figure Figure 4.5. The difference in maximum temperature does not impact the time to maximum temperature.

The time to maximum temperature for all the simulated curves results in Figure 4.7. These graphs are correlated in turn to the experimental data.

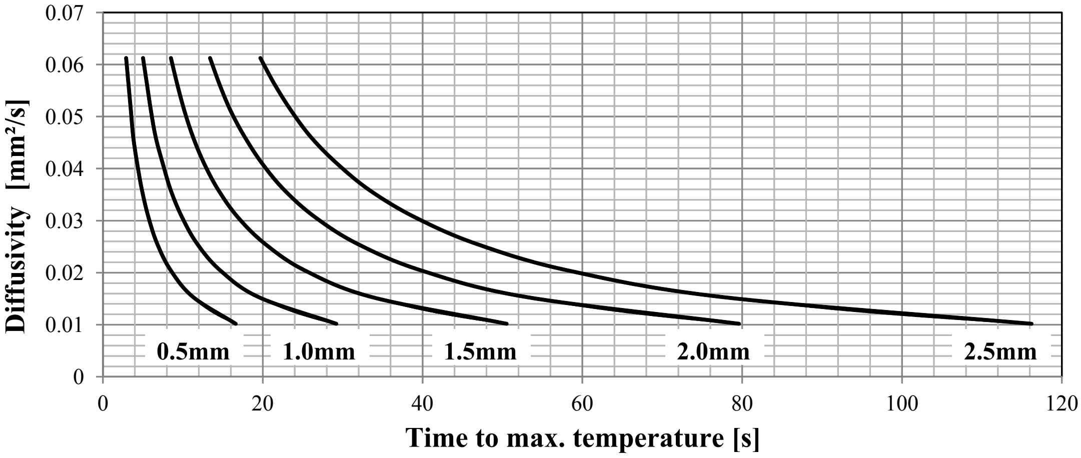

Figure 4.7 – Diffusivity calculation table for the conversion from time to maximum registered temperature to diffusivity. Each curve represents a specific temperature sensor depth.

4.4.3 Diffusivity and conductivity

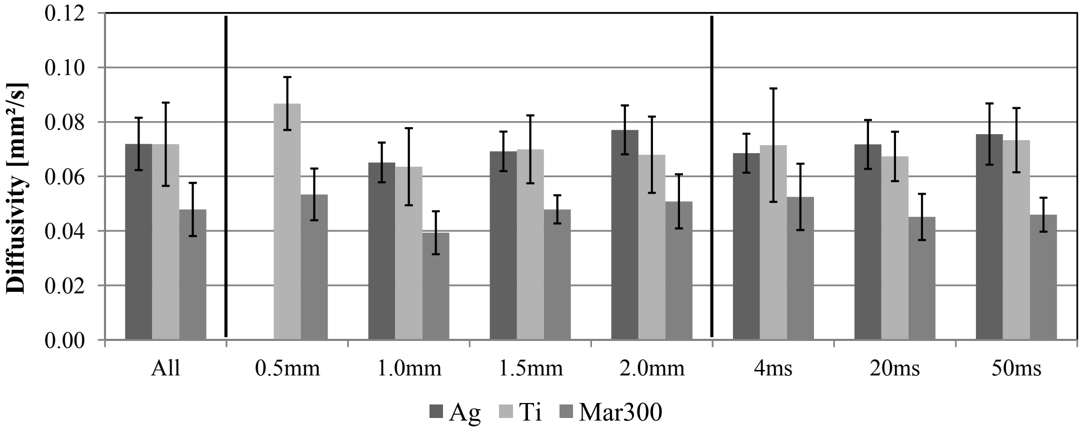

Figure 4.8 – Diffusivity results for the three tested powder types. The first group gives the average over all measurements. The second group gives a breakdown in terms of sensor depth and the third group in terms of beam exposure time. The error bars represent the standard deviation.

Figure 4.8 presents averaged diffusivity values for the three analyzed powder materials. For each of the measurement conditions the average diffusivity and the standard deviation are included. This allows an evaluation of which combination of conditions results in the least amount of spread. The optimal conditions appear to be with a sensor depth of 1.5 mm and a pulse length of 20 ms.

Table 4.1 summarizes the relevant material properties and the calculated effective thermal

Table 4.1 – Thermal and physical properties of the studied powders, and their measured diffusivities and conductivities. Material data is from Table 2.1 and Table 2.2. The given uncertainty interval for the diffusivity and conductivity is ±1 standard deviation.

	Silver	Titanium	Maraging 300 steel
Heat capacity [$\mathrm{J\,kg^{-1}\,K^{-1}}$]	234	528	540
Bulk thermal conductivity [$\mathrm{W\,m^{-1}\,K^{-1}}$]	419	17	19-21
Bulk density [$\mathrm{kg\,m^{-3}}$]	10.49×10^3	4.50×10^3	8.26×10^3
Powder density [$\mathrm{kg\,m^{-3}}$]	5.35×10^3	2.93×10^3	4.96×10^3
Powder volumetric heat capacity [$\mathrm{J\,m^{-3}\,K^{-1}}$]	1.25×10^6	1.54×10^6	2.68×10^6
Powder diffusivity [$\mathrm{m^2\,s^{-1}}$]	720 ± 100	720 ± 150	480 ± 100
Powder thermal conductivity [$\mathrm{W\,m^{-1}\,K^{-1}}$]	0.090 ± 0.012	0.111 ± 0.024	0.128 ± 0.026

diffusivity and conductivity. The thermal conductivities do not vary much, despite the large differences in the bulk thermal conductivity. Silver, with the highest bulk thermal conductivity has the lowest powder thermal conductivity. This could be explained through the low volumetric heat capacity (ρC_p) of silver powder. The numerical results compare well with those of Rombouts et al. (2005) [150] (0.11-0.19 $\mathrm{W\,m^{-1}\,K^{-1}}$) and Furumoto et al. (2007 [58] (0.11-0.18 $\mathrm{W\,m^{-1}\,K^{-1}}$) for comparably sized powders, in air and at room temperature. The dataset is unfortunately too small for an investigation of the influence of the powder density. The results do support the theories that the thermal conductivity is predominantly decided by the powder particle contact thermal resistance.

4.5 Conclusion

The combination of the measurement conditions and the processing method by correlation with simulated data provides results in line with published works. The conductivity for the powder materials is orders of magnitude lower than the bulk thermal conductivity, at least for the analyzed metals. Moreover, the powder thermal conductivity depends little on the bulk thermal conductivity.

The work demonstrates the viability of a thermal conductivity measurement system which is integrated in existing SLS/SLM equipment. A setup with a sufficiently low variability can be designed with few extra materials and used for a wide range of materials.

The measurements could potentially be expanded to studies of the influence of pressure and atmosphere. Due to the low depth of the thermocouple sensor in this design, the change in thermal conductivity during SLS/SLM processing can be characterized. Exploratory studies have been performed using the current setup, though no conclusive results are available as of writing.

5 Melt pool behavior

5.1 Introduction

5.1.1 Aim

This chapter applies process monitoring to the characterization of the melt pool, another of the key physical aspects of the SLM process. The melt pool is the liquid material formed under the laser beam. The melt pool size and shape are related in several ways to the process stability and quality.

The focus here is on the design considerations of the melt pool characterization setup and the procedures for obtaining valid data. The aim for this chapter is to extract a number of parameters which are characteristic for the melt pool. The solution should be able to accommodate for a range of materials and process conditions.

The next chapter focuses on applications of the melt pool characteristics, using three short case studies.

5.1.2 Methodology

The implemented system is based on a coaxial optical monitoring system (see Section 5.2 for terminology). The system is modular in order to accommodate various sensors and wavelength ranges.

The methodology is formed around the optimization of three steps:

- Data acquisition;
- Extraction of general melt pool characteristics;
- Calculation of the detailed melt pool temperature field.

Each step performs an analysis and optimization of the relevant parameters.

5.1.3 State of the art

An extensive state of the art on process monitoring for SLM is provided in Section 1.3.3. The designed setup is very similar to the most common method for on-line monitoring in SLM and laser welding.

The most prevalent characteristics in use are the peak and averaged intensity of the melt pool. For a more in depth analysis of the melt pool the contours can be calculated. Some works assign the material melt temperature to a reference intensity, based on the size of the melt pool as measured a-posteriori. This reference is then used to create a false-temperature image.

5.1.4 Novelty

While the basic method is very similar, the current work implements some acquisition and processing procedures to improve the quality of the retrieved data. The most notable are the hybrid timing methods for complex beam strategies and the rotation and translation invariant melt pool detection.

The calculation of the actual temperature field over the melt pool uses a unique combination of calibration and image processing techniques.

5.2 Background

The following paragraphs introduce some of the key concepts which apply to the contents of this chapter.

5.2.1 Process monitoring

Process monitoring has several application areas. A first application is *process characterization*. The gathered data can be used post-process in combination with other sample data to analyze the performance of the process parameters, aiding in process optimization. A second application is *process monitoring*. The data can be used to certify the quality of parts, demonstrating that they should be free of certain types of defects. This is of interest for medical and aeronautical industries.

The monitoring can also be used for real-time (on-line) detection of defects and process instabilities. This can lead to an automatic stop of the process or remove failed parts from the processing job. The result would be less time spent on parts which would not qualify and reduced material loss.

The last and most advanced application is real-time *process control*, where the collected data is interpreted and used to vary selected process parameters in real-time, in order to prevent or repair defects. From characterization over monitoring to control, the requirements of the system performance become more extensive.

5.2.2 Coaxial vision systems

A coaxial type of vision system is selected as the general basis of the monitoring setup. Vision systems detect some form of electromagnetic radiation. In laser processing methods, a coaxial vision system uses largely the same optical path as the laser beam. The radiation which is emitted or reflected from the processed spot returns through the same path as the incoming laser beam and is separated back out through the use of a selectively transparent mirror.

5.2.3 Sensors

The type of sensor has severe implications on the defect detection possibilities, as demonstrated further in this chapter. The sensors used in vision systems can be categorized in multiple ways. They can be separated by their wavelength sensitivities. Generally, sensors for the SLM process operate in the visible wavelength range (400-700 nm), the near-infrared range (NIR, 700-2000 nm) or in deeper infrared ranges (>2000 nm). A second form of classification is by spatial resolution. Typically two categories exist: spatially resolving sensors (1D or 2D cameras) or spatially integrating sensors (photodiodes). A third classification is by temporal response. For example, cameras typically integrate over a period of time, thermal sensors can have a settling time and photodiodes give an instantaneous snapshot measurement.

5.2.4 Data mapping

Data mapping is the spatial localization of measured or derived data quantities. In the case of monitoring systems for SLM, the sensor or image data is available as a function of time. If the position of the laser beam is also known as a function of time, the two data streams can be combined into a data series with the sensor data as a function of 2D or 3D position ((x,y) or (x,y,z)). This technique has already been applied to SLM by Craeghs et. al. (2011) [63]. The approach allows for easier visualization of structural defects and easier analysis.

5.3 Design and implementation

5.3.1 General assembly

The monitoring setups is integrated in the in-house SLM machine as detailed in Section2.2.

A schematic of the monitoring assembly is presented in Figure 5.1. The main reason for selecting a coaxial vision system is that the region of interest - the vicinity of the laser spot - remains centered in the field of view of the sensor. This allows for optimal use of the resolution and precision of a camera, assures a steady output for a photodiode and results in easier data

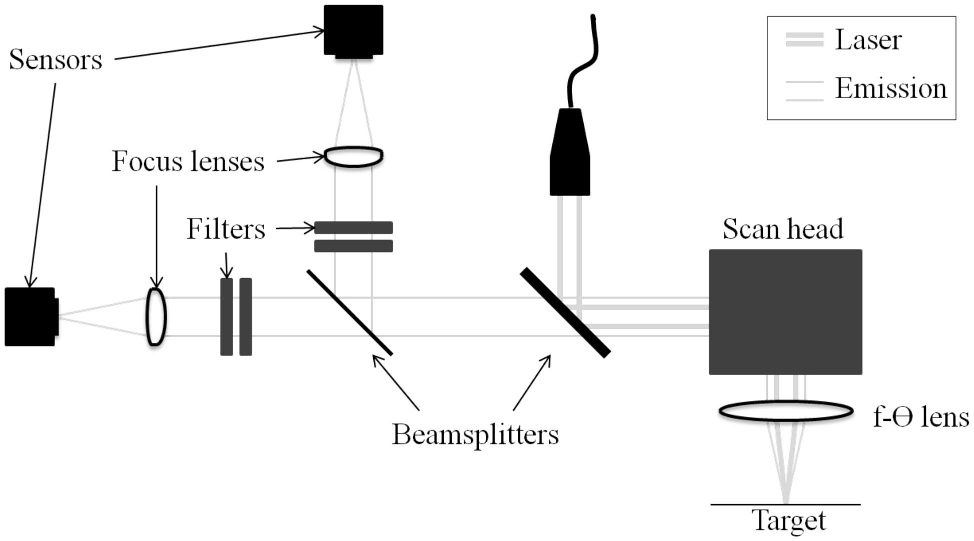

Figure 5.1 – Schema of the components of the general monitoring setup for two sensors. The filters and focusing optics are optional. The sensors can be CMOS cameras, photodiodes or a mixture.

treatment. It is also easier to shield the sensor equipment from influences of the processing chamber. Disadvantages of a coaxial setup are the smaller field of view - you don't see the complete processing area at once -, a more complicated setup and limitations in the studied wavelength bands.

The basis is a semi-transparent mirror (LaserOptics), which reflects or transmits light based on the radiation wavelength (also called dichroic mirror or beam-splitter). The dichroic mirror is used in reflection mode for the laser beam light. The cut-off wavelength is 1000 nm, the laser beam has a wavelength of 1070 nm. The mirror is mounted between the laser beam collimator and the scan head. Light emitted below and around the laser spot passes back through the scan head. The portion of the emitted radiation with a wavelength below 1000 nm is transmitted to the vision module.

The developed vision module is highly modular and can be equipped with one or two sensors, which can be cameras or photodiodes. Different configurations are selected, depending on the application. When two sensors are used, a second semi-transparent mirror separates the radiation. The second mirror can be a dichroic, to obtain light in two wavelength bands (Chroma T810lpxr-UF3) or broadband to reflect and transmit a certain portion of the intensity over all relevant wavelengths (Thorlabs BSW26R). Finally, focusing optics can be inserted between the filters and the sensors to obtain a range of magnifications for cameras or to tune the field of vision of photodiodes (Thorlabs AC254-200-B or Thorlabs AC254-300-B).

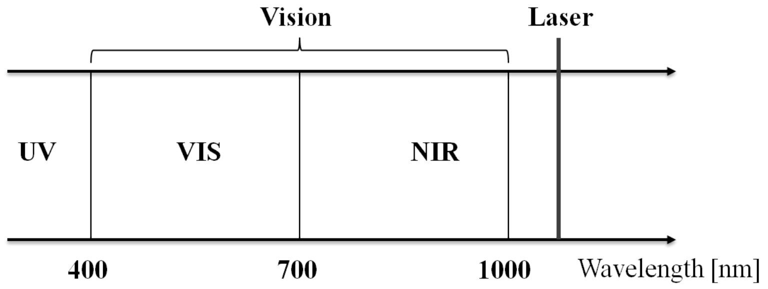

Figure 5.2 – Relevant radiation wavelength bands, with the position of the vision sensor ranges and the laser beam wavelength.

5.3.2 Wavelength band selection

The sampled radiation can be further adjusted by a series of optical filters. A wavelength specific (notch) filter is most often used to filter out any remaining back-reflection from the laser beam itself (Thorlabs NF1064). Long-pass and short-pass filters can be used to filter out infrared radiation and visible light, depending on the specific needs (Figure 5.2, Thorlabs FEL0700 and Thorlabs FES1000).

In standard conditions the wavelength band between 700 and 1000 nm is selected. The laser beam reflections at 1070 nm are filtered out as these do not give information on the size and shape of the melt pool, or the temperature distribution. The portion above the laser wavelength is what is used in many thermal imaging sensors, however the melting point of most SLM materials is higher, resulting in more intensity at lower wavelengths (<1000 nm).

The portion below 700 nm is often also filtered out, as emissions in this range are often associated with plasma formation above the melt pool or emissions from chemical reactions (oxidation).

5.3.3 Spatially integrating sensors

The setup can be equipped with a Thorlabs PDA36A photodiode with a measurement range between 350-1100 nm and a sensor area of 13 mm^2. The photodiode has a built-in amplifier with an amplification between 0 and 70 dB.

Usually no focusing optics are needed for this type of sensor, however focusing lenses can be used to tune the field of vision of the sensor. With the highest magnification optics (300 mm objective) the field of vision of the PDA36A detector is approximately 7.5 by 7.5 mm.

The value returned by the photodiode is a measure for the average intensity over the field of vision and correlates to the average image intensity of a 2D camera with equivalent field of vision.

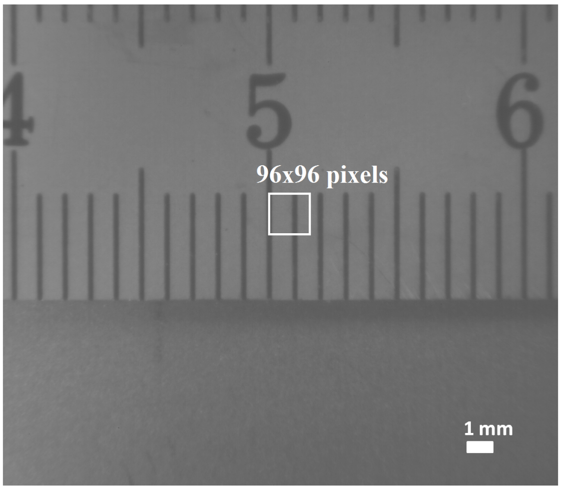

Figure 5.3 – Example calibration image for the MV1-D1312-240-CL8 camera with 300 mm objective. Demonstration of a typical 96x96 pixel region of interest.

5.3.4 Spatially resolving sensors

The vision setup can be configured with one or two CMOS cameras (PhotonFocus MV1-D1312-240-CL8), with a sensor which covers the wavelengths between 400 and 1000 nm. CMOS sensor technology was chosen over LCD technology because CMOS sensors are not sensitive to blooming. Blooming causes the intensity of nearby pixels to be affected by an overexposed pixel, which is a common occurrence for the high intensity variations in SLM. The selected camera model comes additionally with a configurable intensity compression technology which further increases the intensity range.

The pixel resolution can be varied by switching the focus lense. Three sets are available with effective resolutions of 48 µm (110 mm objective), 26 µm (200 mm objective) and 17 µm per pixel (300 mm objective). The image size is reduced to only include the vicinity of the melt pool. In most cases 96x96 pixels are sufficient, the equivalent of an area of 1.6 by 1.6 mm for the 300 mm objective (Figure 5.3). An increased resolution decreases the light intensity per pixel and might require an increase in exposure time for a sufficient signal to noise ratio.

5.4 General acquisition procedure

5.4.1 Camera calibration procedure

The monitoring system requires a number of calibration steps after an equipment change or even after process parameters changes.

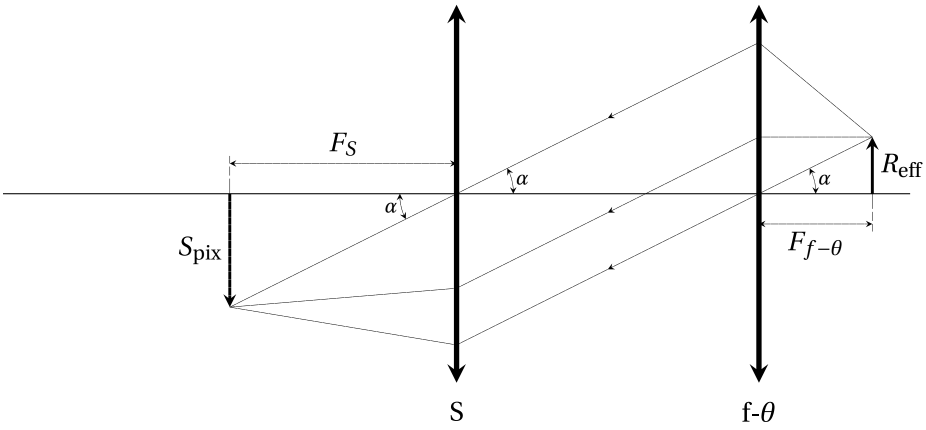

Figure 5.4 – Simplified optical chain for the calculation of the effective resolution.

Spatial calibration

When using the camera, the image resolution is measured experimentally by placing a calibrated object a the target plane. The object is sufficiently illuminated by an external light source and images are recorded. The effective resolution (R_{eff}) can also be theoretically derived from the $f-\theta$ lens focal length ($F_{f-\theta}$), the sensor focus lens focal length (F_s) and the physical sensor pixel size (S_{pix}). Figure 5.4 gives a simplified model of how the light propagates through the optical elements. Since the beamsplitter mirror and the low-pass mirror (see Figure 5.1) do not affect the magnification properties, only the lenses have to be considered.

Since it is in the focal plane, the reference object (size R_{eff}) emits light rays which will be parallel after the $f-\theta$ lens. Their angle with the lens axis is α:

$$\tan\alpha = \frac{R_{\text{eff}}}{F_{f-\theta}}. \tag{5.1}$$

The focusing lens now produces an image of the reference object in its focal plane. By definition of the reference object, this image has exactly the pixel size S_{pix}. On Figure 5.4 it can be seen that:

$$S_{\text{pix}} = F_S \tan\alpha. \tag{5.2}$$

It now follows from (5.1) and (5.2) that:

$$R_{\text{eff}} = \frac{F_{f-\theta}}{F_s} S_{\text{pix}}. \tag{5.3}$$

If the camera operates with a reduced image size - to gain in sample rate -, an image centering step is required. The camera orientation is first adapted manually, after which fine-tuning is possible by selection of the area of interest by software. Often one of the principal axes of the image is aligned with either one of the axes of the scan head coordinate system or with one of

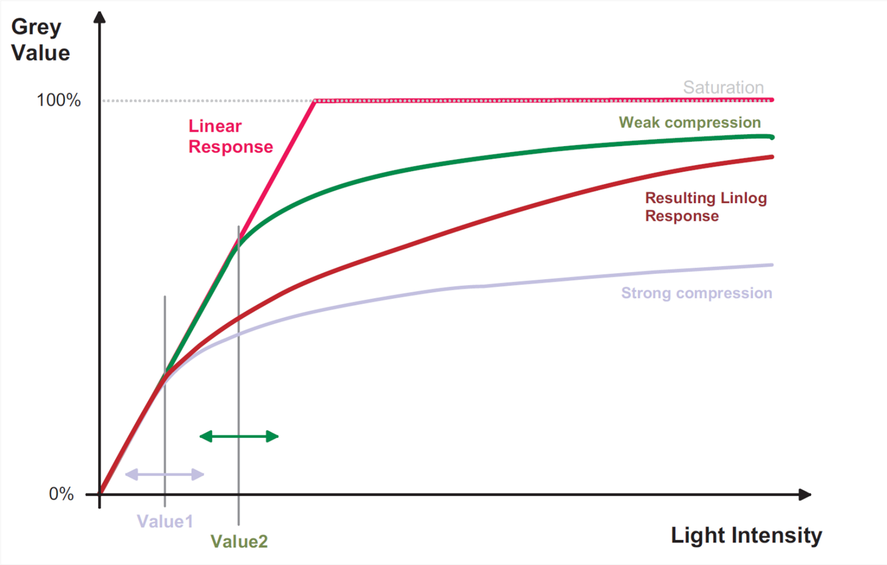

Figure 5.5 – Intensity compression capabilities of the PhotonFocus MV1 CMOS camera system.

the principal scan vectors (Figure 5.3).

Intensity calibration

The camera integrates the received light over a period of time, which is called the exposure time. The exposure time calibration is heavily process and material dependent, which means it often has to be optimized experimentally. The first step is to define the minimum exposure time in order to distinguish the low intensity features. After the first step, the intensity compression can be adjusted until almost no pixels are overexposed. The PhotonFocus cameras support intensity compressions with four adjustable parameters (Figure 5.5). Stronger compression results in a larger intensity range but lowers the resolution of the measurement.

For melt pool analysis the exposure time is between 10 and 200 µs, depending on the material and process conditions. The tuning process can be quite tedious due to high variance in received intensities.

5.4.2 Camera measurement procedure

Acquisition

An important part of the vision implementation in this work is the timing system for the cameras. Several image timing options are available (Figure 5.6).

For the monitoring of very short vectors, as is the case when building thin walls or lattice structures or when lasing at high speeds, the start of the camera exposure is synchronized with

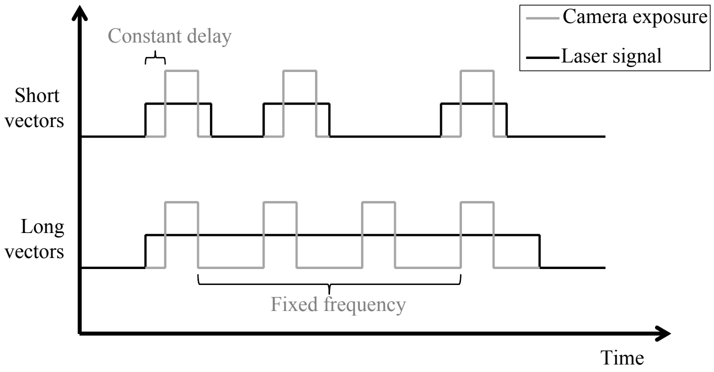

Figure 5.6 – Schematic representation of the image timing options for short (top curve) and long (bottom curve) scan vectors for optimal data collection.

the laser on signal. The synchronization has an experimentally measured delay between 50 and 100 µs. For a typical maximum exposure time of 200 µs, this allows efficient monitoring of 0.3 mm wide structures at a laser beam speed of $1\,\mathrm{m\,s^{-1}}$. The minimum delay can be increased if the application requires this, for example to take the image after an initial transient phase.

For longer scan vectors a fixed frequency sample rate is used in combination with the laser on signal as a gate signal. Images are only taken if the laser is active. Both systems can be combined, with the first image of a scan vector at a constant delay, and subsequent images at a fixed interval.

This approach results in increased consistency of the acquired images and increased flexibility. This is an important trait for the increasingly advanced and complex laser scan patterns (Section 1.3.2) and also for complex parts, where longer vectors are used for reinforced regions and short vectors for internal lattice structures (Section 1.2.5).

After the image acquisition is triggered through one of the available timing modes, the image data is corrected for background noise, fixed pattern noise and defective pixels by the camera hardware, before being send to buffer card in a PC. Custom software collects each image for further processing.

Processing

Camera images are processed in-real time or post-process. Several image and melt-pool characteristics are extracted to present the data in a more compact format, with a clear relation between the data and the process stability. The corrected image is first thresholded (binarized); all pixels with a low intensity value are discarded (typically < 80 – 120 out of 255). A 4-neighbor particle analysis algorithm extracts the largest homogeneous object, which is considered the melt pool. Any extra objects are detected and simply counted.

The threshold and neighbor selection algorithm is translation and rotation invariant. Despite the coaxial setup, the melt pool position is not entirely stable. The position and orientation depend on the speed and orientation of the beam movement. The algorithm compensates for these variations.

As for the melt pool detection, the characteristic algorithms have been selected based on robustness for asymmetric melt-pool shapes. Currently there are 5 extracted characteristics:

- **Average intensity** This is the average pixel intensity of all the pixels in the image or in a fixed subset of the image. The calculation is based on the image after correction but before binarization. The average intensity indicates how hot the material around the melt pool is and can indicate structural overheating or a bad contact with the previous layer (delamination, layer too thick).
- **Peak intensity** The highest intensity in the image. This characteristic is primarily used to calibrate camera parameters as the exposure time and the fine gain. An unusually low peak intensity can be a sign of insufficient energy input. This can be due to smoke occluding the laser beam or a powder deficit which causes energy loss through the previous layer.
- **Melt-pool size** The surface area of the melt pool in pixels or mm^2. This is the main melt-pool characteristic. Too small a melt pool indicates insufficient melting, too large a melt pool indicates overheating. It is also the principal stability metric.
- **Melt-pool aspect ratio** The aspect ratio of the melt pool is calculated as the ratio of the Feret diameter and the length of the equivalent ellipse minor axis (Figure 5.7). The Feret diameter is the longest distance between two points on the perimeter of the melt pool. The equivalent ellipse is an ellipse with the same area as the melt pool and a major axis with the same length as the Feret diameter. Typically an aspect ratio of over 3 indicates a risk of balling or loss of melt pool cohesion.
- **Total number of particles** Ideally only one particle (the melt pool) is present on the image. If multiple particles are found, this indicates spattering of material out of the melt pool or balling. The current algorithm does not distinguish between the two cases, even though it is technically possible to do so by analyzing the remaining particles size and position.

Reporting

The monitoring software automatically saves the camera and processing settings in a file along with the test data. The raw, processed and or thresholded images can be saved along with the extracted numerical data.

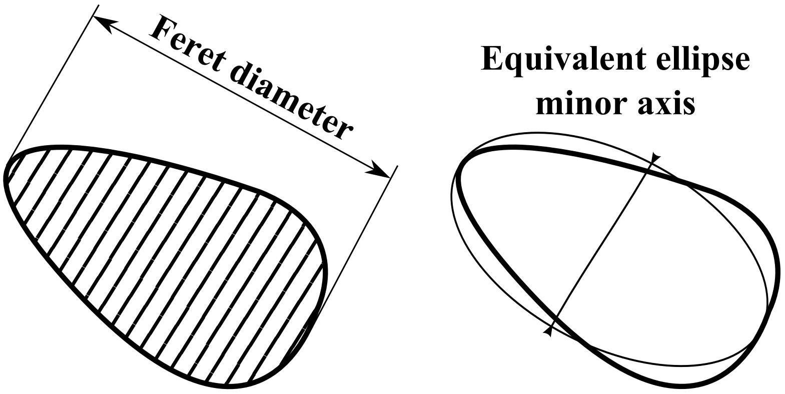

Figure 5.7 – Visualization of the concepts of Feret diameter, equivalent ellipse and the ellipse minor axis for the calculation of the aspect ratio of a melt pool.

5.4.3 Photodiode measurement procedure

Photodiode signal acquisition is performed at a fixed sample rate of typically 50-100 kHz. The voltage output (0-10 V) is converted to a 16-bit digital quantity by a data-acquisition card connected to a PC. Except for the amplification setting of the diode sensor, no additional pre-processing or signal conditioning is applied.

5.5 General temperature field procedure

Apart from the general characteristics of the melt pool, an effort is made to advance the calculation of the true temperature field over the melt pool. The temperature calculations are based on the concept of black body radiation and the ratio method for calculating the temperature for materials with unknown emissivity. The ratio method relies on two simultaneous light intensity measurements at two distinct wavelength bands.

The implemented setup uses two synchronized image sensors. The two images need to be superposed (correlated) and cleaned (median or Gaussian convolution filter). If intensity compression is used, the intensity of each image is linearized. The intensities of the two images are divided pixel per pixel to obtain the intensity ratio. This intensity ratio can be related to the black body spectrum. However, the optical elements do not transfer each wavelength equally.

The temperature calibration results principally in the measurement of the transfer function for each wavelength band. Two distinct calibration procedures are explained. The calibrations result in a correction on the theoretical intensity ratio.

5.5.1 Image acquisition

A two-camera system is used in combination with a wavelength-selective mirror (Chroma 810lpxr-UF3) which splits the normal vision wavelength range in two bands (A: 810-1000 nm and B: 700-810 nm). The images are acquired using a hardware synchronized timer and fixed exposure time (0.1-0.2 ms).

5.5.2 Spatial correlation

Since mechanical spatial alignment of the two camera sensors is near impossible, a software algorithm shifts (translates) one of the two images so that the two images are superposed. Two methods are developed: one uses positional data from the melt pool characterization algorithm (melt-pool-center method) and the other uses image cross-correlation (cross-correlation method).

The melt-pool-center method uses the melt-pool detection algorithm and calculates the center of gravity of the melt pool by uniform weights for each pixel in the melt pool, for both camera images. The difference in the positions of the melt pool center of gravity is used as the translation vector.

The cross-correlation method uses an implementation of normalized image cross-correlation in LabVIEW. This standard technique [153] is applied in the Fourier domain. Conceptually, the method works as follows: the gray levels in both images essentially correspond to two discrete functions attributing an integer value to each pixel (in $2D$). These functions can be extended into two complex valued functions g_1 and g_2, defined over $\mathbb{R}^2$. If the second image is simply obtained by shifting the first, g_2 is obtained by mapping a translation onto g_1:

$$g_2(\mathbf{x}) = T_{\mathbf{h}_0} g_1(\mathbf{x}), \mathbf{x} \in \mathbb{R}^2, \tag{5.4}$$

where $T_{\mathbf{h}_0}$ is the translation operator:

$$v = T_{\mathbf{h}_0} u \Longrightarrow v(\mathbf{x}) = u(\mathbf{x} - \mathbf{h}_0), \mathbf{x} \in \mathbb{R}^2. \tag{5.5}$$

The challenge of the correlation method is how to determine as accurately as possible the translation vector $\mathbf{h_0} \in \mathbb{R}^2$. The solution is to compute the Fourier transforms $\hat{g}_1$ and $\hat{g}_2$ of g_1 and g_2, respectively, and to consider the inverse Fourier transform w of the ratio $\hat{g}_1/\hat{g}_2$:

$$w(\mathbf{h}) = \int_{\mathbb{R}^2} e^{i\mathbf{h}\cdot\mathbf{k}} \frac{\hat{g}_1(\mathbf{k})}{\hat{g}_2(\mathbf{k})} \mathrm{d}^2\mathbf{k}. \tag{5.6}$$

The theory says that the module $|w|$ of w shows a very sharp maximum at $\mathbf{h} = \mathbf{h_0}$ where $\mathbf{h_0}$ is the translation vector between the two images (Equation 5.4). This property enables a precise identification of $\mathbf{h_0}$.

Both correlation methods can not compensate for differences in rotation. Software algorithms exist, but degrade the quality of the image. In the current setup, the rotation alignment can only be done manually. No scaling or perspective compensation is needed for this optical setup.

For regular melt pools or calibration images the two correlation methods give equivalent results (Figure 5.8). The cross-correlation method has more difficulties in unstable processing conditions (bright spots), while the melt-pool-center of gravity method can be inaccurate for small melt pools due to inaccuracies in the melt pool detection.

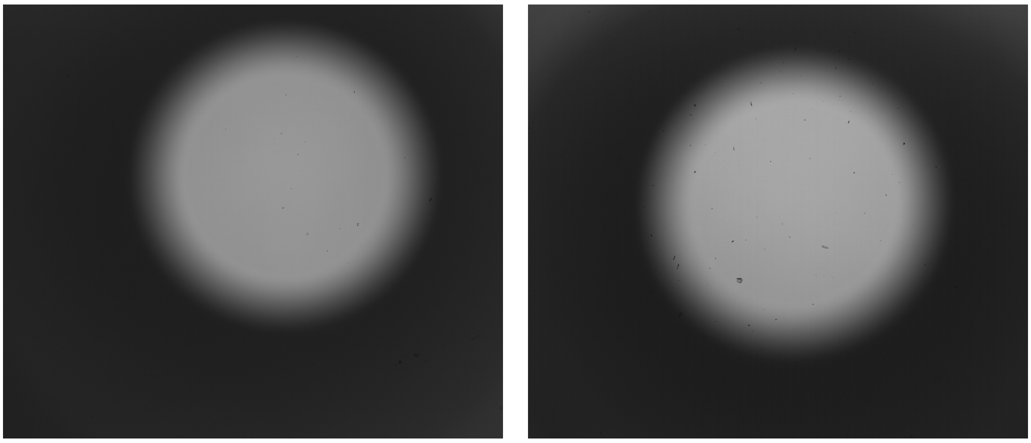

(a) Camera A (b) Camera B

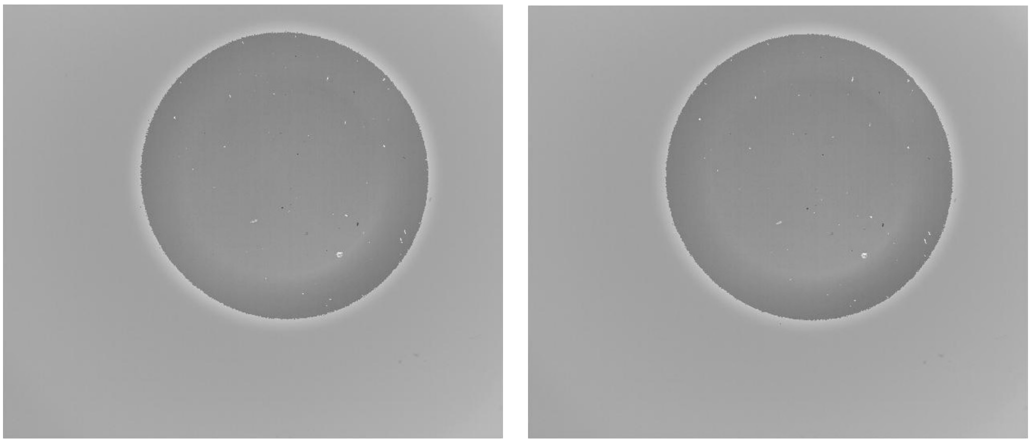

(c) Cross-correlation (d) Center of gravity

Figure 5.8 – Example of 2 images for calibration procedure A and comparison between two spatial correlation techniques: cross-correlation through the frequency domain (c) and melt-pool center of gravity (d). The comparison image is the result of the subtraction of the two images after correlation.

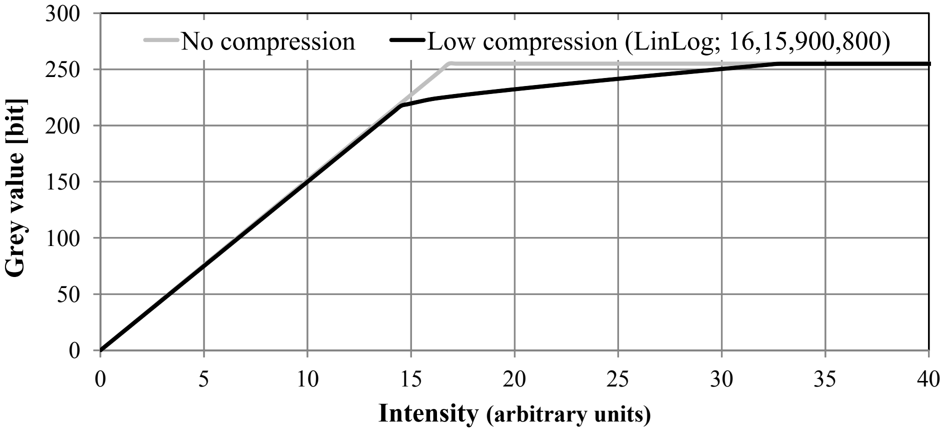

Figure 5.9 – Resulting camera sensor return value (gray value) as a function of intensity for two camera exposure modes: no compression and low compression.

5.5.3 Intensity linearization

The intensity linearization involves two steps. The first step is a shift of the intensity levels to compensate for the mean background intensity level.

The second step is the linearization of the gray levels in case intensity compression has been used. The intensity-gray level relation can be derived from the specifications provided by the manufacturer. Figure 5.9 shows the intensity profiles for the two most common modes: the linear mode with no compression and the LinLog mode with pseudo-logarithmic compression which roughly doubles the intensity range for the low-compression mode.

In the case of the low-compression LinLog mode, the link between the pixel gray value and the collected intensity is derived to be:

$$g(I) = \begin{cases} c_0 I, \text{ if } I < I_1 \\ c_0 I_1 + (1-t_1)c_0(I-I_1) + \alpha \log(1+t_1(I-I_1)), \text{ if } I_1 < I < I_2 \\ c_0 I_1 + (1-t_1)c_0(I_2-I_1) + (1-(t_1+t_2))c_0(I-I_1) + \\ \qquad \alpha \log(1+t_1(I-I_1))(1+t_2(I-I_2)), \text{ if } I_2 < I < I_3 \\ 255, \text{ otherwise.} \end{cases} \tag{5.7}$$

In this relation, c_0 is an arbitrary constant since only the relative intensity will be considered (Section 5.5.5). The two parameters t_1 and t_2 can be specified in the camera settings. The three limit intensities I_1, I_2, I_3 as well as the coefficient α are then determined from the manufacturer LinLog documentation.

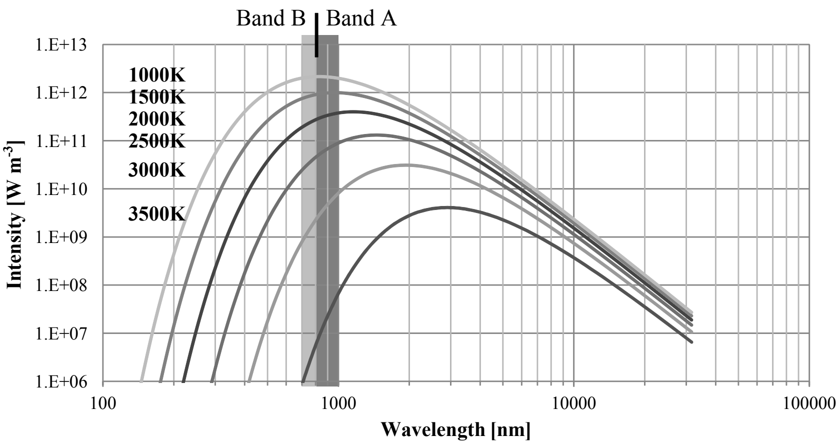

Figure 5.10 – Emission spectrum for a black body at various temperatures. The two sensor wavelength bands are indicated.

5.5.4 Radiation spectra

A section $\mathrm{d}\sigma$ on the surface of a body at temperature T emits a radiative power $\mathrm{d}P$ in the wavelength band between λ and $\lambda + \mathrm{d}\lambda$:

$$\mathrm{d}P = E(\lambda, T)\mathrm{d}\sigma\mathrm{d}\lambda, \tag{5.8}$$

where E represents the intensity spectrum which depends on the wavelength λ and on the temperature T. According to Planck's theory [154], E is expressed as:

$$E(\lambda, T) = \epsilon(\lambda, T)\frac{2hc_0^2}{\lambda^5\left(e^{\frac{hc_0}{k\lambda T}} - 1\right)}[\mathrm{W\,m^{-2}m^{-1}}], \tag{5.9}$$

where h is Planck's constant (6.626×10^{-34} Js), k is Boltzmann's constant ($1.380 \times 10^{-23}\ \mathrm{J\,K^{-1}}$) and c_0 the speed of light in vacuum ($2.99792 \times 10^8\ \mathrm{m\,s^{-1}}$). The positive factor $\epsilon(\lambda, T)$ is the emissivity of the material. The emissivity is wavelength and temperature dependent in most situations, but its value is always less than 1. If it equals 1, then the material is said to be a black-body. Figure 5.10 illustrates the intensity spectrum of a black-body for the relevant range of temperatures. The wavelength bands corresponding to the equipped sensors are indicated on this diagram as well.

Consider now a sensor S of surface $\mathrm{d}S$ (e.g. a single pixel), associated to an optical chain so that it looks exclusively at the surface $\mathrm{d}\sigma$. If the radiative power received by S is represented as $\mathrm{d}p$, then for each wavelength band $(\lambda, \lambda + \mathrm{d}\lambda)$, the sensor actually collects a power proportional to the emitted one (Equation 5.8). The proportionality constant K' depends on the wavelength and on the combination of the sensor and optical chain. It also takes the pixel sensitivity and its exposure time into account as well as the view angle of the surface $\mathrm{d}\sigma$ and the losses through the optical elements (lenses, mirrors, filters). K' represents a function $K' = K'(S, \lambda)$. If

$(\lambda_{\text{min}}, \lambda_{\text{max}})$ is the wavelength band to which S is sensitive, the final conclusion is:

$$\mathrm{d}p = \int_{\lambda_{\text{min}}}^{\lambda_{\text{max}}} K'(S,\lambda) E(\lambda, T) \mathrm{d}\sigma \mathrm{d}\lambda. \tag{5.10}$$

The differential quantity $\mathrm{d}p$ can be correlated to the sensor size $\mathrm{d}S$ to obtain the total collected intensity, expressed in $\mathrm{W\,mm^{-2}}$. It is a function of the sensor characteristics and of the temperature: $I = I(S,T)$. To highlight this dependency, after dividing Equation 5.10 by $\mathrm{d}S$ and replacement of $E(\lambda, T)$ by its value (Equation 5.9) the result is:

$$I(S,T) = \int_{\lambda_{\text{min}}}^{\lambda_{\text{max}}} K(S,\lambda)\epsilon(\lambda,T) \frac{2hc_0^2}{\lambda^5\left(e^{\frac{hc_0}{k\lambda T}} - 1\right)} \mathrm{d}\lambda. \tag{5.11}$$

In this relation the new factor $K(S,\lambda)$ is called the transfer function for sensor S. It is obtained as the product of the previous factor $K'(S,\lambda)$ and of the magnification coefficient $\mathrm{d}S/\mathrm{d}\sigma$, which obviously depends on the optical chain as K' already does.

5.5.5 Ratio method

If the temperature dependency of the emissivity $\epsilon(\lambda, T)$ of the material is known, the measure of $I(S,T)$ leads to an equation to be solved for the temperature T. For most materials, especially for powders, this information is not available or difficult to obtain. The ratio method was developed to solve the problem of the unknown emissivity. Two sensors S_A and S_B are used to observe the same region $\mathrm{d}\sigma$ of the material surface over two different wavelength bands $(\lambda^A_{\text{min}}, \lambda^A_{\text{max}})$ and $(\lambda^B_{\text{min}}, \lambda^B_{\text{max}})$. The assumption is that the wavelength bands are sufficiently narrow and close together so that the emissivity is constant over each band for a fixed temperature: $\epsilon(\lambda, T) \simeq \epsilon(T)$. The same condition applies to the two transfer functions $K(S_A,\lambda) \simeq K(S_A)$ and $K(S_B,\lambda) \simeq K(S_B)$. By dividing the two intensities, the emissivity factor cancels out and the proportionality constants combine in a ratio $C(S_A, S_B) = \frac{K(S_A)}{K(S_B)}$, referred to as the calibration constant.

The calibration depends on the two sensors' characteristics and on their respective optical chains. The conclusion is now that the intensity ratio:

$$R(S_A, S_B, T) = \frac{I(S_A, T)}{I(S_B, T)}, \tag{5.12}$$

only deviates from its so called normalized value:

$$R_{\text{norm}}(S_A, S_B, T) = \frac{\int_{\lambda^A_{\text{min}}}^{\lambda^A_{\text{max}}} \frac{\mathrm{d}\lambda}{\lambda^5\left(e^{\frac{hc_0}{k\lambda T}} - 1\right)}}{\int_{\lambda^B_{\text{min}}}^{\lambda^B_{\text{max}}} \frac{\mathrm{d}\lambda}{\lambda^5\left(e^{\frac{hc_0}{k\lambda T}} - 1\right)}}, \tag{5.13}$$

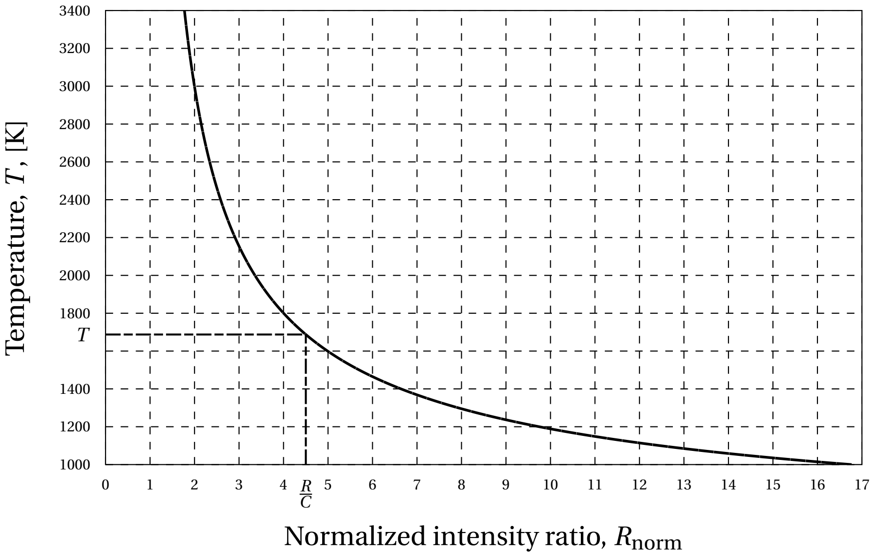

Figure 5.11 – Normalized intensity ratio for wavelength bands of 810-1000 nm (A) and 700-810 nm (B). Illustration of the method to identify T when the intensity ratio R and the calibration constant C are known.

by the calibration constant:

$$R(S_A, S_B, T) = C(S_A, S_B) R_{\text{norm}}(S_A, S_B, T). \tag{5.14}$$

If the value of the intensity ratio is measured and if the calibration constant is known, then Equation 5.14 can be solved for the temperature.

Figure 5.11 represents the relationship between the temperature and the normalized ratio in the case of the two camera sensors S_A and S_B, with wavelength bands between 810 and 1000 nm (S_A) and 700 and 810 nm (S_B). It also illustrates graphically the procedure for solving Equation 5.14. The figure clearly shows a one to one correspondence. Observe as well that the practical range of ratios is limited by the image intensity quantization levels. The rough limit would be between 2 and 6 for 8 bit cameras.

Even with a good knowledge of the cameras' settings and the optical chains, an a priori computation of the calibration constant $C(S_A, S_B)$ seems difficult. The next sections propose two different experimental procedures (calibration methods) for the indirect calculation of $C(S_A, S_B)$, after alignment of the cameras and optical chains.

An important assumption is that all the pixels in a given camera have the same settings (sensitivity, exposure time, wavelength band) and are part of the same optical chain. This means that the calibration constant $C(S_A, S_B)$ has a given value as soon as S_A and S_B are pixels in camera A and camera B, respectively, looking to the same physical point.

5.6 Temperature calibration A - Calibrated light source

5.6.1 Setup description

This calibration strategy uses a light source with a known intensity distribution. The method is tested with an Olympus KL1500 light source with a black body spectrum and an adjustable color temperature between 2600 K and 3300 K. The light source is placed near the normal processing plane, at the position of the laser beam.

This particular light source does not cover the entire relevant temperature range. Unfortunately, alternative sources with lower color temperatures did not achieve sufficient intensity for good images. Therefore some extrapolation is required.

5.6.2 Ratio calculation

The procedure consists of the acquisition of images for a number of color temperatures (Figure 5.8). The images are acquired and processed by the aforementioned procedure. The results is a map of the intensity ratio (Equation 5.12), corresponding to a selected temperature. The next step is to compare it to the map of the normalized ratio R_{norm} for the same temperature (Equation 5.13 and Figure 5.11).

The ratio between the two maps results in the calibration constant (Equation 5.14):

$$C(S_A, S_B) = \frac{R(S_A, S_B, T)}{R_{\text{norm}}(S_A, S_B, T)}.$$

The results are illustrated on Figure 5.13 for twelve temperatures ranging from 2650 K to 3500 K. Statistics are calculated for six images per temperature to obtain an average value of the calibration constant as well as the standard deviation over each image series.

Figure 5.13 seems to show a slight monotone increasing dependency of the calibration constant with respect to temperature. This fact can not be explained by our model. A possible reason is that the basic assumption on which the theory is based is not completely fulfilled and that the emissivity ϵ and the transfer function K do depend on the wavelength.

5.6.3 Temperature field

The value of the calibration constant deduced from Figure 5.13 can now be used to calculate the full temperature distribution over the actual melt pool, as measured during SLM processing. For each pixel the intensity ratio is calculated and converted into a temperature. An example of a calculated temperature field is given in Figure 5.14. The melt pool was captured during the scanning of a layer of Maraging steel powder on a stainless steel substrate.

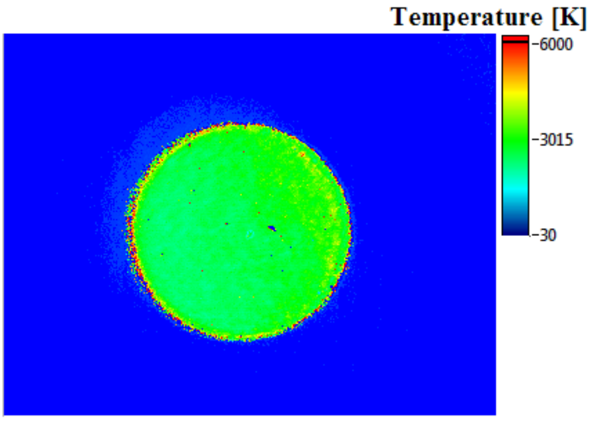

Figure 5.12 – Temperature field of a calibration image at 3000 K. This type of image is used to check the calibration homogeneity for a given temperature/intensity ratio combination.

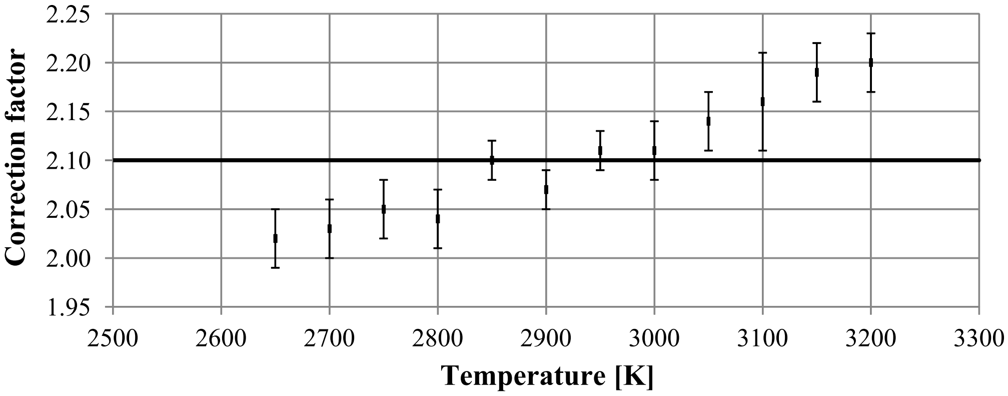

Figure 5.13 – Calibration constant as a function of temperature for a typical calibration. The error bars represent the standard deviation over 6 images. The average value of the calibration constant is 2.10.

5.7 Temperature calibration B - Melt pool size

5.7.1 Setup description

This calibration method relies on the correlation of the melt pool size on the acquired images with a physical melt pool size. At the edge of the physical melt pool, the temperature is equal to the melting point of the material.

The conditions for applying this method are:

- A stable, well defined melt pool should be created;
- The material needs to have a small temperature interval between solidus and liquidus;
- A range of materials is necessary to perform a full calibration.

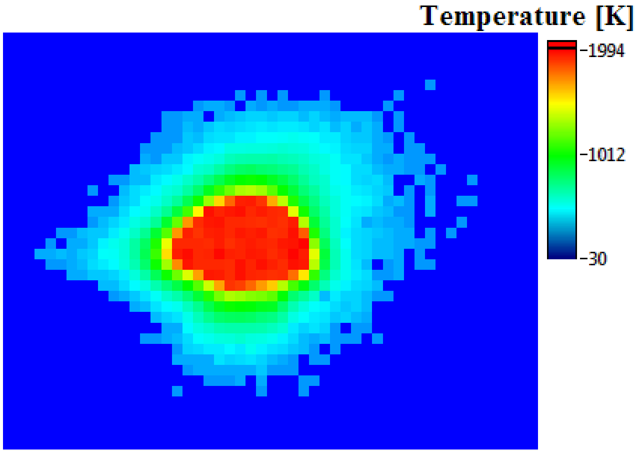

Figure 5.14 – Temperature field of a melt pool. Calibration according to the calibrated lamp method. The resolution is 25 µm per pixel.

Table 5.1 – Suitable materials for melt pool calibrations. Sourced from MatWeb.

Material	Solidus [°C]	Liquidus [°C]	Melt interval [°C]
Aluminum 1100	643	657	14
Brass	885	900	15
Silver	961	961	0
Copper C10100	1083	1083	0
Stainless steel 301	1400	1421	21
Titanium	1650	1670	20

The procedure is tested on one material: 316L stainless steel. Other materials which could be considered for a complete calibration curve are listed in Table 5.1. These are either pure metals or near-eutectic alloys.

5.7.2 Data-acquisition

The implemented procedure uses the SLM laser beam to melt a single, straight line in a solid metal substrate. The laser beam operates at a power between 27 and 75 W in steps of 5 W. The displacement speed is fixed at 80 mm s^{-1}.

The image acquisition is performed with an exposure time of 1 ms and in low compression mode. The images have a resolution of 17 µm per pixel.

5.7.3 Melt pool measurement

The real melt pool is measured orthogonal to the displacement vector, from a-posteriori optical microscope images (Figure 5.15). The width of the actual molten portion is measured. The heat affected zone with discoloration but no large surface topology changes is not taken into account.

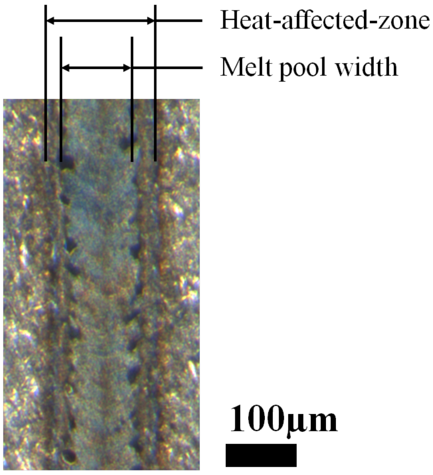

Figure 5.15 – Measurement of the real melt pool width.

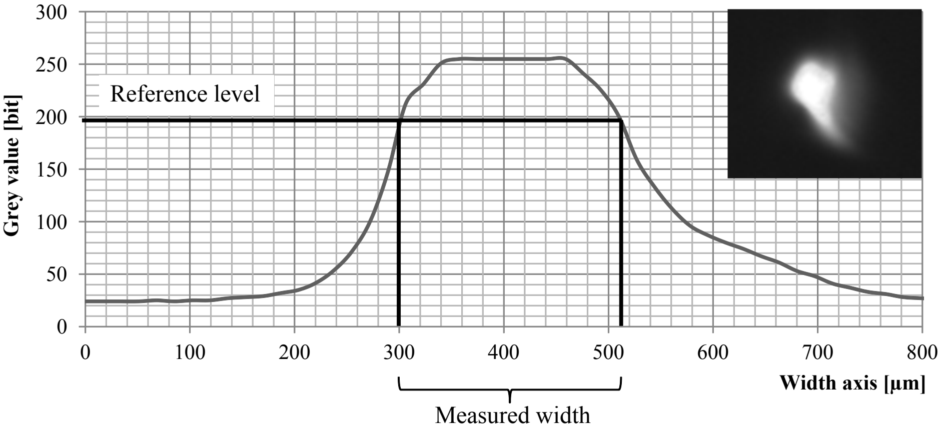

Figure 5.16 – Correlation of the real melt pool width to the image intensity line profile.

The melt pool image is bisected at the point of maximum melt pool width. The intensity line profile is generated and the measured real melt pool width is fitted onto the line profile

(Figure 5.16). The grey levels corresponding to the melt point T_{melt} of the tested material are obtained for both cameras.

After background level subtraction and linearization (Equation 5.7), the intensities $I(S_A, T_{\text{melt}})$ and $I(S_B, T_{\text{melt}})$ are deduced and the intensity ratio (Equation 5.12) is computed. Correlation with the normalized value (Equation 5.13) results in the calibration constant $C(S_A, S_B)$.

Measurements for additional materials with a range of melting points will yield a calibration curve with the temperature as a function of the intensity ratio. The rest of the procedure continuous as described in Section 5.6.2 and Section 5.6.3.

5.8 Additional considerations

Several influences can disturb the monitoring process. There are those which affect the emission of the melt pool radiation:

- Shielding of radiation due to smoke or suspended powder particles in the atmosphere;
- Emission of parasitic radiation through chemical reactions (oxidation).

The use of the camera means the melt pool emissions are integrated over the exposure time. The emission fluctuations introduce some error on any calculations, especially the temperature field. All calculations using the gray value of the image are subject to quantization error due to the limited number of discrete values available. Even dust particles on optical elements or malfunctioning pixels will give local erroneous values.

Furthermore, the various algorithms introduce errors as well. The spatial correlation algorithm can fail in the case of low intensity or a chaotic melt pool behavior. The errors can be mitigated by smoothing the image using a convolution filter, however this reduces the resolution of the resulting data.

Note that the description of the calibrations is mainly to demonstrate the procedures. It has not yet been possible to verify whether the calibration holds up in the interval between 1000 K and 2000 K.

5.9 Conclusion

The chapter presented a detailed technique for obtaining melt pool characteristics for SLM. It builds upon existing setups and introduces some new techniques to improve the data quality and quantity. The melt pool characteristics are useful process indicators for real-time process monitoring.

The procedure for calculating the temperature field around the melt pool can give useful data for comparison with and validation of numerical models and simulations. However, the calibration is non-trivial, both in terms of equipment and effort. The measurements are easily disturbed, so control of the process environment is of vital importance. The base methods are set, but more data is needed to validate the technique.

6 Applications of melt pool characterization

6.1 Introduction

Three short case studies are presented to illustrate the various applications of melt pool characterization as introduced in Chapter 5. The detailed camera vision results are applied to the study of how defects develop and what their characteristic features are on the acquired images. Spatial data mapping is used in identifying problem regions during the build process. High-sample rate measurements help process optimization by comparing process conditions in terms of stability.

6.2 Defect development

6.2.1 Case description

This case study uses the developed laser-camera synchronization (Section 5.4.2) to acquire an image of the melt pool at fixed positions for each scan vector. The synchronization allows to consistently acquire images even for short vectors and high scan speeds.

The case study attempts the production of a thin wall, 0.6 mm wide, scanned with a discontinuous, inclined pattern with alternating vectors. The nominal speed of the laser beam is 2400-3500 $\mathrm{mm\,s^{-1}}$. Each scan vector consists of a lasing part where the laser melts material (0.3-0.6 ms) and a deceleration, reverse direction, acceleration part where the laser beam is off (0.6 ms). The material is Maraging 300 steel powder in 50 µm layers on a stainless steel substrate, beam power is 250 W vector spacing is 50 µm. The process takes place in the in-house SLM machine under Argon atmosphere (Section 2.2).

The camera has a flexible acquisition rate, with a maximum of approximately 2 kHz. The synchronization delay is 50-100 µs and the camera exposure time is 100 µs. The pixel resolution is 26 µm.

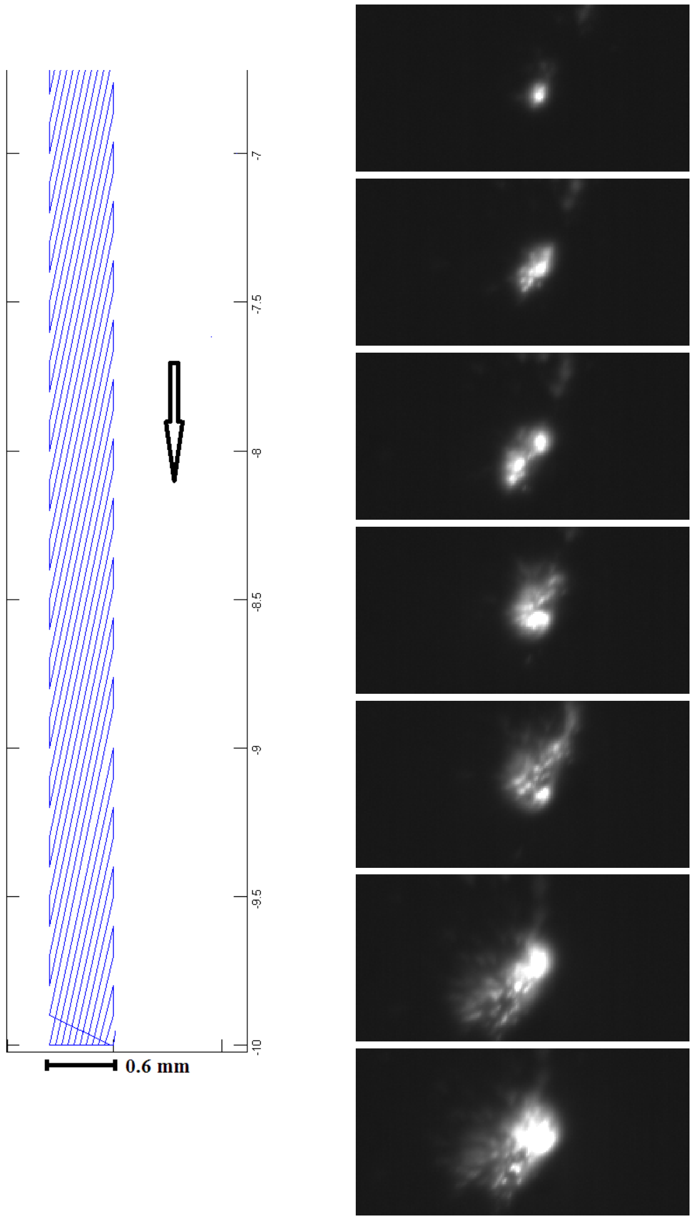

Normal operation, well defined melt pool with no artefacts.

Start of instability, elongation of the melt pool and ejection of molten material.

Desintegration of the melt pool, possible balling as a result.

Major overheating of the melt pool, previously scanned tracks remain hot.

Cycle of overheating and melt pool decomposition, overheated area increases.

Escalation of melt pool overheating, damage to the sample over a wide area.

Continuous instability.

Figure 6.1 – Illustration of the development and escalation of a defect while scanning thin walls (one image in two, interval ±1.5 – 2 ms, total time 9-12 ms).

6.2.2 Results and discussion

The results presented in Figure 6.1 are an extract of the 10th layer. The images demonstrate the way in which a melt pool can become unstable. The melt pool goes through different stages with each their characteristic features. The camera images allow to distinguish between different types of instabilities. The melt pool characteristics which are extracted from the images (Section 5.4.2) are based on this kind of analysis.

The series of images also demonstrates the time-scale at which these defects occur and develop. The camera does not continuously register the melt pool emissions and there is time-averaging of the emission over the sensor exposure time. Short time-scale instabilities can go undetected, however, these are rarely critical. Critical defects, which require the process to be stopped, could be detected during the escalation phase (3-5 ms).

This case study acquires the images in a relatively controlled environment, the scanning of thin walls does not lead to significant powder bed heating and does not cause much powder blow-out. During the production of bulk samples, there are often more factors disturbing the measurement, making the assessment of instabilities more difficult. This will become more apparent in the second case study.

6.3 Melt pool stability maps

6.3.1 Case description

This case study applies the technique of spatial data mapping (Section 5.2.4) to the extracted melt pool characteristics from a camera image (Section 5.4.2). The purpose is to visualize the data in a way which makes it easier to assess the process homogeneity and easier to detect which parts of the scan strategy might give problems. In order to demonstrate the effect of various process conditions, a benchmark of 10 scan patterns is assembled.

Data mapping requires the registration of the laser position along with the melt pool data. In this case an indirect approach is applied. Timing data is stored together with the melt pool data. The laser beam movement is simulated numerically, by a model which emulates the functioning of the beam controller. The beam movement data is then correlated to the melt pool data. The developed software can perform these calculations in real time.

The benchmark patterns are introduced in Figure 6.2. The actual scan strategy uses the same configuration of the patterns. Each pattern is a separate sample of 6 by 6 mm. The state of the art contains more information on common scan patterns (Section 1.3.2).

The melt pool data is obtained by scanning a solid 304 steel substrate (250 W, 765 $\mathrm{mm\,s^{-1}}$ beam speed, 50 μm vector spacing) and acquiring images at a frequency of 500 fps with an exposure time of 100 μs and low LinLog compression. The standard processing parameters are applied (Section 5.4.2).

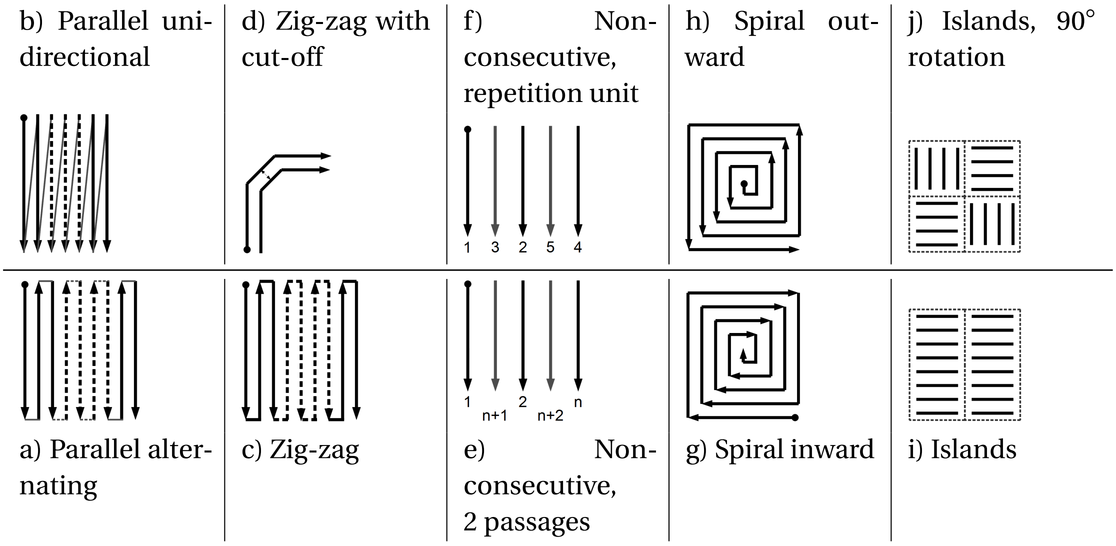

b) Parallel unidirectional

d) Zig-zag with cut-off

f) Non-consecutive, repetition unit

h) Spiral outward

j) Islands, 90° rotation

a) Parallel alternating

c) Zig-zag

e) Non-consecutive, 2 passages

g) Spiral inward

i) Islands

Figure 6.2 – Benchmark consisting of 10 different scan patterns.

6.3.2 Results and discussion

Figure 6.3, Figure 6.4 and Figure 6.5 show the maps for three of the measured melt pool characteristics: the melt pool surface area, the average image intensity and the peak image intensity.

Visual analysis of makes it clear that for these specific parameters, samples ‘a’ and ‘b’ consistently had a larger than average melt pool. The average image intensity agrees reasonable well with the melt pool size. This indicates that an increase in overall image intensity generally goes together with in increase in melt pool size. The same can be observed for the peak image intensity. Since photodiodes measure a total intensity over an area around the melt pool, the result for a photodiode sensor will contain a mix of the melt pool size and the intensity of the melt pool emission.

The assessment of the severity of instabilities remains difficult, as apparently large differences in melt pool parameters, even over large zones, do not necessarily have a visible effect on the physical sample. Effective use of these maps requires a good understanding of the conditions and values which result in critical defects.

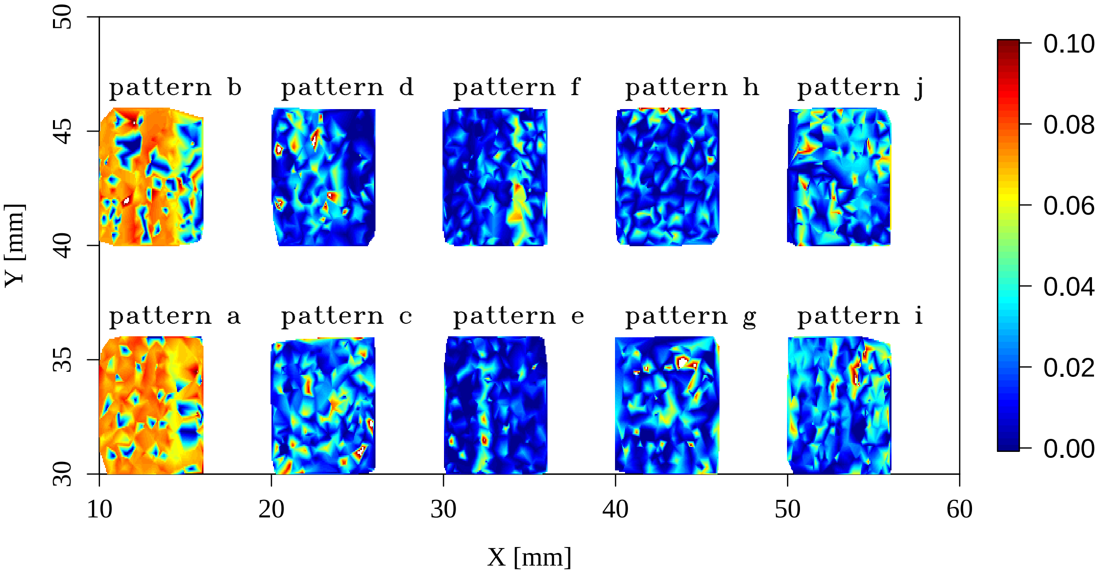

Figure 6.3 – Mapping of the melt pool size (in mm^2) on a benchmark of 10 scan patterns as detailed in Figure 6.2.

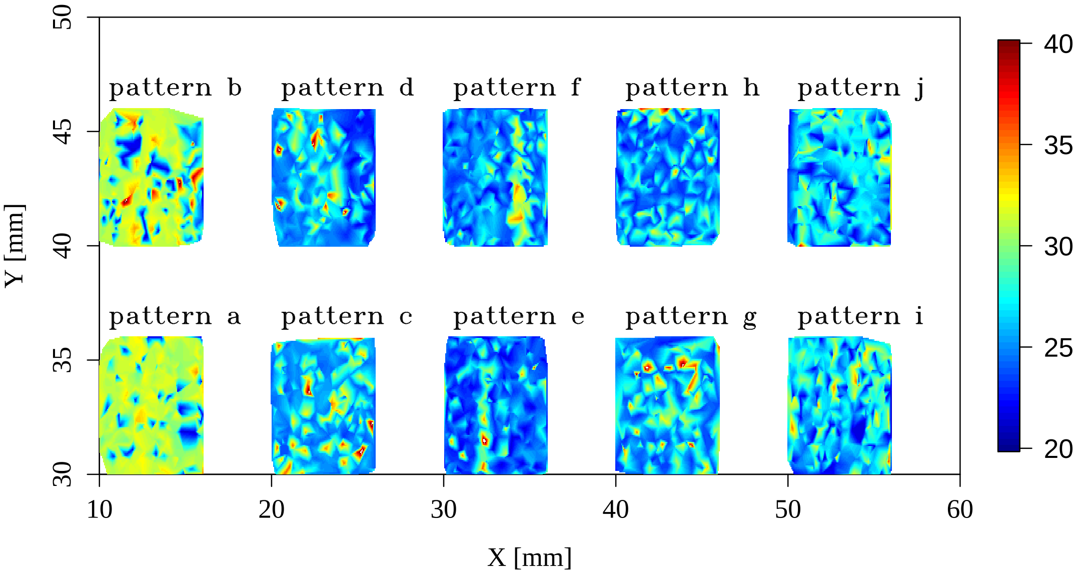

Figure 6.4 – Mapping of the number of the average image intensity on a benchmark of 10 scan patterns as detailed in Figure 6.2.

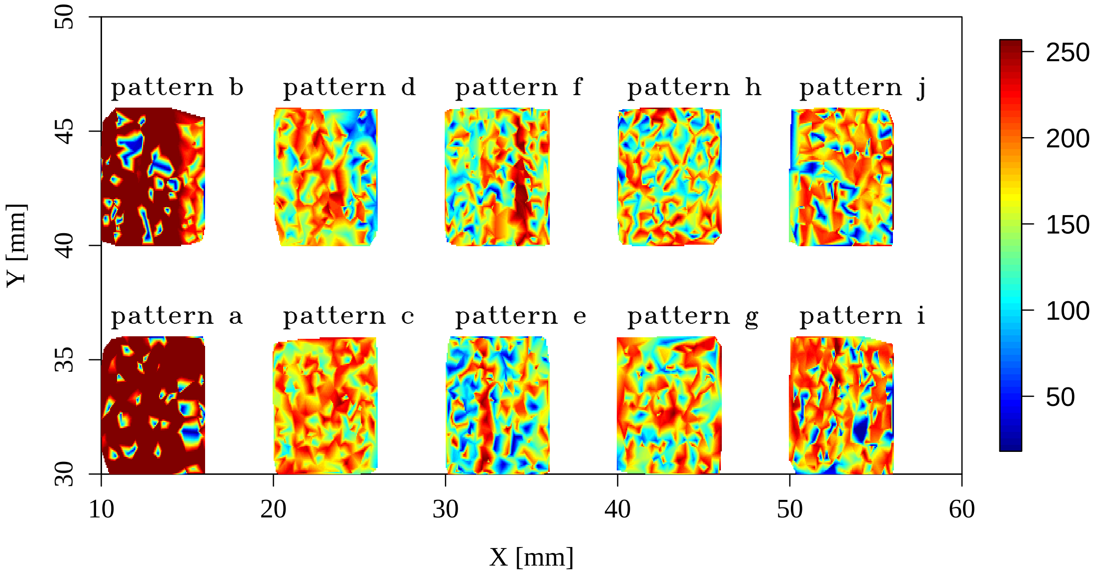

Figure 6.5 – Mapping of image peak intensity on a benchmark of 10 scan patterns as detailed in Figure 6.2.

6.4 Scan pattern comparison

6.4.1 Case description

This case study retakes the scan pattern benchmark from the previous section (Figure 6.2). This time the signal from a high-speed (100 kHz) photodiode is studied. The focus is on the use of the detailed temporal information to better evaluate the differences in the scan patterns.

The process conditions for the test are the same as in Section 6.3.1, except for this case study a 100 µm layer of the reference AlSi10Mg powder is applied (Section 2.3) and the process takes place in Argon atmosphere.

6.4.2 Results and discussion

Figure 6.6 represents a discontinuous, alternating pattern. The signal varies substantially over each cycle, with a higher intensity at the start of a cycle. The cycles themselves are very regular, and the interruption in the series near the end of the sample resulted in a noticeable change in surface texture. The source of the irregularity is unknown; one common cause is a powder bed irregularity.

Figure 6.7, which represents a discontinuous, uni-directional pattern does not have the same

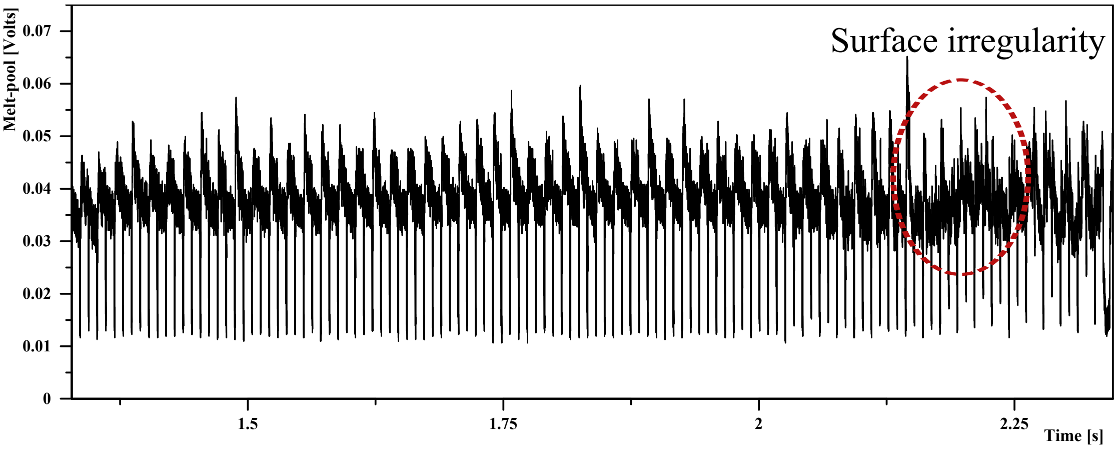

Figure 6.6 – Photodiode output for a parallel alternating pattern (Figure 6.2a).

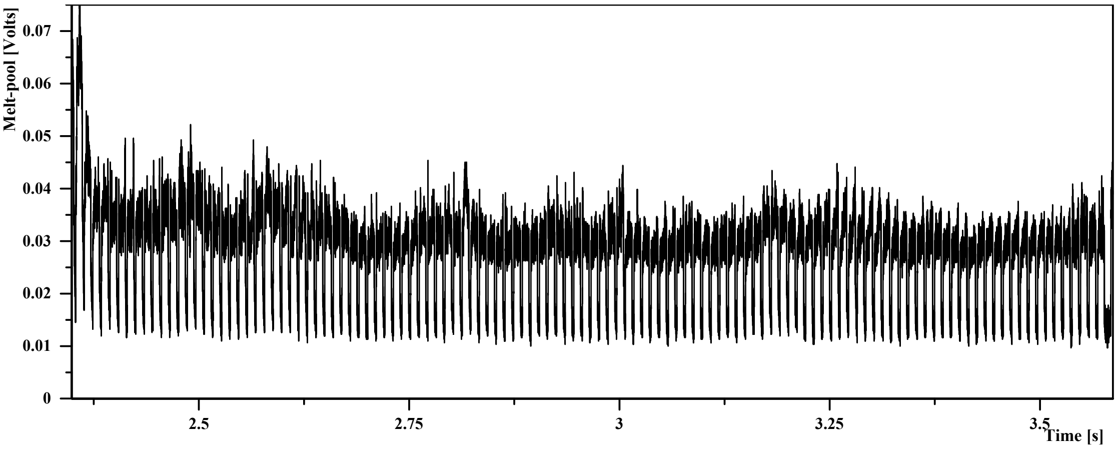

Figure 6.7 – Photodiode output for a parallel uni-directional pattern (Figure 6.2b).

repetitive behavior. The increased intensity at the start is a fairly common occurrence as small variations in the powder bed greatly influence the start of a laser scan. This type of pattern has the tendency to leave a surplus of liquid at the end of the scan vector, resulting in a raised ridge which can hinder the powder layering process.

Figure 6.8 is the signal from a continuous zig-zag pattern. This pattern is somewhat similar to the discontinuous alternating pattern, with cyclic melt pool behavior. The highest intensity is measured near the vector extremities.

Figure 6.9 shows a special type of pattern. The whole sample is scanned twice, but at double vector spacing. This results in a first passage where the melt pool is surrounded by powder, resulting in more unstable behavior. In the second passage the melt pool is mostly surrounded by (partially) consolidated material, which results in a more stable signal. The increased stability is due to the high thermal conductivity of the solid material, which diffuses short

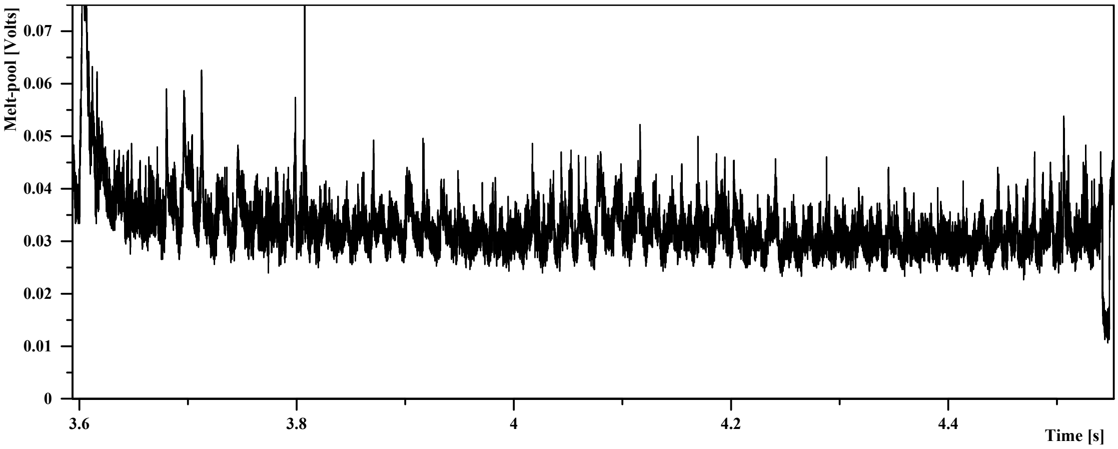

Figure 6.8 – Photodiode output for a zig-zag pattern (Figure 6.2c).

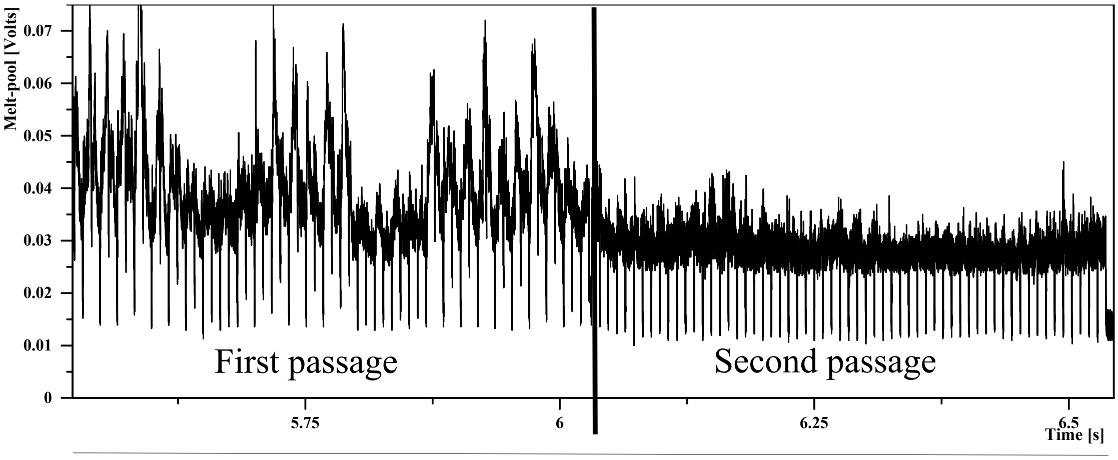

Figure 6.9 – Photodiode output for a non-sequential pattern with two passages (Figure 6.2e).

variations in temperature. This pattern has been shown to be able to reduce internal porosity and improve the surface finish [110].

Figure 6.10 represents a non-consecutive scan pattern, where the vectors are not scanned in the logical order. Instead, each cycle one vector is skipped, after which the skipped vector is scanned. This results in vectors which are alternately surrounded by mainly powder and mainly consolidated material. The effect is a relatively large variation in signal intensity from vector to vector. The benefit of this ‘skipping’ pattern is that overheated melt pools cannot propagate for very long as the pattern is continuously interrupted.

Figure 6.11 shows the signal development for a continuous, inwards spiraling pattern. The signal is relatively stable for most of the sample, except for the innermost part where energy rapidly accumulates. The effect is somewhat tempered though, due to the large amount of

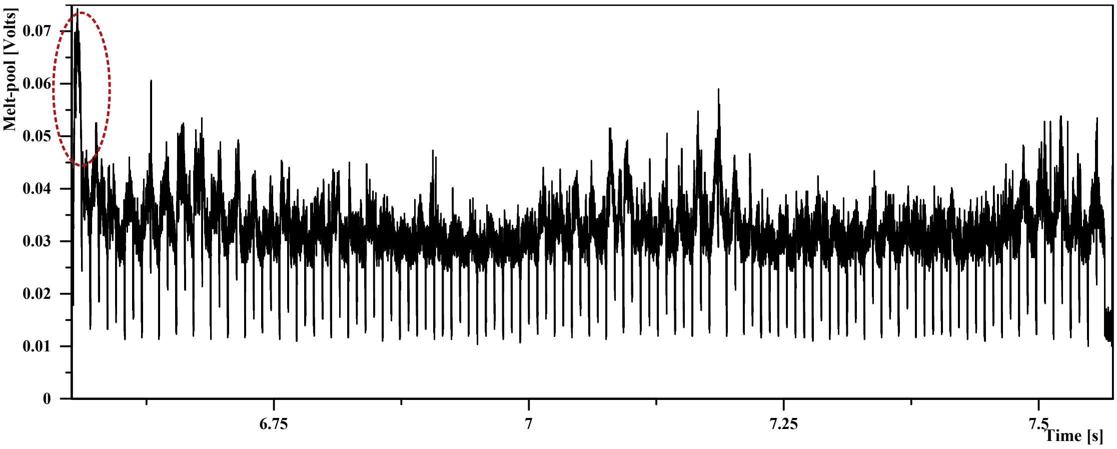

Figure 6.10 – Photodiode output for a non-sequential pattern with a repetition unit of 2 vector spacings (Figure 6.2f).

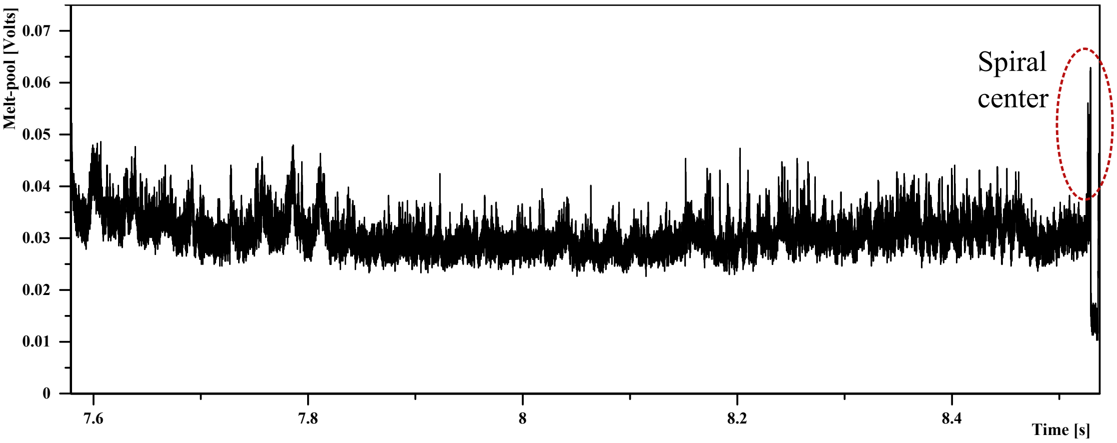

Figure 6.11 – Photodiode output for an inwards spiraling pattern (Figure 6.2g).

highly conductive solid material surrounding the center.

Figure 6.12 shows a continuous, outwards spiraling pattern. The signal starts high and is unstable for a long time before it stabilizes. At the start of the pattern a lot of energy is absorbed by the center at the center of the spiral. In contrast to the inwards spiral, the center is now surrounded by low thermally conductive powder.

While spiral patterns are uncommon in practice, they demonstrate what can happen at fine features in 3D objects. It is advised to start with the blunt side of the feature, to use the consolidated material as a thermal sink to avoid overheating at the fine feature.

The average signal intensity level does not vary much between the scan patterns. Though all present some unique features.

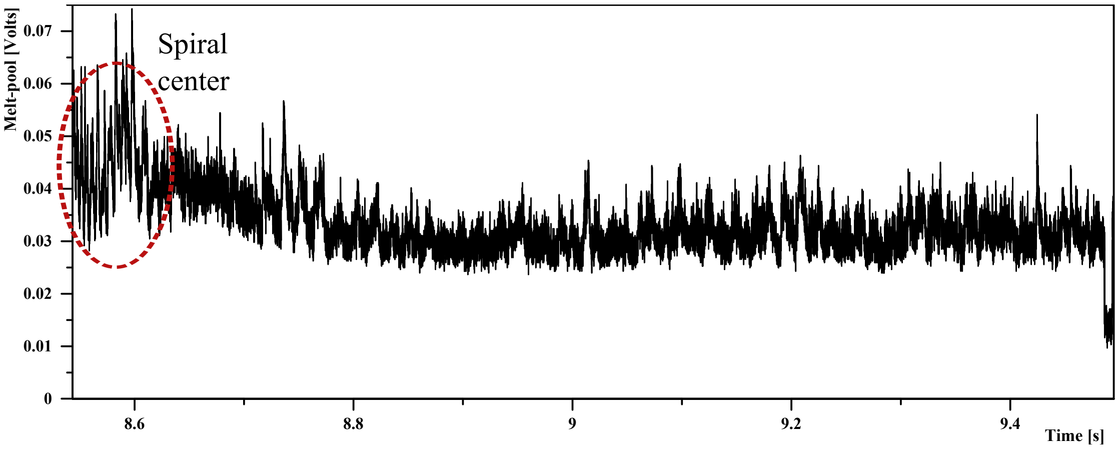

Figure 6.12 – Photodiode output for an outwards spiraling pattern (Figure 6.2h).

6.5 Conclusion

The three case studies present practical applications which are made possible by the integrated vision system. The applications cover a wide range from fundamental defect analysis, assistance in pre-process optimizations and quality control in production environments. The case studies also highlight the strengths and uses of the different sensors.

Spatially resolving cameras give more detailed information on the melt pool geometry, the melt pool surroundings and melt pool desintegration. This information allows to distinguish between possible types of defects in real-time. Spatial mapping of the data further helps in identifying problem regions or in the detection of larger defects as delamination of layers.

High-speed photodiodes on the other hand are more suited to general stability analysis using the high acquisition frequency and detailed intensity measurement. The photodiodes also give precise information on the evolution of the melt pool along individual scan vectors and help in identifying problematic regions in the scan pattern.

The analysis of the data and especially the prediction of the impact remain difficult and the limit values for the extracted characteristics will have to be established experimentally for each case, until predictive numerical models are available.

Conclusion

The presented work tries to aid the SLM process by improving the understanding of the physical mechanisms at play. It shows how focused experimental studies can help and are even required for the further development of SLM.

The state of the art is written for stakeholders in the SLM process, to develop and increase awareness of the multitude of efforts and solutions for improving the SLM process. It also serves as a bridge to show how the study of the fundamental process aspects ties into several solution strategies: material selection, parameter optimization, defect reductions and improved predictive models for structural optimization of additive designs.

Three of the fundamental physical aspects are experimentally studied: the interaction of laser beam light with the material to be processed, the transport of heat within the material and the behavior of the molten material. The SLM process conditions for these aspects have some unique characteristics. The radiation material interaction is characterized by very high energy intensities, the beam is small compared to the individual powder particles and the state transition from porous solid to liquid happens on very small timescales (~ 0.1 ms). The small melt pool translates at high speeds ($\sim 1000\,\mathrm{mm\,s^{-1}}$), while the thermal diffusion in the surrounding powder material is very low.

The three techniques demonstrated in this thesis are designed for operation at the specific conditions of the SLM process. Validation of the results is carried out by comparison with available data where possible. Assessments of the precision of the techniques also receives considerable attention. If the test conditions are well controlled the variability is shown to be acceptable. Possible effects which can disturb the measurements are pointed out.

The performed absorptance experiments show that the classical material properties are not a good indicator of the materials' performance for SLM. The results indicate that during the absorption event the effective absorptance varies greatly with the state of the material, but is always higher compared to reported values for the same material in the bulk, cleaned and polished state. The measurements show that especially materials with a low base absorption, like silver and aluminum, have a significantly higher (5-10 times) effective absorptance.

Even the absorption by molten or re-solidified material can vary considerably depending on the processing environment. Solid Maraging steel samples with an oxidation layer have a

35% higher absorptance compared to samples processed in a protective atmosphere. These are important considerations during material selection and during optimization of process parameters such as the process atmosphere, scan vector overlap and scan speed.

The outcome of the thermal diffusion measurements are results for the thermal conductivity for Maraging steel powder ($0.128\,\mathrm{W\,m^{-1}\,K^{-1}}$), silver powder ($0.090\,\mathrm{W\,m^{-1}\,K^{-1}}$) and titanium ($0.111\,\mathrm{W\,m^{-1}\,K^{-1}}$). The results confirm those reported elsewhere and show that the powder thermal conductivity can not easily be related to the bulk conductivity. The results also validate the measurement technique, which uses an unconventional ring-shaped laser beam and combines it with simplified finite-element simulations to correlate the measured data to the material properties.

The thermal conductivity experiments measure the thermal evolution around the melt pool. The thermal history will affect the material state and change related properties as the absorptance and mechanical cohesion. The material change around the melt pool thus affects the conditions for the next scan vector. The thermal conductivity also plays an important role in the energy balance, as demonstrated by melt pool overheating at regions surrounded by powder: first vectors, overhangs and sharp features. A correct simulation of the temperature flow and balance can help optimize the processing conditions for these situations.

The study of the melt pool behavior gives detailed data on the process stability and is of vital importance for fine-tuning process parameters and beam patterns. Significant research into monitoring systems is already available for a variety of purposes. This work introduces a series of acquisition and image processing techniques to extract relevant information and present it in an understandable way, through mapping of the data.

The relationship between the melt pool characteristics and several types of defects is elaborated. The detection capabilities are not perfect, powder blowout and smoke formation affect the measurement and no detector can detect every anomaly. The monitoring techniques are nonetheless already helpful in a number of situations, such as general overheating, delamination and instability escalations. Early detection of critical defects can save process time and prevent equipment damage.

It has to be stressed that the investigated aspects, while important, do not cover the whole process. Aspects that are not included are the 3D melt pool dynamics, the cooling of the melt, the subsequent micro-structure formation and the final mechanical properties.

Even for the studied aspects, the work represents an evolutionary step. The techniques build on those developed by previous researchers. The implementations are robust and can be used for further investigations. The SLM process involves many parameters and there is still plenty of opportunity for research. Suggestions are a more thorough investigation of the role of the process atmosphere, the measurement of the thermal diffusion at the moment the melt pool comes into contact with the previous layer and an improvement of the interpretation of measured melt pool characteristics.

Bibliography

1. Levy, G. N., Schindel, R. & Kruth, J.-P. Rapid Manufacturing and Rapid Tooling With Layer Manufacturing (Lm) Technologies, State of the Art and Future Perspectives. *CIRP Ann. - Manuf. Technol.* **52,** 589–609 (2003).
2. The Economist. *Three-dimensional printing may help entrench the worlds engineering giants* Berlin, 2014. <http://www.economist.com/news/business/21601528-three-dimensional-printing-may-help-entrench-worlds-engineering-giants-heavy-metal>.
3. Cunningham, J. *Airbus puts its faith in 3D printed parts* 2014. <http://www.materials-for-engineering.co.uk/engineering-materials-news/airbus-puts-its-faith-in-3d-printed-parts/62218/> (visited on 06/17/2015).
4. Weaver, T. J., Thomas, J. A., Atre, S. V. & German, R. M. Time compression-rapid steel tooling for an ever-changing world. *Mater. Des.* **21,** 409–415 (2000).
5. Autodesk. *Autodesk Inventor* 2015. <http://www.autodesk.com/products/inventor/overview>.
6. Adobe. *Adobe Photoshop CC* 2015. <https://blogs.adobe.com/creativecloud/3d-printing-a-beginners-guide-for-creatives/>.
7. Kruth, J.-P., Vandenbroucke, B., Vaerenbergh, J. & Mercelis, P. Benchmarking of different SLS/SLM processes as rapid manufacturing techniques. *Int. Conf. Polym. Mould. Innov.* 1–7 (2005).
8. Manfredi, D. *et al.* Additive Manufacturing of Al Alloys and Aluminium Matrix Composites (AMCs). *Light Met. Alloy. Appl.* 3–34 (2014).
9. Kruth, J.-P., Mercelis, P., Froyen, L. & Rombouts, M. Binding Mechanisms in Selective Laser Sintering and Selective Laser Melting. *Solid Free. Fabr. Proc.* **15** (2004).
10. Gu, D. D., Meiners, W., Wissenbach, K. & Poprawe, R. Laser additive manufacturing of metallic components: materials, processes and mechanisms. *Int. Mater. Rev.* **57,** 133–164 (2012).
11. Levy, G. N. The role and future of the Laser technology in the Additive Manufacturing environment. *Phys. Procedia* **5,** 65–80 (2010).

12. Lyons, B. Additive Manufacturing in Aerospace Examples and Research Outlook. *Front. Eng.* **42,** 13–19 (2012).

13. Polivnikova, T. *Study and Modelling of the Melt Pool Dynamics during Selective Laser Sintering and Melting* PhD thesis (Ecole Polytechnique Fédérale de Lausanne, 2015).

14. Bayle, F. & Doubenskaia, M. Selective Laser Melting process monitoring with high speed infra-red camera and pyrometer. *Proc. SPIE* **6985,** 698505 (2008).

15. Castillo, L. *Study about the rapid manufacturing of complex parts of stainless steel and titanium* tech. rep. (2005).

16. Buchbinder, D., Schleifenbaum, H., Heidrich, S., Meiners, W. & Bültmann, J. High power Selective Laser Melting (HP SLM) of aluminum parts. *Phys. Procedia* **12,** 271–278 (2011).

17. Schleifenbaum, H., Meiners, W., Wissenbach, K. & Hinke, C. High power selective laser melting; a new approach for individualized series production. *ICALEO* (2010).

18. Birnbaum, A. J., Beuth, J. L. & Sears, J. W. Scaling Effects in Laser-Based Additive Manufacturing Processes. *Solid Free. Fabr. Symp.* 151–162 (2004).

19. Fallahi Sichani, E., De Keuster, J., Kruth, J.-P. & Duflou, J. R. Monitoring of CO2 Laser Cutting of Thick Steel Plates by Means of a NIR Camera Based System. *Key Eng. Mater.* **410-411,** 207–216 (2009).

20. Yang, J., Ouyang, H., Xu, C. & Wang, Y. Top surface quality research for direct metal laser fabrication. *Rapid Prototyp. J.* **18,** 4–15 (2012).

21. Abe, F., Osakada, K., Shiomi, M., Uematsu, K. & Matsumoto, M. The manufacturing of hard tools from metallic powders by selective laser melting. *J. Mater. Process. Technol.* **111,** 210–213 (2001).

22. Dadbakhsh, S. & Hao, L. Effect of Layer Thickness in Selective Laser Melting on Microstructure of Al / 5 wt .% Fe 2 O 3 Powder Consolidated Parts. *Powder Technol.* **231,** 112–121 (2014).

23. Verma, A. & Rai, R. Energy Efficient Modeling and Optimization of Additive Manufacturing Processes. *Proc. Solid Free. Fabr. Symp.* 231–241 (2013).

24. Beuth, J. & Klingbeil, N. The role of process variables in laser-based direct metal solid freeform fabrication. *J. Mater. Sci.* **53,** 36–39 (2001).

25. Gahler, A., Heinrich, J. G. & Günster, J. Direct laser sintering of Al2O3-SiO2 dental ceramic components by layer-wise slurry deposition. *J. Am. Ceram. Soc.* **89,** 3076–3080 (2006).

26. Kruth, J.-P., Wang, X., Laoui, T. & Froyen, L. Lasers and materials in selective laser sintering. *Assem. Autom.* **23,** 357–371 (2003).

27. Wijers, J. L. C. Nach CO2 nun Nd: YAG Laser für Blechbearbeitung. *Tech. Rundschau* **112** (1996).

28. Gusarov, A. V. Radiation transfer in metallic-powder beds during laser forming. *Quantum Electron.* **40,** 451–459 (2010).

29. Zhou, J., Zhang, Y. & Chen, J. K. Numerical simulation of laser irradiation to a randomly packed bimodal powder bed. *Int. J. Heat Mass Transf.* **52,** 3137–3146 (2009).

30. Yasa, E., Deckers, J., Craeghs, T., Badrossamay, M. & Kruth, J.-P. Investigation on occurrence of elevated edges in selective laser melting. *Solid Free. Fabr. Symp.* 180–192 (2009).

31. Liu, K. & Tovar, A. An efficient 3D topology optimization code written in Matlab. *Struct. Multidiscip. Optim.* 1175–1196 (2014).

32. Smith, C., Todd, I. & Gilbert, M. Utilizing additive manufacturing techniques to fabricate weight optimized components designed using structural optimization methods. *Solid Free. Fabr. Symp.* 879–894 (2013).

33. Amin Yavari, S., Ahmadi, S. M., Wauthle, R., Pouran, B., Schrooten, J., Weinans, H. & Zadpoor, A. A. Relationship between unit cell type and porosity and the fatigue behavior of selective laser melted meta-biomaterials. *J. Mech. Behav. Biomed. Mater.* **43,** 91–100 (2015).

34. Wauthle, R., Vrancken, B., Beynaerts, B., Jorissen, K., Schrooten, J., Kruth, J.-P. & Van Humbeeck, J. Effects of build orientation and heat treatment on the microstructure and mechanical properties of selective laser melted Ti6Al4V lattice structures. *Addit. Manuf.* **5,** 77–84 (2015).

35. Wang, D., Yang, Y., Liu, R., Xiao, D. & Sun, J. Study on the designing rules and processability of porous structure based on selective laser melting (SLM). *J. Mater. Process. Technol.* **213,** 1734–1742 (2013).

36. Reinhart, G. & Teufelhart, S. Load-adapted design of generative manufactured lattice structures. *Phys. Procedia* **12,** 385–392 (2011).

37. Buls, S., Craeghs, T., Clijsters, S., Kempen, K., Swevers, J. & Kruth, J.-P. The influence of a dynamically optimized galvano based laser scanner on the total scan time of slm parts. *Solid Free. Fabr. Symp.* 260–266 (2013).

38. Cambridge Technology. *New Fully Integrated Subsystems The Future of Laser Processing* Stuttgart, 2014. <http://camtech.com/index.php?option=com_content&view=article&id=161:new-24-bit-scan-controller-and-user-interface-scanmastertm-controller-a-scanmastertm-software&catid=45:press-releases&Itemid=71>.

39. Argento, C. & Bouvard, D. A Ray Tracing Method For Evaluating The Radiative Heat Transfer In Porous Media. *Int. J. Heat Mass Transf.* **39,** 3175–3180 (1996).

40. Laoui, T., Wang, X, Childs, T. H. C., Kruth, J.-P. & Froyen, L. Laser penetration in a powder bed during selective laser sintering of metal powders: simulations versus experiments. *Solid Free. Fabr. Symp.* 453–460 (2000).

41. Rombouts, M., Froyen, L., Gusarov, A. V., Bentefour, E. H. & Glorieux, C. Light extinction in metallic powder beds: Correlation with powder structure. *J. Appl. Phys.* **98** (2005).

42. Buls, S., Clijsters, S. & Kruth, J.-P. Homogenizing the melt pool intensity distribution in the SLM process through system identification and feedback control. *Solid Free. Fabr. Symp.* 6–11 (2014).

43. Bergström, D. *The Absorption of Laser Light by Rough Metal Surfaces* PhD thesis (Lulea University of Technology, 2008).

44. Argento, C. & Bouvard, D. Modeling the effective thermal conductivity of random packing of spheres through densification. *Int. J. Heat Mass Transf.* **39,** 1343–1350 (1996).

45. Tolochko, N. K., Khlopkov, Y. V., Mozzharov, S. E., Ignatiev, M. B., Laoui, T. & Titov, V. I. Absorptance of powder materials suitable for laser sintering. *Rapid Prototyp. J.* **6,** 155–161 (2000).

46. Bergström, D., Powell, J. & Kaplan, F. H. The absorptance of steels to Nd : YLF and Nd : YAG laser light at room temperature. *Appl. Surf. Sci.* **253,** 5017–5028 (2007).

47. Chen, W., Zhang, X. & Jia, L. Penetration monitoring and control of CO 2 laser welding with coaxial visual sensing system. *Proc. SPIE* **5629,** 129–140 (2005).

48. Sankaranarayanan, S. & Kar, A. Nonlinear effects of laser – plasma interaction on melt-surface temperature. *J. Appl. Phys.* **32,** 777–784 (1999).

49. Xie, J. & Kar, A. Laser welding of thin sheet steel with surface oxidation. *Weld. J.* **78,** 343–348 (1999).

50. André, C. *Modélisation quantitative du procédé de frittage sélectif par laser: relation paramètres/microstructure* PhD thesis (Ecole Polytechnique Fédérale de Lausanne, 2007).

51. Tsotsas, E. & Martin, H. Thermal conductivity of packed beds: A review. *Chem. Eng. Process. Process Intensif.* **22,** 19–37 (1987).

52. Alkahari, M. R., Furumoto, T., Ueda, T., Hosokawa, A., Tanaka, R. & Abdul Aziz, M. S. Thermal Conductivity of Metal Powder and Consolidated Material Fabricated via Selective Laser Melting. *Key Eng. Mater.* **523-524,** 244–249 (2012).

53. Zhang, Y., Faghri, A., Buckley, C. W. & Bergman, T. L. Three-dimensional sintering of two-component metal powders with stationary and moving laser beams. *Trans. ASME* **122,** 150 (2000).

54. Zeng, K., Pal, D. & Stucker, B. E. A Review of Thermal Analysis Methods in Laser Sintering and Selective Laser Melting. *Proc. Solid Free. Fabr. Symp.* 796–814 (2012).

55. Taylor, C. M. *Direct laser sintering of stainless steel : thermal experiments and numerical modelling* PhD thesis (University of Leeds, 2004).

56. Hadley, G. R. Thermal-conductivity of packed metal powders. *Int. J. Heat Mass Transf.* **29,** 909–920 (1986).

57. Gonzo, E. E. Estimating correlations for the effective thermal conductivity of granular materials. *Chem. Eng. J.* **90,** 299–302 (2002).

58. Furumoto, T., Ueda, T., Hosokawa, A., Abe, S. & Childs, T. H. C. Study on the Measurement of Physical Properties in the Metal Powder for Rapid Prototyping. *J. Japan Soc. Precis. Eng.* **73,** 558–562 (2007).
59. Bauer, T. H. A general analytical approach toward the thermal conductivity of porous media. *Int. J. Heat Mass Transf.* **36,** 4181–4191 (1993).
60. Tolochko, N. K., Arshinov, M. K., Gusarov, A. V., Titov, V. I., Laoui, T. & Froyen, L. Mechanisms of selective laser sintering and heat transfer in Ti powder. *Rapid Prototyp. J.* **9,** 314–326 (2003).
61. Doubenskaia, M., Pavlov, M. & Chivel, Y. Optical System for On-Line Monitoring and Temperature Control in Selective Laser Melting Technology. *Key Eng. Mater.* **437,** 458–461 (2010).
62. Garrido, C., Leon, B. & Perez-Amor, M. A model to calculate the temperature induced by a laser. *J. Appl. Phys.* **69,** 1133 (1991).
63. Craeghs, T., Clijsters, S., Yasa, E., Bechmann, F., Berumen, S. & Kruth, J.-P. Determination of geometrical factors in Layerwise Laser Melting using optical process monitoring. *Opt. Lasers Eng.* **49,** 1440–1446 (2011).
64. Bag, S., Trivedi, A. & De, A. Development of a finite element based heat transfer model for conduction mode laser spot welding process using an adaptive volumetric heat source. *Int. J. Therm. Sci.* **48,** 1923–1931 (2009).
65. Chua, C. K., Liu, A. & Leong, K. F. A practical approach on temperature variation in Selective Laser Melting with a novel heat transfer model. *Innov. Dev. Des. Manuf.* 363–367 (2010).
66. Van Elsen, M., Baelmans, M., Mercelis, P. & Kruth, J.-P. Solutions for modelling moving heat sources in a semi-infinite medium and applications to laser material processing. *Int. J. Heat Mass Transf.* **50,** 4872–4882 (2007).
67. Kolossov, S. *Non-Linear Model and Finite Element Simulation of the Selective Laser Sintering Process* PhD thesis (Ecole Polytechnique Fédérale de Lausanne, 2005).
68. Dai, K. & Shaw, L. Distortion minimization of laser-processed components through control of laser scanning patterns. *Rapid Prototyp. J.* **8,** 270–276 (2002).
69. Dai, K. & Shaw, L. Finite element analysis of the effect of volume shrinkage during laser densification. *Acta Mater.* **53,** 4743–4754 (2005).
70. Gürtler, F.-J., Karg, M., Leitz, K.-H. & Schmidt, M. Simulation of Laser Beam Melting of Steel Powders using the Three-Dimensional Volume of Fluid Method. *Phys. Procedia* **41,** 881–886 (2013).
71. Hussein, A., Hao, L., Yan, C. & Everson, R. Finite element simulation of the temperature and stress fields in single layers built without-support in selective laser melting. *Mater. Des.* **52,** 638–647 (2013).
72. Brif, Y., Thomas, M. & Todd, I. The use of high-entropy alloys in additive manufacturing. *Scr. Mater.* **99,** 93–96 (2015).

73. Dong, L., Makradi, A., Ahzi, S. & Remond, Y. Three-dimensional transient finite element analysis of the selective laser sintering process. *J. Mater. Process. Technol.* **209,** 700–706 (2009).

74. Zaeh, M. F. & Kahnert, M. The effect of scanning strategies on electron beam sintering. *Prod. Eng.* **3,** 217–224 (2009).

75. Matsumoto, M., Shiomi, M., Osakada, K. & Abe, F. Finite element analysis of single layer forming on metallic powder bed in rapid prototyping by selective laser processing. *Int. J. Mach. Tools Manuf.* **42,** 61–67 (2002).

76. Zaeh, M. F., Branner, G. & Krol, T. A. A three dimensional FE-model for the investigation of transient physical effects in Selective Laser Melting. *Innov. Dev. Des. Manuf. - Adv. Res. Virtual Rapid Prototyp.* 415–424 (2010).

77. Delgado, J., Ciurana, J. & Rodríguez, C. Influence of process parameters on part quality and mechanical properties for DMLS and SLM with iron-based materials. *Int. J. Adv. Manuf. Technol.* **60,** 601–610 (2012).

78. Morton, W., Green, S., Rennie, A. & Abram, T. Surface finishing techniques for SLM manufactured stainless steel 316L components. *Innov. Dev. Virtual Phys. Prototyp.* 503–509 (2012).

79. Senthilkumaran, K., Pandey, P. M. & Rao, P. V. M. Influence of building strategies on the accuracy of parts in selective laser sintering. *Mater. Des.* **30,** 2946–2954 (2009).

80. Thijs, L., Montero Sistiaga, M. L., Wauthle, R., Xie, Q., Kruth, J.-P. & Van Humbeeck, J. Strong morphological and crystallographic texture and resulting yield strength anisotropy in selective laser melted tantalum. *Acta Mater.* **61,** 4657–4668 (2013).

81. Mumtaz, K., Vora, P. & Hopkinson, N. A method to eliminate anchors/supports from directly laser melted metal powder bed processes. *Solid Free. Fabr. Symp.* 55–64 (2011).

82. Materialise. *Magics software* 2015. <http://software.materialise.com/magics> (visited on 06/17/2015).

83. Crawford, R. H. & Beaman, J. J. A method to generate exact contour files for solid freeform fabrication. *Proc. 1992 Solid Free. Fabr. Symp.* 95–101 (1992).

84. Shi, Y., Zhang, W., Cheng, Y. & Huang, S. Compound scan mode developed from subarea and contour scan mode for selective laser sintering. *Int. J. Mach. Tools Manuf.* **47,** 873–883 (2007).

85. Yadroitsev, I., Yadroitsava, I. & Smurov, I. Strategy of fabrication of complex shape parts based on the stability of single laser melted track. *SPIE LASE* **7921,** 79210C–79210C–13 (2011).

86. Yadroitsev, I., Gusarov, A., Yadroitsava, I. & Smurov, I. Single track formation in selective laser melting of metal powders. *J. Mater. Process. Technol.* **210,** 1624–1631 (2010).

87. Van Elsen, M. *Complexity of Selective Laser Melting: a new optimisation approach* PhD thesis (Katholieke Universiteit Leuven, 2007). ISBN: 9789056827687.

88. Van Elsen, M., Al-Bender, F. & Kruth, J.-P. Application of dimensional analysis to selective laser melting. *Rapid Prototyp. J.* **14,** 15–22 (2008).

89. Kumar, S. Selective Laser Sintering: Recent Advances. *4th Pacific Int. Conf. Appl. Lasers Opt.* 1–8 (2010).

90. Averyanova, M., Bertrand, P. & Grevey, D. Optimization of Selective Laser Melting technology using design of experiments method. *Innov. Dev. Virtual Phys. Prototyp.* 459–466 (2012).

91. Campanelli, S. L., Contuzzi, N. & Ludovico, A. D. Manufacturing of 18 Ni Marage 300 Steel Samples by Selective Laser Melting. *Adv. Mater. Res.* **83-86,** 850–857 (2009).

92. Delgado, J., Sereno, L. & Ciurana, J. Methodology for analyzing the depth of sintering in the building platform. *Innov. Dev. Virtual Phys. Prototyp.* 495–498 (2012).

93. Deng, X. M. & Beaman, J. J. Application of Factorial Design in Selective Laser Sintering. *Proc. SFF Symp.* 154–160 (1992).

94. Mertens, R., Clijsters, S., Kempen, K. & Kruth, J.-P. Optimization of Scan Strategies in Selective Laser Melting of Aluminum Parts With Downfacing Areas. *J. Manuf. Sci. Eng.* **136,** 061012 (2014).

95. Craeghs, T., Clijsters, S., Yasa, E. & Kruth, J.-P. Online quality control of selective laser melting. *Solid Free. Fabr. Proc.* 212–226 (2011).

96. Berumen, S., Bechmann, F., Lindner, S., Kruth, J.-P. & Craeghs, T. Quality control of laser- and powder bed-based Additive Manufacturing (AM) technologies. *Phys. Procedia* **5,** 617–622 (2010).

97. Mumtaz, K. & Hopkinson, N. Selective Laser Melting of thin wall parts using pulse shaping. *J. Mater. Process. Technol.* **210,** 279–287 (2010).

98. Pohl, H., Simchi, A., Issa, M. & Dias, H. C. Thermal stresses in direct metal laser sintering. *Proc. SFF Symp.* 366–372 (2001).

99. Furumoto, T., Ueda, T., Abdul Aziz, M., Hosokawa, A. & Tanaka, R. Study on Reduction of Residual Stress Induced during Rapid Tooling Process: Influence of Heating Conditions on Residual Stress. *Key Eng. Mater.* **447-448,** 785–789 (2010).

100. Shiomil, M., Yamashital, T., Osakada, K., Shiomi, M., Yamashita, T., Abe, F. & Nakamura, K. Residual Stress within Metallic Model Made by Selective Laser Melting Process. *Ann. CIRP* **53,** 195–198 (2004).

101. Nickel, A. H., Barnett, D. M. & Prinz, F. B. Thermal stresses and deposition patterns in layered manufacturing. *Mater. Sci. Eng. A* **317,** 59–64 (2001).

102. Zhu, H. H., Fuh, J. Y. H. & Lu, L. The influence of powder apparent density on the density in direct laser-sintered metallic parts. *Int. J. Mach. Tools Manuf.* **47,** 294–298 (2007).

103. Aboulkhair, N. T., Everitt, N. M., Ashcroft, I. & Tuck, C. Reducing porosity in AlSi10Mg parts processed by selective laser melting. *Addit. Manuf.* **1-4,** 77–86 (2014).

104. Jhabvala, J., Boillat, E., Antignac, T. & Glardon, R. Study and simulation of different scanning strategies in SLM. *Innov. Dev. Des. Manuf.* 369–375 (2010).

105. Rombouts, M., Kruth, J.-P., Froyen, L. & Mercelis, P. Fundamentals of selective laser melting of alloyed steel powders. *CIRP Ann. - Manuf. Technol.* **55,** 187–192 (2006).

106. Tolochko, N. K., Mozzharov, S. E., Yadroitsev, I. A., Laoui, T., Froyen, L., Titov, V. I. & Ignatiev, M. B. Balling processes during selective laser treatment of powders. *Rapid Prototyp. J.* **10,** 78–87 (2004).

107. Guo, C., Ge, W. & Lin, F. Effects of scanning parameters on material deposition during Electron Beam Selective Melting of Ti-6Al-4V powder. *J. Mater. Process. Technol.* **217,** 148–157 (2014).

108. Zhang, W., Shi, Y., Liu, B., Xu, L. & Jiang, W. Consecutive sub-sector scan mode with adjustable scan lengths for selective laser melting technology. *Int. J. Adv. Manuf. Technol.* **41,** 706–713 (2009).

109. Bormann, T., Müller, B., Schinhammer, M., Kessler, A., Thalmann, P. & de Wild, M. Microstructure of selective laser melted nickel–titanium. *Mater. Charact.* **94,** 189–202 (2014).

110. Morgan, R. H., Papworth, A. J., Sutcliffe, C., Fox, P. & Oneill, W. High density net shape components by direct laser re-melting of single-phase powders. *J. Mater. Sci.* **37,** 3093–3100 (2002).

111. Yadroitsev, I., Pavlov, M., Bertrand, P. & Smurov, I. Mechanical properties of samples fabricated by selective laser melting. *14èmes Assises Eur. du Prototypage Fabr. Rapide* (2009).

112. Doubenskaia, M., Pavlov, M. & Chivel, Y. Optical monitoring of heat processes in selective laser melting. *Proc. SPIE* **7921,** 79210D–79210D–10 (2011).

113. Beal, V. E., Erasenthiran, P., Hopkinson, N., Dickens, P. & Ahrens, C. H. The effect of scanning strategy on laser fusion of functionally graded H13/Cu materials. *Int. J. Adv. Manuf. Technol.* **30,** 844–852 (2006).

114. Kempen, K., Vrancken, B., Thijs, L., Buls, S., Van Humbeeck, J. & Kruth, J.-P. Lowering thermal gradients in Selective Laser melting by pre-heating the baseplate. *Solid Free. Fabr. Proc.* **24** (2013).

115. Brandl, E., Heckenberger, U., Holzinger, V. & Buchbinder, D. Additive manufactured AlSi10Mg samples using Selective Laser Melting (SLM): Microstructure, high cycle fatigue, and fracture behavior. *Mater. Des.* **34,** 159–169 (2012).

116. Bi, G., Gasser, A., Wissenbach, K., Drenker, A. & Poprawe, R. Identification and qualification of temperature signal for monitoring and control in laser cladding. *Opt. Lasers Eng.* **44,** 1348–1359 (2006).

117. Craeghs, T., Bechmann, F., Berumen, S. & Kruth, J.-P. Feedback control of Layerwise Laser Melting using optical sensors. *Phys. Procedia* **5,** 505–514 (2010).

118. Deckera, I., Heyn, H., Martinen, D. & Wohlfahrt, H. Process monitoring in laser beam cutting on its way to industrial application. *SPIE Proc.* **3097,** 29–37 (1997).

119. Hertle, D. & Sieben, M. Process monitoring using the principle of reflection diagnosis. *Phys. Procedia* **12,** 771–778 (2011).

120. Wiesemann, W. in *New Ser. Landolt-Bornstein Laser Appl.* 1st ed., 243–272 (Springer, 2004). ISBN: 978-3540001058.

121. Weberpals, J., Hermann, T., Berger, P. & Singpiel, H. Utilisation of thermal radiation for process monitoring. *Phys. Procedia* **12,** 704–711 (2011).

122. Lott, P., Schleifenbaum, H., Meiners, W., Wissenbach, K., Hinke, C. & Bültmann, J. Design of an optical system for the in situ process monitoring of Selective Laser Melting (SLM). *Phys. Procedia* **12,** 683–690 (2011).

123. Kruth, J.-P., Mercelis, P., Van Vaerenbergh, J. & Craeghs, T. *Feedback control of Selective Laser Melting* tech. rep. (KU Leuven, 2007), 1–7.

124. Yasa, E., Craeghs, T., Badrossamay, M. & Kruth, J.-P. Rapid Manufacturing Research at the Catholic University of Leuven. *RapidTech 2009,* 1–10 (2009).

125. Craeghs, T., Clijsters, S., Kruth, J.-P., Bechmann, F. & Ebert, M.-C. Detection of Process Failures in Layerwise Laser Melting with Optical Process Monitoring. *Phys. Procedia* **39,** 753–759 (2012).

126. Chivel, Y. & Smurov, I. On-line temperature monitoring in selective laser sintering/melting. *Phys. Procedia* **5,** 515–521 (2010).

127. Pavlov, M., Doubenskaia, M. & Smurov, I. Pyrometric analysis of thermal processes in SLM technology. *Phys. Procedia* **5,** 523–531 (2010).

128. Chivel, Y. Optical In-Process Temperature Monitoring of Selective Laser Melting. *Phys. Procedia* **41,** 904–910 (2013).

129. Krauss, H., Eschey, C. & Zaeh, M. F. Thermography for Monitoring the Selective Laser Melting Process. *Proc. 23rd Annu. Int. Solid Free. Fabr. Symp.* 999–1014 (2012).

130. Grum, J. & Slabe, J. M. Effect of laser-remelting of surface cracks on microstructure and residual stresses in 12Ni maraging steel. *Appl. Surf. Sci.* **252,** 4486–4492 (2006).

131. Wang, W. F., Zheng, Y. G., Yao, J. H. & Zhang, M. Effects of the Particle Size Variety of Metal Oxide on the Absorption Property of Long-Wavelength Infrared Laser. *Adv. Mater. Res.* **418-420,** 536–539 (2011).

132. Yasa, E., Kruth, J.-P. & Deckers, J. Manufacturing by combining Selective Laser Melting and Selective Laser Erosion/laser re-melting. *CIRP Ann. - Manuf. Technol.* **60,** 263–266 (2011).

133. Xu, W., Brandt, M., Sun, S., Elambasseril, J., Liu, Q., Latham, K., Xia, K. & Qian, M. Additive manufacturing of strong and ductile Ti–6Al–4V by selective laser melting via in situ martensite decomposition. *Acta Mater.* **85,** 74–84 (2015).

134. Attar, H., Prashanth, K. G., Chaubey, A., Calin, M., Zhang, L. C., Scudino, S. & Eckert, J. Comparison of wear properties of commercially pure titanium prepared by selective laser melting and casting processes. *Mater. Lett.* **142,** 38–41 (2015).

135. Thijs, L., Kempen, K., Kruth, J.-P. & Van Humbeeck, J. Fine-structured aluminium products with controllable texture by selective laser melting of pre-alloyed AlSi10Mg powder. *Acta Mater.* **61,** 1809–1819 (2013).

136. Averyanova, M. & Bertrand, P. Direct Manufacturing of dense parts from martensitic precipitation hardening steel gas atomized powder by Selective Laser Melting (SLM) technology. *Innov. Dev. Des. Manuf.* 343–348 (2010).

137. Tjong, S. Microstructural and mechanical characteristics of in situ metal matrix composites. *Mater. Sci. Eng. R Reports* **29,** 49–113 (2000).

138. Gu, D., Hong, C. & Meng, G. Densification, microstructure, and wear property of in situ titanium nitride-reinforced titanium silicide matrix composites prepared by a novel selective laser melting process. *Metall. Mater. Trans. A Phys. Metall. Mater. Sci.* **43,** 697–708 (2012).

139. Dadbakhsh, S. & Hao, L. Effect of Al alloys on selective laser melting behaviour and microstructure of in-situ formed particle reinforced composites. *J. Alloys Compd.* **541,** 328–334 (2012).

140. King, D. & Tansey, T. Rapid tooling: Selective laser sintering injection tooling. *J. Mater. Process. Technol.* **132,** 42–48 (2003).

141. Yen, H. C. & Tang, H. H. Developing a paving system for fabricating ultra-thin layers in ceramic laser rapid prototyping. *Int. J. Adv. Manuf. Technol.* **36,** 280–287 (2008).

142. Karapatis, P. *A sub-process approach of selective laser sintering* PhD thesis (Ecole Polytechnique Fédérale de Lausanne, 2002).

143. Matweb. *EOS MS1 Maraging Steel for DMLS 3D Printing* 2015. <http://www.matweb.com/search/DataSheet.aspx?MatGUID=e9f7cb19eb81450d8f67966151bd1802> (visited on 08/17/2015).

144. Matweb. *Aluminum 360.0F Die Casting Alloy* 2015. <http://www.matweb.com/search/DataSheet.aspx?MatGUID=46cc3a20683748718693cbb6039bec68> (visited on 08/17/2015).

145. Matweb. *Silver* 2015. <http://www.matweb.com/search/DataSheet.aspx?MatGUID=63cbd043a31f4f739ddb7632c1443d33> (visited on 08/17/2015).

146. Matweb. *Titanium* 2015. <http://www.matweb.com/search/DataSheet.aspx?MatGUID=66a15d609a3f4c829cb6ad08f0dafc01> (visited on 08/17/2015).

147. Nicolle, R. L., Irvine, J. & Bowden, F. G. Near-infra-red diffuse reflectivities of natural and man-made materials. *J. Phys. D. Appl. Phys.* **2,** 201–204 (2002).

148. Parker, W. J., Jenkins, R. J., Butler, C. P. & Abbott, G. L. Flash method of determining thermal diffusivity, heat capacity, and thermal conductivity. *J. Appl. Phys.* **32,** 1679–1684 (1961).

149. Sih, S. S. & Barlow, J. W. The Measurement of the Thermal Properties and Absorptances of Powders Near Their Melting Temperatures. *Chem. Eng.* 131–140 (1992).

150. Rombouts, M., Froyen, L., Gusarov, A. V., Bentefour, E. H. & Glorieux, C. Photopyroelectric measurement of thermal conductivity of metallic powders. *J. Appl. Phys.* **97** (2005).

151. Taylor, C. M. & Childs, T. H. C. Thermal Stresses in Direct Metal Laser Sintering. *Solid Free. Fabr. Symp.* 366–372 (2001).

152. Johnston, T. F. & Sasnett, M. W. in *Handb. Opt. Laser Scanning* (ed Marshall, G. F.) 5–8 (Marcel Dekker Inc., New York, 2004). ISBN: 0-8247-5569-3.

153. Lewis, J. P. Fast template matching. *Vis. interface,* 120–123 (1995).

154. Incorpera, F. P. & DeWitt, D. P. *Fundamentals of heat transfer* 6th ed., 927–958. ISBN: 978-0471457282 (John Wiely & Sons, New York, 1981).

Curriculum Vitae – VAN GESTEL Christoph

Personal data

Surname	Van Gestel	Nationality	Belgian
Name	Christoph		
E-mail	christoph.vangestel@gmail.com		

Work experience

2011-2015	PhD – “Study of physical phenomena of Selective Laser Melting towards increased productivity” Laboratory for production management and processes Ecole Polytechnique Fédérale de Lausanne (Switzerland)
Tasks	R&D collaboration with small and large companies Management and training of junior scientists (bachelor/master) Full design, implementation and validation of material/process test equipment

Education

2009-2011	Master in Engineering Sciences: Material sciences Option Polymers and Composites Katholieke Universiteit Leuven, Leuven (Belgium)
2009-2010	Erasmus exchange year Ecole Polytechnique Fédérale de Lausanne, Lausanne (Switzerland)
2006-2009	Bachelor in Engineering Sciences: Material sciences Katholieke Universiteit Leuven, Leuven (Belgium)

Competences

Additive manufacturing – Selective Laser Melting	
Powder characterization – test design and implementation	PhD
Process monitoring – sensor integration and software	PhD
Composite production and mechanical testing	Master

Skills

Languages	Dutch	(mother tongue)	French	(fluent, B2)
	English	(fluent, C1/C2)	German	(basic, fluent reading)

Software	Proficient	LabVIEW (certified CLAD)
	Accustomed	Matlab; Mathematica; SolidEdge (3D CAD); LaTeX
	Basic	ELMER (finite element); Java, Scala, various IDE’s